DSE - Airborne Wind Power

Design a durable and lightweight wing that can be used for cost-effective traction power generation in a pumping kite power system

R.J.Coenen	1506862	R.J.Meijer	4008200
S.Drenth	4064127	F.T.Ndonga	1543954
M.T.Islam	4009592	T.Smits	4094336
R.J.Kruithof	1507265	M.L.W.Veraart	4091531
K.Lindeborg	4013360		

Final Report

Design Synthesis Exercise

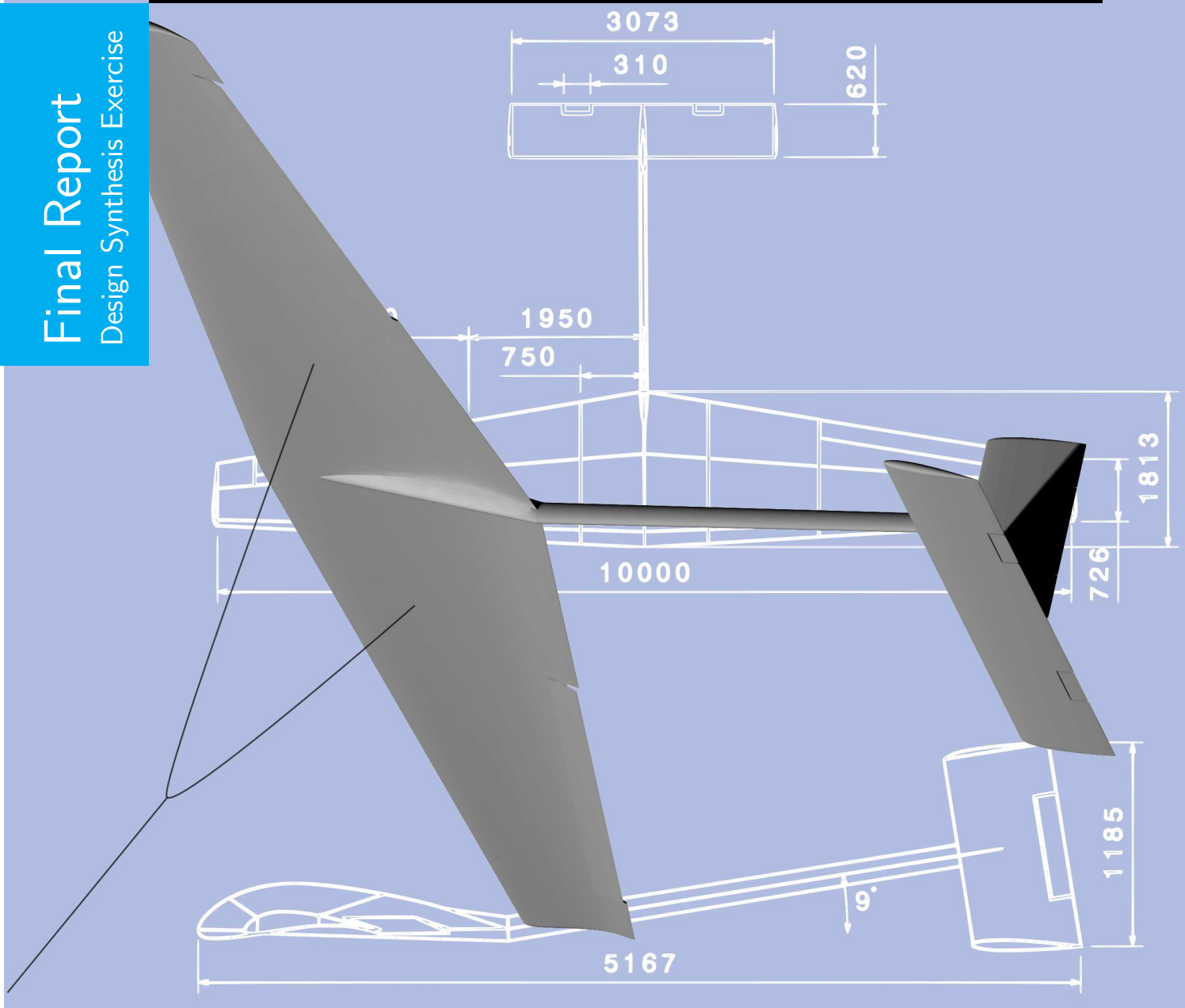

TU Delft Delft University of Technology

Aerospace Engineering

January 27, 2015

Preface

For completing the Bachelor in Aerospace Engineering, students are given the responsible task to make a challenging Design Synthesis Exercise (DSE). In this exercise the students are given the opportunity to obtain design experience in a multidisciplinary design project. The project consists of a realistic problem, where team work, communication, and design are some of the key factors. During the DSE three reports are submitted, where the complete process of the design is clearly presented.

This report is the 'final' technical report for the DSE to design a durable and light-weight kite for pumping kite power generation. The design concept chosen in the 'mid-term' is further analyzed into the final design. A detailed analysis into its technical properties, such as structures, aerodynamics, stability and control is done to optimize the kite ensuring it will meet the performance requirements. Besides the technical aspects of the kite, an elaboration on reliability, maintainability, safety and risk is included in this report. Finally, the conclusion and recommendations for future development of this system are discussed.

We would like to thank and express our appreciation to our tutor Roland Schmehl and two mentors Sofia Teixeira de Freitas (associate professors at the Delft University of Technology) and Jacco Geul (ir. and PHD candidate at the Delft University of Technology) for their constant guidance and support. We would also like to express our gratitude to Christoph Grete and Felix Friedl (Kite Power 2.0) and Alfred van den Brink and Coert Smeenk (E-Kite), for providing feedback from the industry. Finally we would like to thank TU Delft to give us the opportunity to participate in this innovative project and provide us with all the necessary equipments and facilities.

DSE Group 03, January 2015

Contents

List of Abbreviations

Abbreviation	Definition
ac	Aerodynamic Center
AWE	Airborne Wind Energy
CAD	Computer Aided Design
CFD	Computational Fluid Dynamics
CFRP	Carbon Fiber Reinforced Polymer
cg	Center of Gravity
CTF	Cycles To Failure
DSE	Design Synthesis Exercise
ESDU	Engineering Sciences Data Unit
FBD	Free Body Diagram
FEA	Finite Element Analysis
GPS	Global Positioning System
HMPE	High Modulus Poly Ethelene
ISA	International Standard Atmosphere
ICOF	In Case Of Failure
LCOE	Levelized Cost Of Energy
MAC	Mean Aerodynamic Chord
MBL	Minimum Breaking Load
NACA	National Advisory Committee for Aeronautics
np	Neutral Point
OJF	Open Jet Facility
PPU	Power Processing Unit
PV	Photo Voltaics
RAMS	Reliability, Availability, Maintainability, Safety
RDT	Requirement Discovery Tree
RoI	Return on Investment
RPM	Revolutions Per Minute
SL	Service Life
ss	simply supported
SWL	Safe Working Life
ta	Tether Attachment
TOL	Take-Off and Landing
TV	Tail Volume

List of Symbols

Symbol	Description	Unit
A_{cs}	Cross-sectional area	m^2
A_{fs}	Facesheet matrix	-
$A_{enclosed}$	Enclosed cross-sectional area	m^2
a_{rail}	Acceleration given to the kite	m/s^2
A	Aspect ratio	-
A_h	Aspect ratio of the horizontal tail	-
b	Wingspan	m
b_A	Span of aileron	m
b_E	Span of elevator	m
b_h	Wingspan of horizontal tail	m
B_i ‘	Boom area	m^2
b_R	Apan of rudder	m
b_v	Wingspan of vertical tail	m
c_A	Average aileron chord	m
C_c	Control surface chord	m
$\bar{c}$	Mean aerodynamic chord	m
C_d	Airfoil drag coefficient	-
C_D	Wing drag coefficient	-
C_{D_0}	Zero lift drag coefficient	-
C_{D_α}	Drag coefficient slope	rad^{-1}
$C_{D_{eff}}$	Effective drag coefficient	-
C_{D_k}	Kite drag coefficient	-
C_{D_R}	Roll drag coefficient	-
C_{D_t}	Tether drag coefficient	-
C_{d_t}	Circular tether drag coefficient	
C_{D_w}	Drag coefficient of the wing	-
C_e	Elevator chord	m
CF	Crest factor	-
C_h	Hinge moment coefficient	-
C_{h_α}	Hinge moment slope due to angle of attack	-
$C_{h_{\delta_c}}$	Hinge moment slope due to control surface	-
C_l	Profile lift coefficient	-
C_L	Wing lift coefficient	-
C_{L_k}	Kite lift coefficient	-
C_{L_h}	Lift coefficient of the horizontal tail	-
$C_{L_{max}}$	Maximum lift coefficient	-
C_{L_0}	Lift coefficient at zero angle of attack	-

Symbol	Description	Unit
$C_{L_{\alpha_k}}$	Lift slope of the system	rad^{-1}
$C_{L_{\alpha_{A-h}}}$	Lift slope of the system without tail	rad^{-1}
$C_{L_{\alpha_h}}$	Lift slope of the horizontal tail	rad^{-1}
$C_{L_{\alpha_f}}$	Lift slope of the fuselage	rad^{-1}
$C_{L_{\alpha_w}}$	Lift slope of the main wing	rad^{-1}
$C_{L_{\alpha_v}}$	Lift slope of the vertical tail	rad^{-1}
C_m	Profile moment coefficient	-
C_M	Wing moment coefficient	-
$C_{M_{ac}}$	Moment coefficient in the aerodynamic center	-
$C_{m_{\delta E}}$	Moment coefficient due to elevator deflection	-
C_{M_q}	Moment derivative with respect to the pitch rate	-
C_{M_u}	Moment derivative with respect to the airspeed	-
C_{M_x}	Moment derivative with respect to the X force	-
C_{M_q}	Moment derivative with respect to the Z force	-
C_{M_α}	Moment derivative with respect to the angle of attack	-
$C_m rm_0$	Moment derivative with respect to the steady state	-
$C_{M_{\dot{\alpha}}}$	Moment derivative with respect to the angle of attack rate	-
C_{n_r}	Yawing moment coefficient due to turn	-
C_{n_β}	Yawing moment coefficient due to side slip	-
$C_{n_{\delta A}}$	Yawing moment coefficient due to aileron deflection	
$C_{n_{\delta R}}$	Yawing moment coefficient due to rudder deflection	-
C_P	Power coefficient	-
C_R	Rolling moment coefficient	-
c_r	Root chord	m
c_R	Rudder chord	m
$C_{R_{\delta A}}$	Slope of roll coefficient due to aileron deflection	rad^{-1}
c_{RPM}	Revolutions per minute	-
C_{X_0}	Force in x-direction derivative in steady state	-
C_{X_α}	Force in x-direction derivative with respect to angle of attack	-
$C_{X_{\delta e}}$	Force in x-direction derivative with respect to elevator deflection	-
C_{X_q}	Force in x-direction derivative with respect to pitch rate	-
C_{X_u}	Force in x-direction derivative with respect to airspeed	-
c_t	Tip chord	m
$(C_{Y_r})_v$	Side force due to ver. tail coefficient	-
C_{Z_0}	Force in z-direction derivative in steady state	-
C_{Z_q}	Force in z-direction derivative with respect to pitch rate	-
C_{Z_u}	Force in z-direction derivative with respect to airspeed	-
C_{Z_α}	Force in z-direction derivative with respect to angle of attack	-
$C_{Z_{\dot{\alpha}}}$	Force in z-direction derivative with respect to angle of attack rate	-
$C_{Z_{\delta e}}$	Force in z-direction derivative with respect to elevator deflection	-
C_0	Zero angle of attack and deflection hinge moment coefficient	-
D	Total drag	N
d	Diameter	m
D_{dp}	Diameter of drum and sheave	m

Symbol	Description	Unit
D_{m}	Diameter of the torque motor drum	m
D_{fs}	Sandwich facesheet	-
D_{R}	Roll drag	N
d_{t}	Tether diameter	m
D_{sw}	Sandwich panel correction	-
e	Oswald factor	-
E	Young's modulus	$\mathrm{N/m^2}$
E_{k}	Kinetic energy	J
E_{p}	Potential energy	J
F_{b}	Bridle force	N
$F_{\mathrm{b_{crit}}}$	Crtitical buckling load	N
F_{C}	Centripetal force	N
f_{d}	Design factor	-
f_{k}	Load factor	-
F_{MB}	Mean breaking load	N
F_{r}	Radial force	N
$F_{\mathrm{reel-in}}$	Reel in force	N
f_{s}	Season temperature factor	-
F_{tether}	Tether force	N
$F_{\mathrm{t_{max}}}$	Maximum tether force	N
F_{t}	Tension force in tether	N
f_{t}	Day/night temperature factor	-
F_{τ}	Tangential force	N
F_{x}	Aerodynamic forces in x-direction	N
F_{z}	Aerodynamic forces in z-direction	N
g	Gravitational constant	$\mathrm{m/s^2}$
γ_{glide}	Glide angle	deg
G_{c}	Shear modulus for the core	Pa
H	Hinge moment	Nm
h	Height/Altitude	m
$h_{aft_{gl}}$	Altitude achieved after gliding	m
H_{A}	Hinge moment of aileron	Nm
H_{E}	Hinge moment of elevator	Nm
H_{R}	Hinge moment of rudder	Nm
h_0	Reference altitude	m
$h_{\mathrm{P\approx 40kW}}$	Altitude for which 40 kW is generated	m
I_{xx}	Moment of area around x-axis	$\mathrm{m^4}$
I_{xy}	Product moment of area around x- and y-axis	$\mathrm{m^4}$
I_{yy}	Moment of area around y-axis	$\mathrm{m^4}$
I_{zz}	Moment of area around z-axis	$\mathrm{m^4}$
J_x	Mass moment of inertia around x-axis	$\mathrm{kg\ m^2}$
J_{xz}	Products of inertia relative to the x and y	$\mathrm{kg\ m^2}$
J_y	Mass moment of inertia around y-axis	$\mathrm{kg\ m^2}$
L	Total Lift	N
L_{A}	Rolling moment due to aileron deflection	Nm
λ	Horizontal buckling factor	-
l_{h}	Distance between wing and hot. tail	m

Symbol	Description	Unit
l_v	Distance between wing and ver. tail	m
L_s	Service life	s
L_{sw}	Save working life	-
L_t	Tail lift force	N
M	molar mass of air	kg/mol
m	mass of the kite	kg
M_x	Moment around x-axis	Nm
M_y	Moment around y-axis	Nm
M_z	Moment around z-axis	Nm
N	Yaw moment	Nm
N_{bends}	Number of bends	-
N_{crit}	Critical buckling load	N
$N_{crit_{ts}}$	Critical buckling load in transverse shear	N
N_{CTF}	Number of cycles to failure	-
N_f	Number of failures	-
P	Power	W
P_a	Available Power	W
$P_{average}$	Average annual power output	W
P_{rail}	Power required for kite acceleration during take-off	W
$P_{r_{in}}$	Power required during reel in	W
$P_{r_{out}}$	Nominal power output during traction phase	W
P_{cycle}	Average power output during complete cycle	W
P_R	Roll rate	rad/s
$\dot{P}_R$	Change in roll rate	rad/s^2
$P_{R_{ss}}$	Steady State roll rate	rad/s
P_{num}	Numerically derived power	W
p_0	ISA air pressure at sea level	N/m^2
q	Shear flow	N/m
$\bar{q}$	Dynamic pressure	Pa
q_d	Distributed drag force	N/m
q_l	Distributed lift force	N/m
q_s	Shear flow due to force	N/m
$q_{s,0}$	Shear flow at the cut	N/m
q_t	Shear flow due to torsion	N/m
Q_1	pitch rate	rad/s
r_t	Turbine radius	m
r	Tether length	m
R	universal gas constant	J/molK
R_{curv}	Radius of curvature	m
Re	Reynold's number	-
R_t	Turn radius	m
R_w	Resulting wing force	N

Symbol	Description	Unit
S	Wing surface area	m^2
S_c	Control surface area	m^2
S_h	Horizontal tail surface area	m^2
S_{proj}	Projected area	m^2
s_{rail}	Distance traveled on rail	m
S_{tot}	Sum of wing, horizontal and vertical tail Area	m
S_v	Vertical tail surface area	m^2
S_w	Wing surface area	m^2
S_x	Shear force in x direction	N
S_y	Shear force in y direction	N
S_z	Shear force in z direction	N
t	Thickness	m
T	Temperature	K
t_{r_c}	Core (foam) thickness	m
t_{coat}	Coating content	-
t_{cycle}	Cycle time	s
t_{fs}	Facesheet thickness	m
t_{rail}	Time needed for the kite to reach the end of the rail	s
T_{Tor}	Torsion	Nm
$t_{r_{in}}$	Duration of reel-in phase	s
$t_{r_{out}}$	Duration of traction phase	s
t_{trans}	Duration of traction phase	s
t_{ss}	Steady state roll time	s
t_{tot}	Total roll time	s
$t_{tot_{op}}$	Total operating time	y
t_{tv}	Airfoil thickness	m
t_w	Wing thickness	m
T_0	ISA air temperature at sea level	K
t_1	Time to accelerate to steady state roll	s
TV	Tail volume	-
$T_{1/2}$	Half time	s
V	Velocity	m/s
V_a	Apparent velocity	m/s
V_{avg}	Average velocity	m/s
V_h	Horizontal tail air speed	m/s
$\bar{V}_h$	Horizontal tail volume coefficient	-
V_k	Kite velocity	m/s
V_R	Roll velocity	m/s
V_r	Reel velocity	m/s
$V_{r_{in}}$	Reel-in velocity	m/s
$V_{r_{out}}$	Reel-out velocity (traction phase)	m/s
V_{stall}	Stall Speed	m/s
V_v	Vertical tail air speed	m/s
$\bar{V}_v$	Vertical tail volume coefficient	-
V_w	Wind velocity	m/s
$V_{w,0}$	Wind velocity at ground level	m/s

Symbol	Description	Unit
R_1	yaw rate	rad/s
R_{op}	Reliability for a chosen operational time	-
w	width	m
$w_{aft_{gl}}$	Distance travelled after gliding	m
W_{fiber}	Fiber weight	N
W_{kite}	Weight kite system	N
W_{tether}	Tether weight	N
x	Location in x direction	m
$\bar{x}$	Vertical neutral axis position	m
x_{ac}	Location aerodynamic center	m
x_{cg}	Location center of gravity	m
x_{i}	Horizontal position	m
x_{n}	Location neutral point	m
x_{cp}	Location center of pressure	m
y	Location in y direction	m
y_{o_A}	Aileron outboard span	m
y_{i_A}	Aileron inboard span	m
y_{o_E}	Aileron inboard span	m
y_{A}	Aileron average span	m
y_D	Span of roll drag center	m
z	Location in z direction	m
$\bar{z}$	Horizontal neutral axis position	m
z_{i}	Vertical position	m

Greek Symbol	Description	Unit
α	Angle of attack	rad
α_{LS}	Angle of attack of lifting surface	deg
β	Prandtl-Glauert compressibility correction factor	-
β	Side slip angle	rad
γ	Flight path angle during reel-in	rad
ΔC_{m}	Increase in moment coefficient due to elevator deflection	-
ΔD	Roll drag increase	N
ΔL	Lift increase due to aileron deflection	N
ΔM	Moment increase due to elevator deflection	Nm
δ_{A}	Aileron deflection	deg
δ_{c}	Control surface deflection	rad
δ_{E}	Elevator deflection	deg
δ_{R}	Rudder deflection	deg
ϵ	Downwash angle	rad
η	Airfoil effenciency factor	-
η_{b}	Vertical buckling factor	-
η_{h}	Horizontal tail dynamic pressure coefficient	-
η_{v}	Vertical tail dynamic pressure coefficient	-
θ	Elevation angle	deg
κ	Temperature lapse rate	K/m
λ	Taper ratio	-
$\Lambda_{0.5\text{c}}$	Sweep angle at half chord	rad
ρ	Atmospheric density	kg/m^3
σ_{z}	Normal stress	$\text{N/m}^{\ 2}$
σ_{b}	Bending stress	Pa
σ_{mises}	Von Mises stress	Pa
σ_{u}	Ultimate stress	Pa
τ	Shear stress	N/m^2
τ_{A}	Aileron effectiveness	-
τ_{E}	Elevator effectiveness	-
τ_{m}	Torque that needs to be provided by the motor	Nm
τ_{s}	Shear stress	Pa
τ_{R}	Rudder effectiveness	-
θ	Elevation angle	rad
$\ddot{\theta}$	Angular pitch acceleration	rad/s^2
Φ	Bank angle	rad
Φ_{des}	Design bank angle	rad
Φ_{ss}	Bank angle performed in steady state	rad
Φ_1	Bank angle when starting steady state roll	rad
ϕ	Azimuth angle	rad
ϕ	Angle betwee V_{a} and Earth reference system	rad
ρ_{HMPE}	Density of HMPE	kg/m^3
ω	Angular velocity	rad/s
ω_{m}	Angular velocity of motor	rad/s
$\dot{\omega}$	Angular acceleration	rad/s^2
χ	Angle between $F_{\text{reel-in}}$ and reel-in flight path	rad
ξ	Centroid location	m

List of Figures

List of Tables

Abstract

Pumping kite power energy generation is a promising type of Airborne Wind Energy (AWE), with potential to produce electrical power at low cost in a sustainable manner. A team of nine Design Synthesis Exercise (DSE) students of the Aerospace Engineering faculty at the TU Delft has come up with a concept design for pumping kite power generation. The purpose of this final paper is to present the design of a durable and lightweight wing for pumping kite power generation. This prototype design will be an important development step for AWE systems to reach widespread commercial usage, with scaling capabilities up to and beyond an average power generation of 100 kW.

The sizing and investigation of this final design was conducted using different scientific methods. Aerodynamic sizing was done by iterating between XFLR5 software and the numerical power equations [4] in MATLAB. The effect of dirt was investigated in XFLR5 by shifting the transition point to the leading edge. The structural sizing considered the wall thickness before ultimate failure or buckling would occur, again using MATLAB. For the wingbox a stiffened panel (in longitudinal direction) and a sandwich panel were analyzed, of which the latter turned out to be the most effective. For the tail boom (fuselage) a rectangular and an elliptical cross-section were compared. The kite was designed for stability during both traction and retraction phase. The stability coefficients were derived using the equations of motion, force equilibrium and moment equilibrium, while certain assumptions (such as a massless kite and small Earth) were applied. This lead to the sizing of the tail and an optimal tether attachment location. The overall configuration and layout were designed in CATIA, resulting in a total system mass. Annual average power was approximated using power equations and a probability distribution of the wind velocity derived from measured wind data [2]. Future financing of the system was investigated from the development, production and operational cost as well as the Levelized Cost Of Energy (LCOE). A risk analysis was developed for both development and design phase, using a Technical Risk Assessment. Contingency Management is proposed as mitigation strategy in the event that a risk would occur. Risk of the design was also analyzed by taking into account the Reliability, Availability, Manufacturing and Safety (RAMS) of the system.

It was concluded from the trade-off that the final design configuration is a rigid conventional concept, which consists of a main wing, tail boom, horizontal tail surface and a vertical tail surface. The span of the main wing is 10 m, the projected area of the system 12.7 m^2, and a wing root chord of 1.814 m. The airfoil chosen for the main wing is the Wortmann FX73-CL3-152 airfoil, because of its high $C_{l_{max}}$ of 2.25 and large thickness. There is a wingbox in the main wing, where the skin is an integral part of the wingbox. The wingbox is an upside down U-shape with a top panel and two spars made of a sandwich structure, the bottom panel is a simple unstiffened skin panel. 3 ribs on each side (one at the wingtip, one at the bridle position and one close to the root) provide additional stiffness. These ribs are also constructed from sandwich panels. The wingbox parts are connected to each other using adhesive bonding. The tail boom

has an elliptical cross section, with a 9 deg upward deflection at the main wing trailing edge, to keep the tail tangent to the airflow, which decreases the total system drag significantly. This resulted in the total mass of the kite system, which is approximately 40 kg without considering weight contingency.

The results show that there is a large influence of tether drag, resulting in a maximum power output during the traction phase at approximately 150 m altitude. The system requirement for power generation during the traction phase is 40 kW, which is reached up to an altitude of 350 m. A rough wing (covered in dirt) leads to a maximum power of 38 kW at 150 m during the traction phase. The kite can reduce its maximum operating altitude if the wing has accumulated a significant amount of dirt, to keep power constant.

The material used for the wingbox, tail boom and tail will be Carbon Fiber Reinforced Polymer (CFRP). The bridle locations on the wing will be at 1.95 m from the root on both sides of the wing. The sandwich panel reinforced wing box has a mass of 13.9 kg, while the stiffened wing box would weigh 22.1 kg. Therefore the sandwich panel was used in the concept design. The tail boom will have an elliptical cross-section, with a thickness of 1.4 mm resulting in a weight of 3.7 kg. The rectangular tail boom would weigh a kilo less, but the elliptical tail boom was chosen for its aerodynamic benefits and the fact that the extra weight is small compared to the total system weight.

The system will be dynamically stable, though an elevator is required. The tether attachment will be at 0.55 chord from the leading edge. Control surfaces that were added to the design are ailerons at the main wing, a rudder at the vertical tail and an elevator at the horizontal tail. For the communication and control subsystems, data from the kite sensors is processed at the ground station. The data is sent through a wireless transmission between the ground station and the transceiver in the kite. The control box activates the actuators that subsequently set the control surfaces in motion. A launching and landing concept was proposed, where the kite is launched along a mast straight up in the air up to a minimum altitude of 40 m, from where it will glide 200 m downwind to an altitude of 30 m. From that point, the kite is reeled in so it can reach its power cycle starting position; an altitude of 50 m at a downwind distance from the ground station of 100 m.

It was concluded that the largest risk corresponds to the most critical component: failure of the tether. Maintenance schedules are therefore required to prevent tether failure. For safety, the kite can autonomously glide to the ground if the tether breaks. Therefore a large range of the transceiver is required.

A future development process has been proposed, which consists of the development of five systems. Model 1, which has a span of2 m will be the wind tunnel model and will be tested at the Open Jet Facility (OJF). Model 2, with 6.6 m span, can be tested on the current ground station of KitePower 2.0. The prototype with 10 m span and 22 kW average power output as proposed in this report will be constructed if model 2 works as required. Finally, an scaled-up demonstration system (13 m span) with an average power output of 50 kW and a commercial system (18 m span) which will supply 100 kW of average power to the grid after it has been certified, will be developed.

Chapter 1

Introduction

Though the kite in general has a history of more than two thousand years and has been used for many different applications (e.g. fishing, transportation, entertainment, scientific and military purposes), the idea to generate power using a kite only started being investigated two decades ago. Kite power generation is a type of Airborne Wind Energy (AWE) technology, that despite its short existence already has proven to be technically feasible. Next step is to make it economically viable, competing with established renewable energy resources such as solar panels and horizontal axis wind turbines (HAWT). The main reason for this AWE system to be beneficial compared to HAWTs, is that it can easily reach higher altitudes with stable and higher wind velocities (increased potential power) without requiring a large volume of material and foundation. This results in a mobile system, making it also a good competitor to non-renewable energy sources such as diesel generators.

Kite power is generated using a flying kite which is connected by a tether to a drum in the ground station. During the reel-out phase (traction) the kite flies a figure eight trajectory crosswind, with a high effective kite velocity resulting in a traction force through the tether. The tether reels out and the drum starts rotating, this mechanical motion is converted to electrical energy in the ground station. This is followed by a reel-in phase (retraction), where the kite is depowered and the tether reels-in by rotating the drum (the generator now is used as an electric motor). Since the retraction phase requires less energy (caused by the depowering of the kite) than the traction phase, netto power is generated with this system. It is called a pumping kite power system, regarding the continuous cycle of traction and retraction, as can be seen in figure 1.1.

It may be clear that airborne wind energy generation is a young and promising technology, that has the potential to produce electrical power at low cost in a highly sustainable manner. Following recent developments in airborne wind energy generation, the group of nine students of the TU Delft Design Synthesis Exercise have designed a durable and lightweight wing for pumping kite power generation. This prototype design will be an important step to reach widespread commercial useage of this AWE system, with scaling capabilities kept in mind for power generation up to and beyond 100 kW. The final design of this challenging design prototype is presented in this document.

With the final report, all three phases of the design have been concluded, namely the baseline, mid-term and final phase. Reports that were previously delivered included the project plan, the baseline report and the mid-term report. In the project plan, the planning and the set-up of the entire project were highlighted. Next the baseline report, where general requirements,

risks, different design-options corresponding to many design options and a market analysis have been considered. This was followed by the mid-term phase, where non-feasible design options have been taken out leading to five general design concepts. After analysing these options on system characteristics, such as aerodynamic properties, structural properties, stability, and performance, a final trade-off has been made. Some flaws in this trade-off have come up at the beginning of the final phase, leading to a revision and an improved trade-off during the final phase. The final concept is the rigid conventional kite system, which is detailed designed and analysed during the final phase and thoroughly explained in this document.

The final report consists of three main parts, starting with the design details (part I), secondly the AWE system characteristics (part II) and finally the development projections (part III). Part I consists of seven chapters, where chapter 3 summarizes the final overall design of the system, including the general layout and dimensions. Chapter 3 describes the aerodynamic sizing of the kite, the corresponding iteration process and its largest influences. This is followed by the structural sizing in chapter 5, where thickness, layout and sizing of the main structural members within different sections of the kite are determined. Stability characteristics and the sizing of control surfaces are explained in correspondingly chapter 6 and 7. The design details are concluded with the verification and validation methods of aerodynamic, structural and stability calculations of this report, presented in chapter 8. The AWE system characteristics, Part II, are separated in four chapters, starting with the functional flow analysis in chapter 10, the control architecture in chapter 11 and finally a proposal to an automated take-off and landing system in chapter 12. Future development projections in part III have been done with respect to financing the project and (chapter 13) and a risk analysis (chapter 14). Chapter 15 describes the Reliability, Availability, Maintainability and Safety (RAMS) aspects of the system. Also the future development process to finally produce a commercial system is given in chapter 16. Conclusions and recommendations are presented in chapter IV.

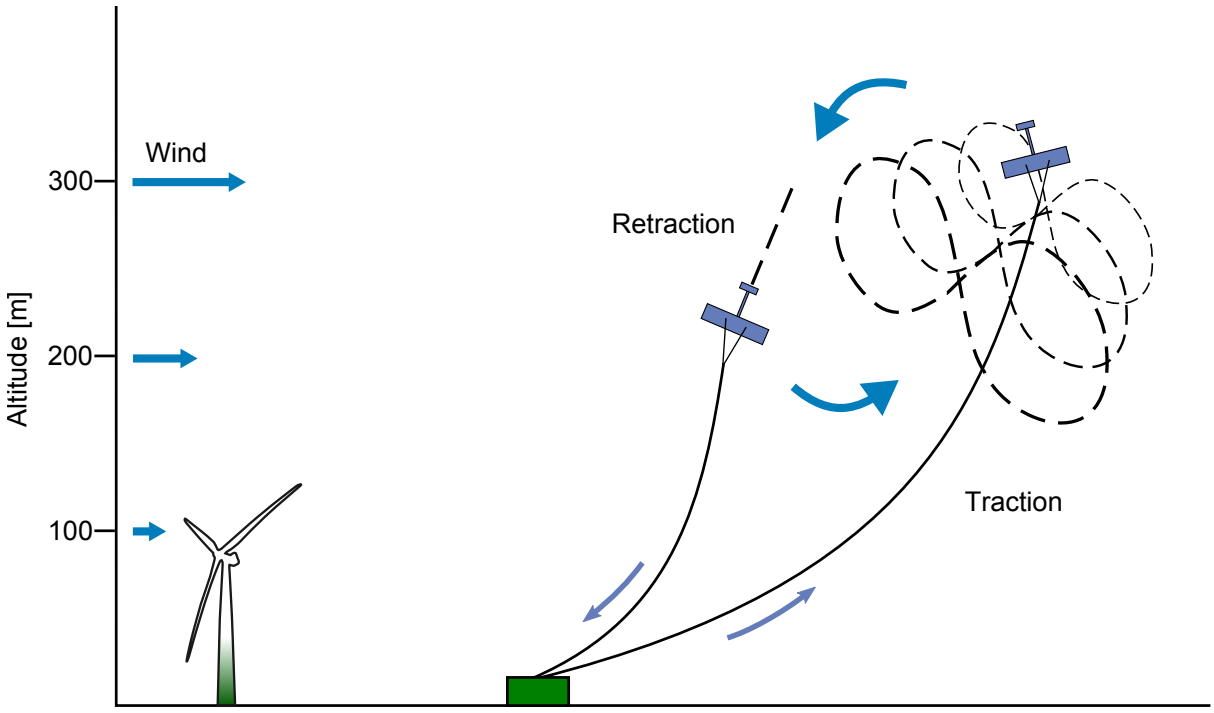

Figure 1.1: Pumping kite power system

Reference systems used in this report are the Earth reference frame and the body reference

frame, as can be seen in figure 1.2. For structural calculations in chapter 5 the body reference frame is used. The body reference frame has its y-axis fixed to the leading edge (LE) of the main wing. Note that for clearance the tail is shown in line with the x-axis, though for the final design this is actually not fixed to each other. The overall design is explained in chapter 3. Stability calculations from chapter 6 are derived from the Earth reference frame leading to the body reference system, important assumptions such as small Earth are also explained in this chapter.

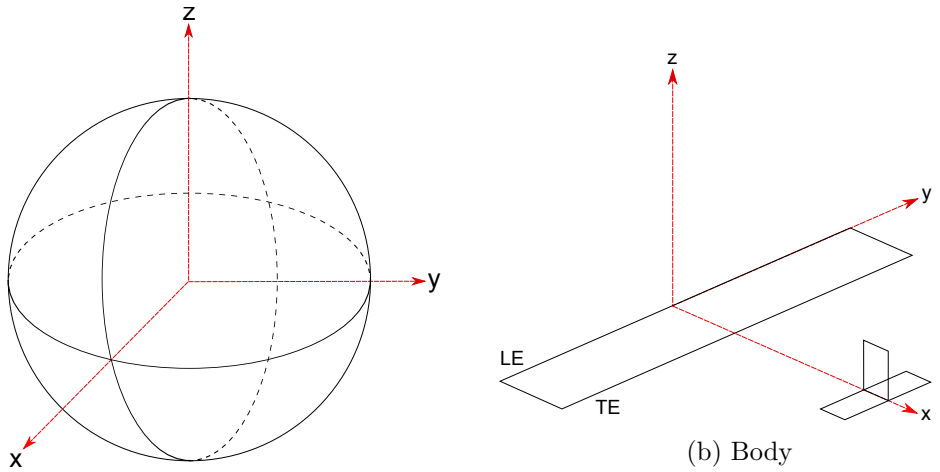

(a) Earth

(b) Body

Figure 1.2: Reference frames

Chapter 2

Requirements

At the start of the project the team received a number of requirements and constraints. These requirements provided the team with a framework for their design and where to start. These requirements and constraints are given in this chapter. At the end of the report in chapter 17, a compliance matrix is given. In this matrix all requirements are checked if they are met.

The requirements are structured in a requirement discovery tree (RDT). This tree was divided in two main branches, namely the technical requirement and the mission constraint branch. The technical requirements part consists of several specific requirements which are grouped in the operational, structural, flight condition and mission output subsections. The constraints part is divided in performance, safety, durability, sustainability, cost and efficiency and other.

The three most important requirements are the following:

- Power generation of 40 kW in the *traction* phase;
- Minimization of cost over mechanical power ratio;
- Optimization of energy production over pumping cycle time.

The requirement discovery trees are given in figure 2.1 and 2.2

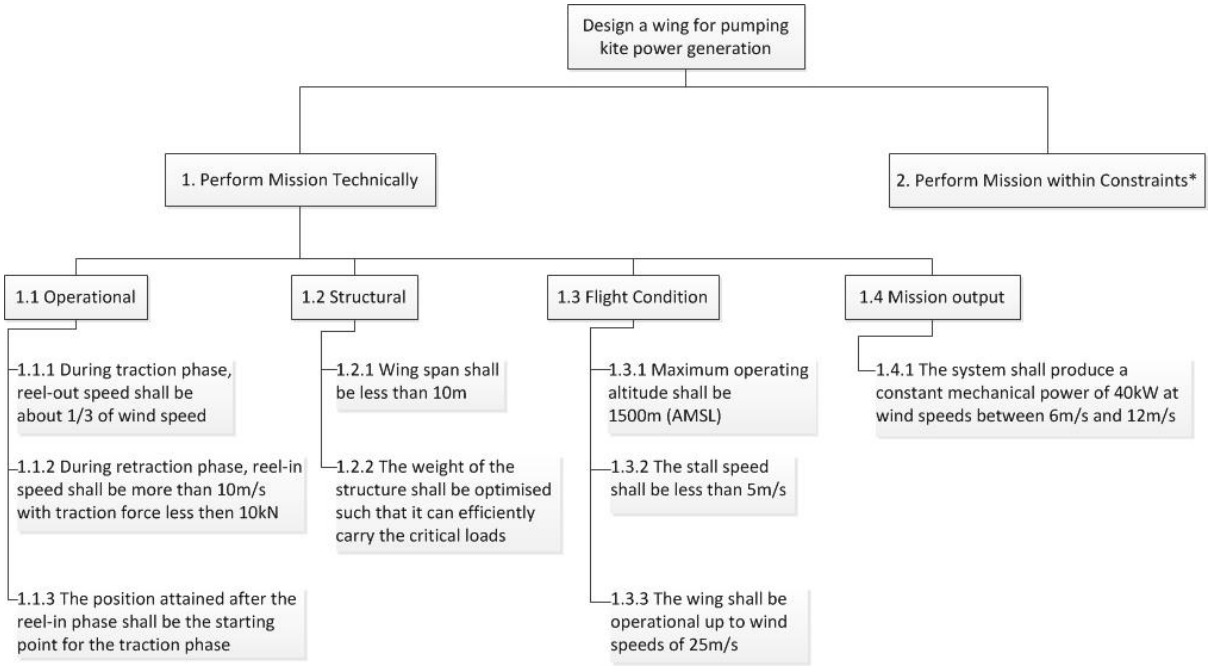

Figure 2.1: RDT with technical requirements

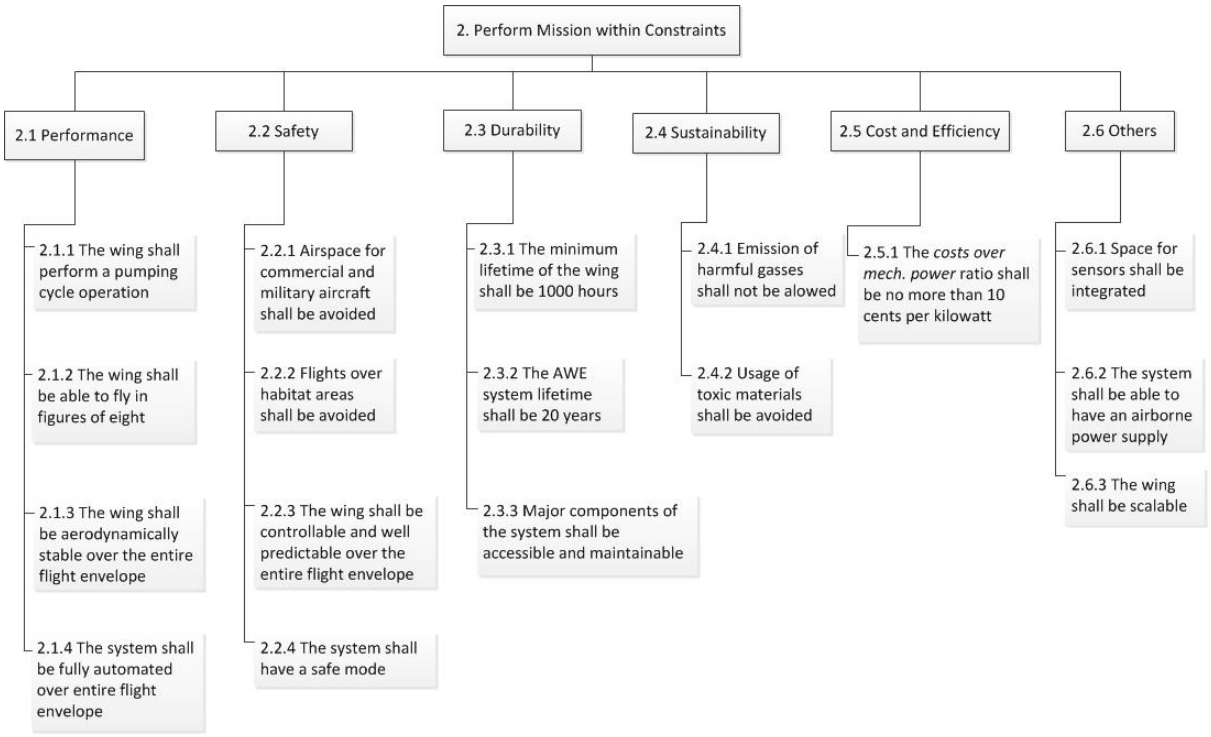

Figure 2.2: RDT with mission constraints

Part I

Design details

Chapter 3

Overall characteristics

In this chapter the final overall design is shortly summarized. This is done so that the methods with which the team came to this design can be understood with keeping the final design in mind. In section 3.1 the general configuration is described, together with the physical dimensions of the kite. In this section the construction and some aerodynamic characteristics are also explained. In section 3.2 the mass and electrical power budgets are presented.

3.1 Configuration and layout

In the midterm phase, five concepts were generated using a morphological chart. These concepts were evaluated and a trade-off was made based on the scores that were given to these different characteristics. From this trade-off the 'rigid conventional' concept was the winner. It is called 'rigid' because all structural parts are rigid, instead of some concepts that were partly flexible. 'Conventional' was because the kite is very similar to a 'standard' aircraft; with a wing, a fuselage and a tail. The big difference is that there is no part of the fuselage in front of the main wing and that the fuselage itself is significantly smaller than on a normal aircraft, since it does not have to carry any payload or fuel; it only provides the structural connection between wing and tail. The design is shown in the render in figure 3.1 and the top and side view in figure 3.2.

3.1.1 Wing

The kite has a span of ten meters. This was the maximum given in the requirements and to achieve an as large as possible aspect ratio for aerodynamic efficiency, this span is used. The wing was sized using the power equations given in chapter 4. The surface area of the wing is $12.7\,\mathrm{m}^2$. It has a taper ratio of 0.4, to approximate an elliptical lift distribution with a wing that has a single taper ratio. It has no quarter chord sweep and $2\,\mathrm{deg}$ of dihedral to improve roll stability. The wing's parameters are summarized in table 3.1.

The wing has the Wortmann FX73-CL3-152 airfoil. This was chosen for its very high $C_{\mathrm{L}_{\mathrm{max}}}$, as described in section 4.2. It also has a larger thickness than the previously selected airfoil, which is beneficial for its structural efficiency. The airfoil is shown in figure 3.3.

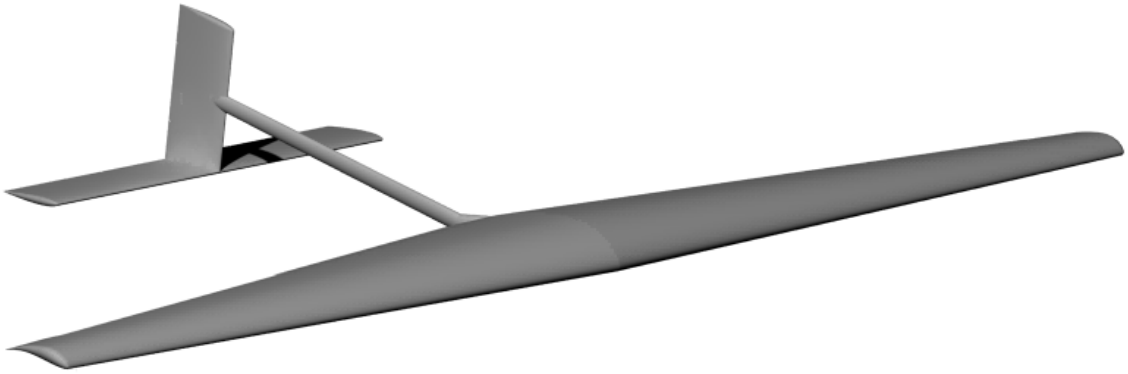

Figure 3.1: Overall picture of the kite

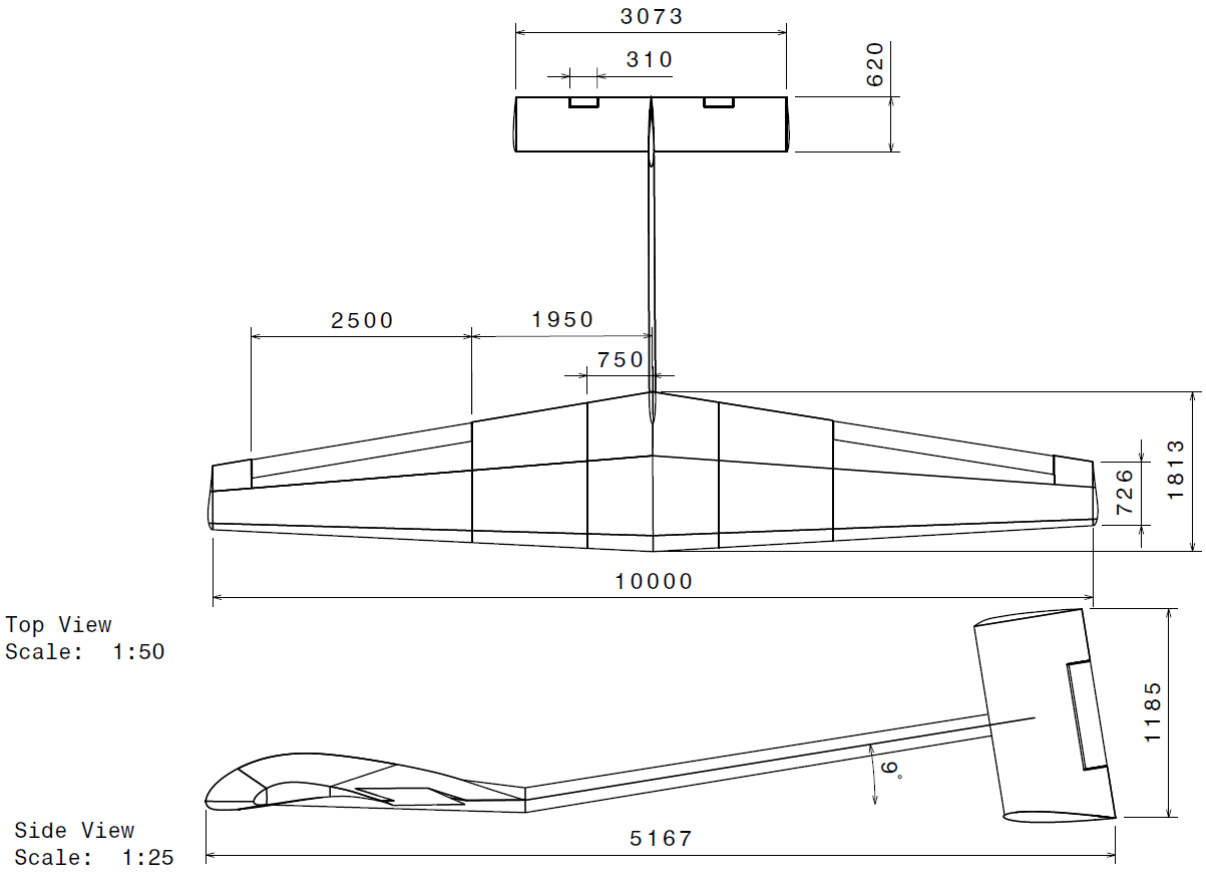

Figure 3.2: Isometric view of the kite with on the top-view(top) and side view(bottom)

Table 3.1: Wing sizing results

Parameter	Value
Surface area [m^2]	12.7
Span [m]	10
Root chord [m]	1.814
Taper ratio [-]	0.4
Aspect ratio [-]	7.88

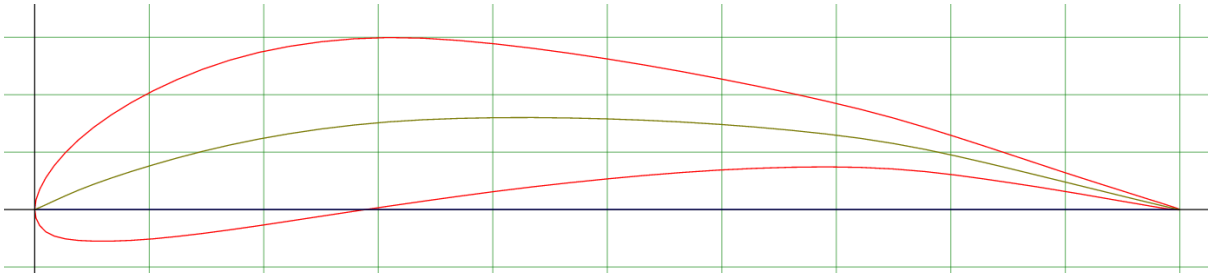

Figure 3.3: Wortmann FX73-CL3-152 airfoil

The outer parts of the main wing trailing edge are taken op by ailerons. These run from 0.41 % span to 0.91 % span and are 15 % of the local wing chord.

The main wing has a wingbox from 0.1 c to 0.6 c, where the skin of the wing will form an integral part of the wingbox. The wing will be constructed out of four panels and three ribs per side. The panel division as displayed in figure 3.4 is determined for ease of assembly and minimization of mold size.

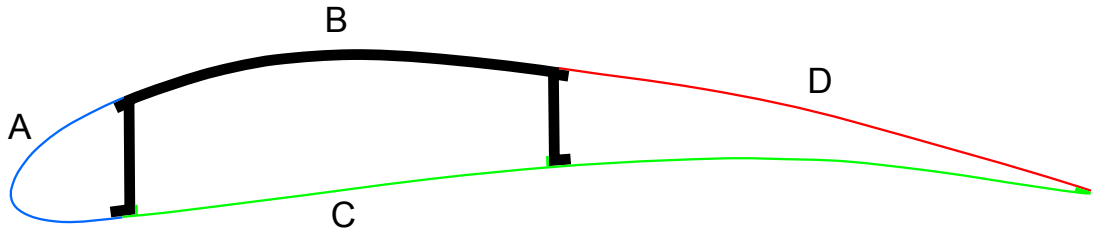

Figure 3.4: Panel division for the production of the main wing

Segment B will be the main load bearing structure of the wing as the only piece of sandwich material. Combined with the left side of segment C it will form the wingbox, and it will be used to mount all other panels of the wingbox on. It will be produced as a simple U-shaped panel on which mounting brackets are attached later. These brackets can then be mounted such that the skin of all panels will be flush after assembly.

Before mounting any of the panels the ribs can be inserted into segment A and glued in place at their respective locations, at the wingtip, and 3.05 m, and 4.25 m from the tip. The ribs consist of thin flanged plates with the shape of the wingbox at the front and rear section of the airfoil. They can be glued into segment B, and to the front and rear of the section. These ribs provide stiffness at the bridle connection points, and reduce the free length of the skin by constraining it, thus increasing the buckling load.

Segment C can then be attached to the assembly. It is produced as a single plate and is glued to the bottom side of segment B. A piece of structural foam can then be glued to the

rear edge of segment C, to provide a bonding surface for segment D. Finally segment A is glued to the mounting brackets of segment B, to complete the wing. During testing phase the bonding process may also be replaced with a less permanent attachment method, to improve the maintainability of the kite. A cutout will be made in the skin panels between the outer ribs to place the ailerons. These can then be mounted between these ribs.

3.1.2 Tail boom

The tail boom connects the tail to the main wing. The tail boom is a beam with elliptical cross section that runs from the thickest part of the main wing up to the thickest part of the vertical tail. At the main wing, the height of the boom will be equal to the thickness of the main wing airfoil and at the tail the boom has the width of the vertical tail airfoil thickness. Along the entire beam, the height of the beam is twice the width. In figure 3.2 the dimensions are displayed. The horizontal tail is connected to the tail boom through the vertical tailplane.

At the end of the main wing is has a 9 deg upward deflection. This was done because the kite flies at high angles of attack over a large operational range. By sweeping the 'body' upward, the tail is kept more tangent to the flow, decreasing the drag of the kite system significantly. Because the horizontal tailplane is at the same level as the main wing, the tail boom connects to the vertical tailplane almost halfway, as can be seen in figure 3.1.

3.1.3 Tail surfaces

The horizontal tail has a NACA 0010 airfoil with a 0.62 m chord and a 3.07 m span. .62 m of this span is elevator, divided over 2 surfaces which are separated due to the connection with the vertical tailplane. It has a 3.5 deg incidence angle over the main wing.

The vertical tail also has the symmetric NACA 0010 airfoil. It has a span of 1.2 m and the same chord as the horizontal tail. Again, 50 % of the span is taken up by a rudder which has a chord of 0.123 m.

The tail surfaces are constructed much easier than the main wing in order to reduce cost. As the loads on the these surfaces is smaller than on the main wing, the structural integrity of these parts can be assured by using a CFRP tube. Tho this tube the actuators for the control surfaces will be connected. The tubes will be covered by foam which is cut to the required shape beforehand. To finish of, the foam will be covered by a minimal layer of CFRP to provide more durability and a smooth surface.

The control surfaces will be constructed in the same way, with the only difference that they will be completely closed (the actuator connection point will be on the outside of the flaps).

3.2 Engineering budgets

In order to keep track of the resources available to the designers in an engineering project, an engineering budget is developed. This budget is made for the system mass and electrical power and is used for the sizing of components.

3.2.1 Mass budget allocation

To calculate the mass of the kite, a model is created in a CAD program - CATIA. Using this model, the volumes of the individual sections are found using the program and from this, the weight of the individual sections can be found. The mass of the kite is found to be as shown in table 3.2. The density values used to determine the section weights are 1400 kg/m^3 for CFRP and 32 kg/m^3 for foam core, with an additional resin absorption of 75 g/m^2 for surface area exposed to the facing.

Table 3.2: The mass breakdown of the kite

Section	Mass [kg]
Horizontal tail	2.38
Vertical tail	1.09
Body	2.35
Wing	22.62
Aileron	2.34
Electronics	7.20
Total	37.98

No contingency factor has been included in these calculations, and an additional total of 3 kg is expected for connection points between the body and the wings, structure of the control surfaces and structure of the tail sections.

3.2.2 Component mass budget allocation

To control the kite operations, a series of systems are placed within the kite structure. These include the components of the kite control system, actuators for the control surfaces, batteries to power the system, wiring and sensors. These weights contribute to the overall weight of the kite and are shown in table 3.3.

Table 3.3: The weights of the control components of the kite

Component	Mass [kg]
On-board control computer	0.3
Batteries	2
Turbine	0.5
Wiring	1
Sensors	0.4
Transceiver	0.5
Actuators	2.5
Total	7.2

3.2.3 Power budget allocation

To receive proper feedback to aid the control of the kite, a series of sensors are employed. These are the attitude sensors, GPS (global positioning system) sensors and wireless transceivers [5]. The values of these components are based on research of the available components in the market,

and the actuators are recommended by the Kite Power 2.0 team. A power budget of these electrical components is generated and shown in table 3.4.

Table 3.4: The power consumed by the electrical components used in kite control

Component	Power [W]
Attitude sensors	1.6 [6]
Wireless transceiver	0.02
GPS sensors	0.271
Actuators	68
Total	69.9

3.2.4 Sizing the turbine

The components connected to the kite control unit are run on a power system that is fed by a battery pack which is in turn charged by a turbine. This turbine has to provide the essential power required to run this system.

The power required to run the kite is set at 100 W. Using this value, calculating the size of the turbine is based on the power equation for the turbine. This is illustrated as [7].

$$P_{\mathrm{a}} = \frac{1}{2}\rho A V^3 C_{\mathrm{P}} \tag{3.1}$$

Where: ρ is the air density $^{\mathrm{kg}}/_{\mathrm{m}^3}$, S is the swept area in m^2, V is the Wind velocity $^{\mathrm{m}}/_{\mathrm{s}}$ and C_{P} the Power coefficient, an indication of the energy carried by the wind that can be extracted by the wind turbine. The theoretical maximum achievable C_{P} is 0.59 and is known as the Betz Limit [8].

To find the size of this turbine, the swept area is calculated at a C_{P} of 0.4. The velocity ranges between 32 - 40 $^{\mathrm{m}}/_{\mathrm{s}}$. The density ranges from 1.168 - 1.204 $^{\mathrm{kg}}/_{\mathrm{m}^3}$. The turbine radius r_{t} is sized at lowest density and lowest velocity, which is at the highest altitude.

$$r_{\mathrm{t}} = \sqrt{\frac{2P_{\mathrm{a}}}{\rho S V^3 C_{\mathrm{P}} \pi}} \tag{3.2}$$

Using the values of 32 $^{\mathrm{m}}/_{\mathrm{s}}$ and 1.168 $^{\mathrm{kg}}/_{\mathrm{m}^3}$, the turbine is found to have a radius of 6.45 cm. The size of this turbine is seemingly small but this is because it is just required to provide power to the components of the kite. Should the kite design evolve to require turbine assisted take-off, the turbine can be re-sized following the same procedure.

Chapter 4

Aerodynamics

In this chapter the aerodynamic sizing of the kite is presented. The iteration process between power output, lift coefficient C_L, projected area S_{proj} and altitude h is largely influenced by the tether drag. Therefore first this influence of drag will be explained. Also the influence of dirt on the wing has been investigated, solutions to this problem are presented. From the iteration process, an operating altitude can be found resulting in a 40 kW power output during reel-out. Then, a search for an airfoil with a higher $C_{L_{max}}$ is conducted, using the iteration between the power equation and the aerodynamic characteristics that are computed with the XFLR5 software.

4.1 Influence of drag

In this section the influence of the drag of the tether to the complete kite system is clarified. This will show that tether drag has a large influence on the power output during reel-out and the apparent kite velocity. To come up with the power output the numerical method presented in the Mid-Term report is used [9]. This method is also used during the iteration process for the improvement of the final design of the rigid conventional kite. Also the numerical method is improved by taking into account the standard atmosphere, where air density decreases at increasing altitude.

4.1.1 Wind velocity at altitude

The maximum tether length for this AWE system is700 m, the maximum attainable altitude can therefore be 700 m if the elevation angle is θ 90 deg (though very uncommon, it could be possible during parking mode). Between ground altitude and 700 m the Earth wind velocity is affected by ground friction, turbulence and heat differences, as this range is within the planetary boundary layer [4]. The power law gradient, see equation 4.1 and shown in figure 4.1, is used to analytically find the wind velocity at different altitude in the planetary boundary layer. This method is based upon empirical data and is proposed in chapter five of the book on airborne wind energy [4]. As explained in this chapter it has to be kept in mind that above 500 m low jet streams may occur, resulting in a significant increase in wind speed and both daily and seasonal effects cause deviations from this wind gradient. The ground wind velocity $V_{w,0}$ of is kept as an average of 5 m/s at $h_0 = 6$ m. This is in line with wind velocity data presented on page 11

of [10]. In this paper the wind data from Lindenberg, midland Germany, shows comparable wind velocities up to 300 m.

$$V_{\mathrm{w}} = V_{\mathrm{w},0} \left(\frac{h}{h_0} \right)^{0.14} \tag{4.1}$$

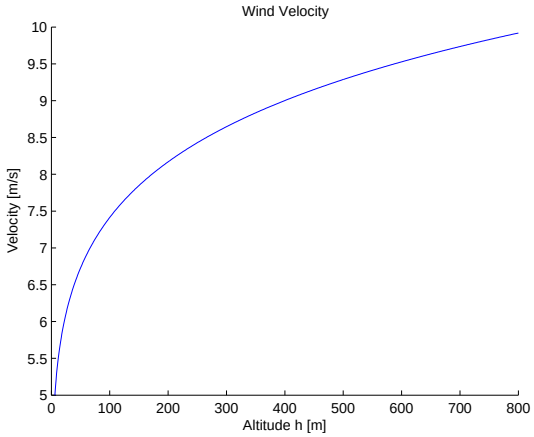

Figure 4.1: Wind velocity versus altitude

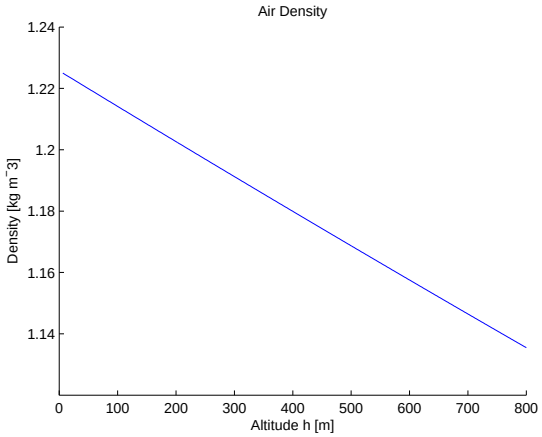

Figure 4.2: Atmospheric density versus altitude

4.1.2 Atmospheric density at altitude

The air density at altitude is calculated according the International Standard Atmosphere (ISA) [11]. In table 4.1 the values according to the International Standard Atmosphere are given. After this the equations to come up with the air density at altitude h are stated, first for pressure 4.2, then for temperature 4.3 and finally density 4.4.

Table 4.1: Values according to ISA

Parameter	**Definition**	**Value**
p_0 [kPa]	Sea level standard atmospheric pressure	101.325
T_0 [K]	Sea level standard temperature	288.15
g [$^{\mathrm{m}}/_{\mathrm{s}^2}$]	Gravitational acceleration	9.81
κ [$^{\mathrm{K}}/_{\mathrm{m}}$]	Temperature lapse rate	0.0065
R [$^{\mathrm{J}}/_{\mathrm{mol}*\mathrm{K}}$]	Universal gas constant	8.31447
M [$^{\mathrm{kg}}/_{\mathrm{mol}}$]	Molar mass of air	0.0289644

$$p = p_0 \left(1 - \frac{\kappa h}{T_0} \right)^{\frac{gM}{R\kappa}} \tag{4.2}$$

$$T = T_0 - \kappa h \tag{4.3}$$

$$\rho = \frac{pM}{RT} \tag{4.4}$$

The air density versus altitude is plotted in figure 4.2.

4.1.3 Power output

Using both the analytical and numerical method explained in the Mid-Term report [9], the power output versus altitude can be plotted 4.3. Note that the numerical method results in lower values for the power output and is used for a more robust design. The simplified equations used for the numerical (4.8) and analytical (4.9) methods are shown below to clearly explain the results from the plot.

$$C_{\mathrm{D_t}} \approx 0.31 \frac{r d_{\mathrm{t}}}{S_{\mathrm{proj}}} C_{\mathrm{d_t}} \tag{4.5}$$

$$C_{\mathrm{D}} = C_{\mathrm{D_k}} + C_{\mathrm{D_t}} \tag{4.6}$$

$$F_{\mathrm{t_{max}}} = \frac{1}{2} \rho {V_{\mathrm{a}}}^2 S_{\mathrm{proj}} C_{\mathrm{D}} \sqrt{1 + \left(\frac{C_{\mathrm{L}}}{C_{\mathrm{D}}}\right)^2} \tag{4.7}$$

$$P_{\mathrm{num}} = \frac{1}{1.11} F_{\mathrm{t_{max}}} \frac{1}{3} V_{\mathrm{w}} \tag{4.8}$$

$$P_{\mathrm{ana}} = \frac{1}{1.11} \frac{2}{27} \rho S_{\mathrm{proj}} \frac{CL^3}{CD^2} {V_{\mathrm{w}}}^3 cos^3\theta \tag{4.9}$$

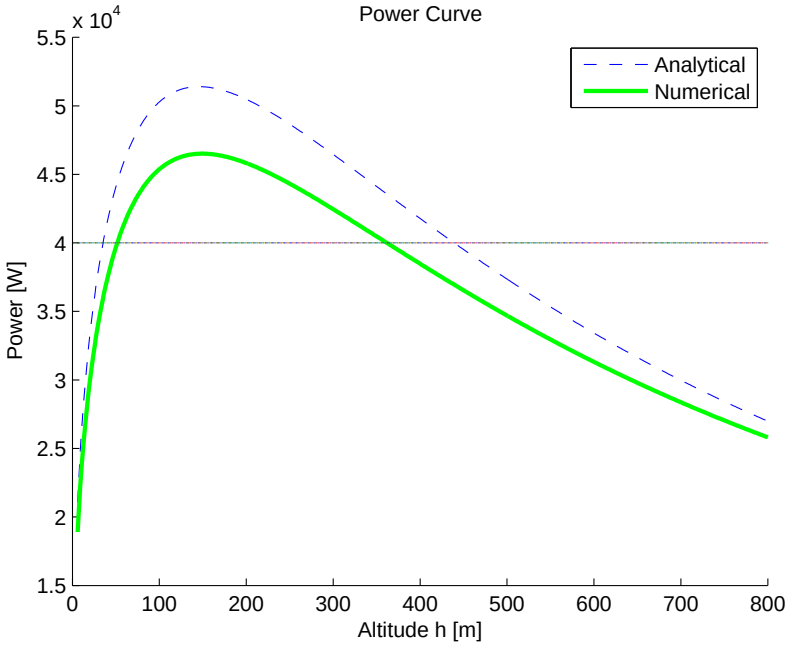

Figure 4.3: Power output versus altitude

In this plot a clear maximum can be seen for power output. Therefore for the final design and this operational range below 700 m the power output does not increase, at increasing altitude h above approximately 150 m. It would sound rather logical that power output increases with altitude, due to the increase in wind velocity V_{w} . However, flying at higher altitude results

in a longer tether. A longer tether length r causes an increase in tether drag C_{D_t} (equation 4.5), and therefore an increase in the total drag of the system C_D (equation 4.6). This largely influences the power output P_{num} (equation 4.8), such that a maximum power output is found at approximately 150 m.

The increase in drag of the tether C_{D_t} is shown in figure 4.4a. At 6 m altitude the length of the tether is zero, which shows the drag of only the kite C_{D_k}. At increasing altitude the contribution of kite drag C_{D_k} is only a fraction compared to the tether drag C_{D_t}.

At approximately 350 m altitude the required 40 kW during reel-out is generated. The kite will now fly its 8-figure trajectory above and below this altitude, resulting in an average 40 kW output during reel-out.

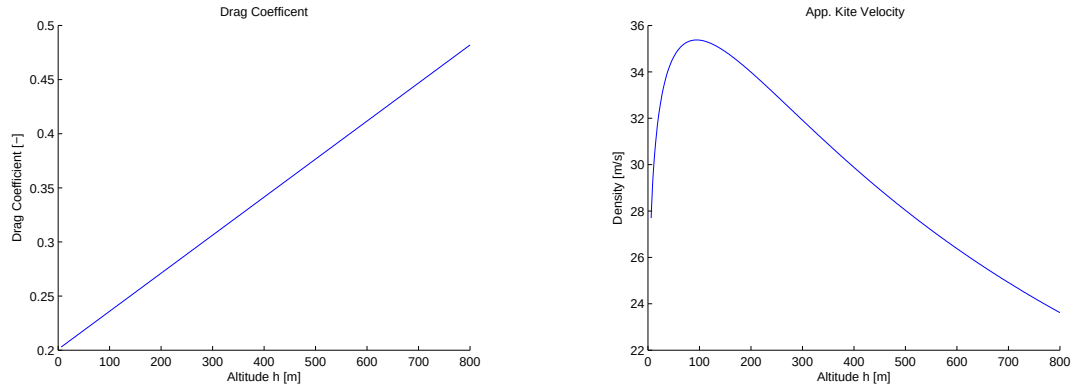

(a) Total kite drag

(b) Apparent kite velocity

Figure 4.4: Parameters variable with altitude

4.1.4 Apparent kite velocity

Using equation 4.10 the apparent kite velocity can be plotted versus kite altitude. This equation is also used in the numerical model, presented in the Mid-Term report [9]. The plot is shown in figure 4.4b. Again a clear maximum can be found in the curve. This for the same reason as for power output, which is the large contribution of tether drag to the total drag at increasing altitude. As can be seen in equation 4.10 the apparent kite velocity is dependent on the total drag C_D and V_w, causing a maximum in the curve.

$$V_a = (\cos\theta\cos\phi - \frac{1}{3})V_w\sqrt{1+\left(\frac{C_L}{C_D}\right)^2} \tag{4.10}$$

4.2 Airfoils

4.2.1 Main wing

In [9], the Wortmann FX63-137 was selected as the airfoil of choice for the kite. With the insights gained in this phase, the search for a higher $C_{L_{max}}$ continued and a new airfoil was found to be more beneficial. It is the Wortmann FX73-CL3-152. It has two main advantages

over the previously selected airfoil, namely a higher $C_{L_{max}}$ and a larger thickness ratio. These are 2.2 versus 2 and 15.2 % versus 13.7 %, respectively. The airfoil itself is shown in 4.5. The airfoil $C_l - \alpha$, $C_d - \alpha$ and $C_m - \alpha$ polars are shown in figures 4.6, 4.7 and 4.8, respectively.

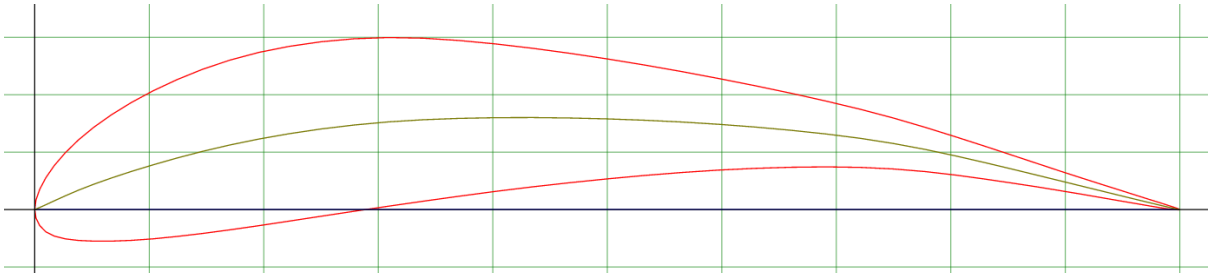

Figure 4.5: Wortmann FX73-CL3-152 airfoil

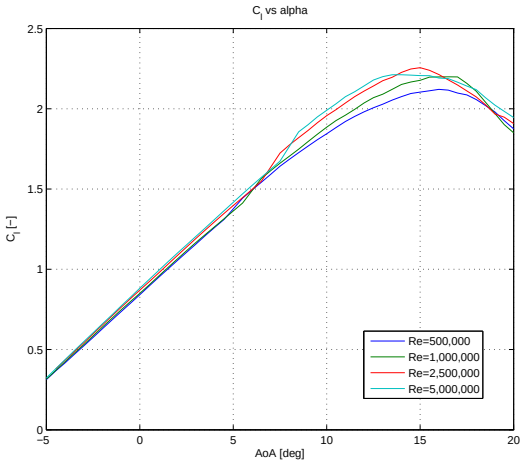

Figure 4.6: C_l vs α polar of the FX73-CL3-152 airfoil

4.2.2 Empennage

On both horizontal and vertical tail surfaces, the NACA 0010 symmetric airfoil is used. Its lift and drag polars are shown in figure 4.9 and 4.10

4.3 Wing sizing

The wing was sized in an iterative manner using the power equations given in section 4.1.3. This process is described in this section.

4.3.1 Process

The kite is sized to produce its minimum power requirement of 40 kW at its maximum tether length of 700 m. In this manner the requirement can be met in the full operational range, as explained in section 4.1.3.

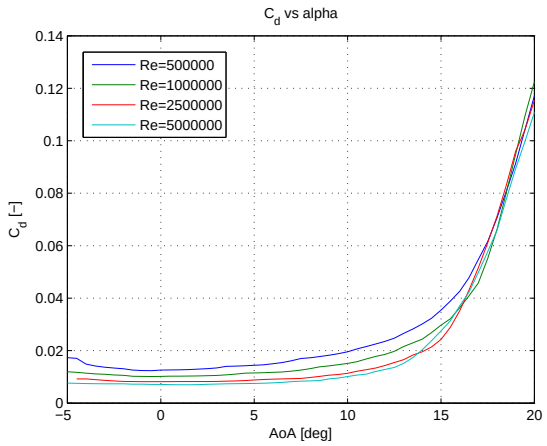

Figure 4.7: C_d vs α polar of the FX73-CL3-152 airfoil

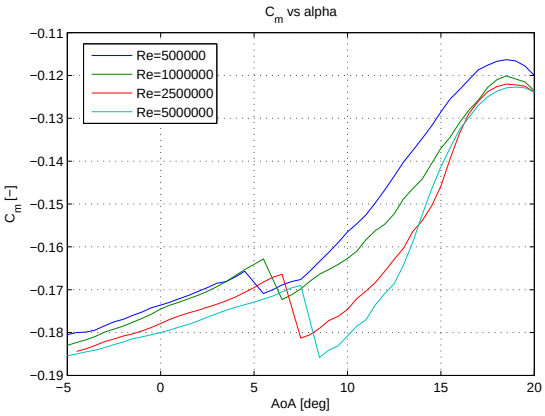

Figure 4.8: C_m vs α polar of the FX73-CL3-152 airfoil

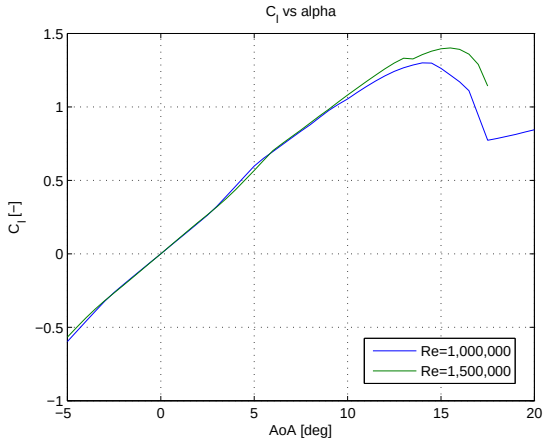

Figure 4.9: C_l vs α polar of NACA 0010 airfoil

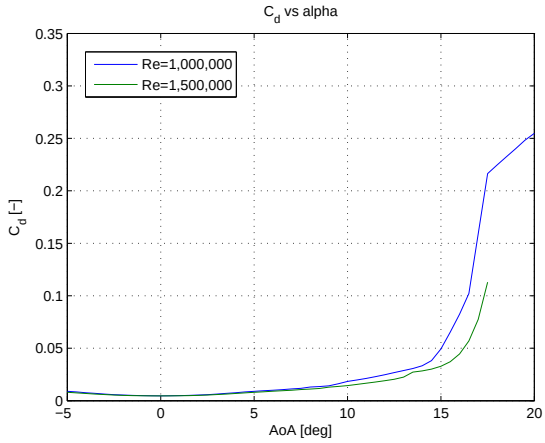

Figure 4.10: C_d vs α polar of NACA 0010 airfoil

The sizing iterations have been performed using the XFLR5 software and the power tool from section. This iteration process is shown in figure 4.11. The blue blocks are inputs that can be changed to find a power output that matches with the required 40 kW during reel-out. Orange blocks are inputs that are kept constant to simplify the iteration as they are equal for all concepts and do not vary significantly (such as density ρ and Reynolds number Re). Purple blocks define outputs of the XFLR5 software and the power tool. The FX73-CL3-152 airfoil selected in section 4.2 acts as an input for the XFLR5 software. This, combined with the orange and blue input blocks in the power tool, will give the power output at different heights.

4.3.2 Result

The results of the aerodynamic analysis combined with the power production analysis are presented in table 4.2. The wing itself is shown in figure 3.1.

The kite lift- and drag polars are shown in 4.12a and 4.12b. Especially the lift polar seems very linear. This is a shortcoming of XFLR5, because at some point the AoA is too large for some parts of the wing. Here it tries to find higher C_l values for the outer portions of the wing but

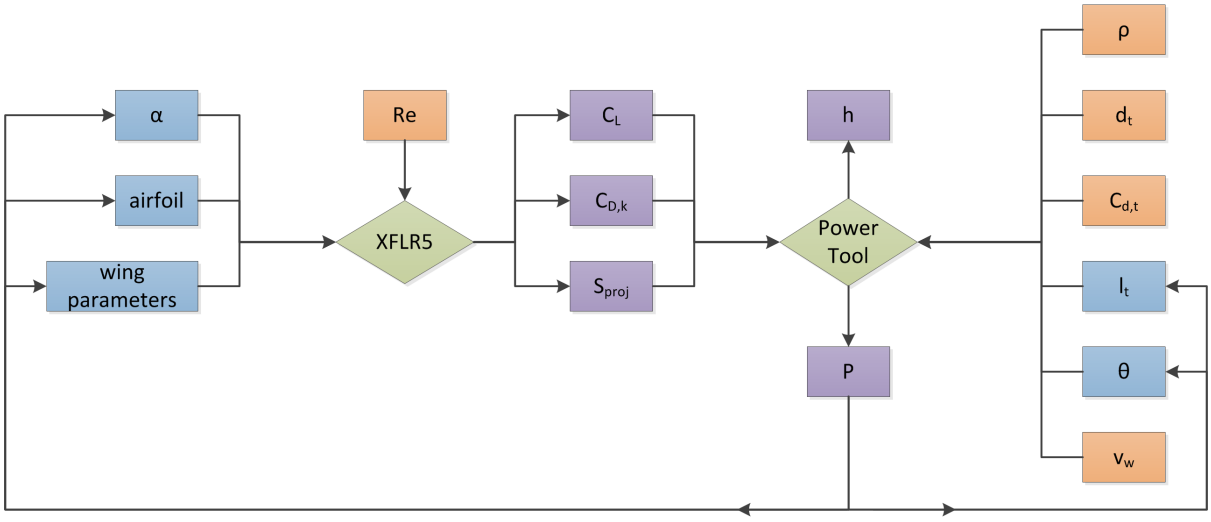

Figure 4.11: Flowchart of iteration process for wing sizing

Table 4.2: Wing sizing results

Parameter	Value
S [m^2]	12.7
b [m]	10
C_r [m]	1.814
λ [-]	0.4
A [-]	7.88

these values are not available, because the lower Re at this point makes the wingtips stall faster than the center. The moment polars are not treated here since there are evaluated in chapter 6.

4.4 Influence of dirt

A factor that also should be taken into account is the accumulation of dirt on the kite during operation in air. Dirt can be for example small insects that collide with the kite or dust particles. This accumulation of dirt increases the roughness of the airfoil surface, increasing the skin friction drag and degrading the aerodynamic performance of the kite (decreasing the C_{L}). Also at higher angles of attack, the skin friction constant for rough wings increases even more, as concluded in paper [12]. This results in a location shift of disturbances and transition point towards the leading edge. Therefore if the kite becomes rough due to dirt and would fly at high angle of attack (which is the case during reel-out), the airfoil surface will encounter turbulent flow for a larger part than a clean airfoil.

Due to dirt the aerodynamic properties become less, decreasing the lift coefficient of the airfoil. The lift coefficient at high angle of attack is the main parameter to power output, while the $C_{\mathrm{L}_{\max}}$ is the main parameter to V_{stall}. Therefore a rough airfoil results in lower power output during reel-out and a higher stall speed (worse take-off and landing properties). The method proposed to do a roughness sensitivity analysis is to evaluate the lift coefficient when the airfoil is clean versus rough in the XFLR5 software. As dirt on the wing would shift the transition

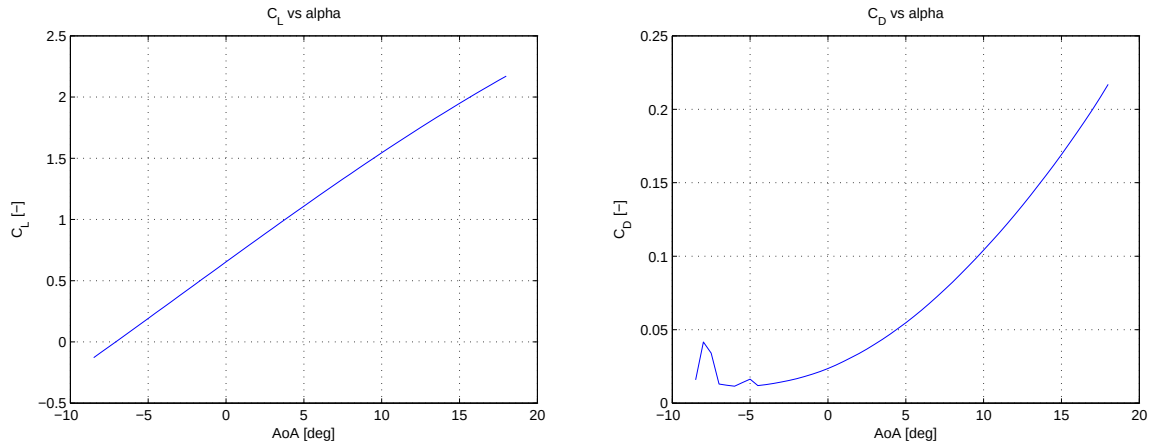

(a) C_{L} vs α polar

(b) C_{D} vs α polar

Figure 4.12: Lift and drag polars of the complete kite

point forward, a rough analysis is done by shifting the transition point to the leading edge (a worst case scenario) and evaluate what the aerodynamic properties become. This location for worst case scenario is put at $x_{\mathrm{cg}} = 10\%$ for the upper surface and $x_{\mathrm{cg}} = 15\%$ for the lower surface (needs to be aft the transition point in upper surface to be computable in XFLR5). This scenario is called worst case, comparing with paper [12] where the transition point for a wind turbine airfoil only shifts to $x_{\mathrm{cg}} = 30\%$ at higher angles of attack.

It must be mentioned that this analysis will only give an indication of performance between a clean and rough surface. There are many uncertainties, mainly due to at which location on the airfoil and how many dirt would accumulate resulting in a difficult to find location of transition point. As mentioned in paper [13] a rough surface near the trailing edge could even result in an increase in lift coefficient. Also in this analysis only the aerodynamic properties of the clean versus rough airfoil are compared, not for the complete kite system. Still this gives a good indication on how much the aerodynamic properties would decrease, resulting in an estimation for power loss and increase in stall speed.

The analysis is done for the airfoil with a Reynolds number kept at $Re = 3 \cdot 10^6$, based on an apparent kite velocity of approximately $V_{\mathrm{a}} \approx 35\,\mathrm{m/s}$ at an altitude of $h = 350\,\mathrm{m}$ (see also figure 4.4b). From the lift coefficient curves the $C_{\mathrm{l_{max}}}$ can be found, presented in table 4.3. There is an approximate maximum decrease of 0.15 in the lift coefficient of the airfoil as can be seen in figure 4.13, which will be used to estimate values for stall speed and power output for a kite system with dirt. Also the lift coefficient curve does not drops dramatically after reaching $C_{\mathrm{l_{max}}}$, which results in still good stall properties if the kite has accumulated dirt.

Drag increases with approximately 0.012 at V_{stall}, the drag coefficient is plotted in figure 4.14. This increase is negligible with respect to the drag of the kite as well as the drag of the complete system (large influence of tether drag to total drag, as explained in section 4.1).

Now the difference in V_{stall} and $h_{\mathrm{P}\approx 40\mathrm{kW}}$ are estimated using a decrease in the lift coefficient C_{L} of 0.15 in the power equation (equation 4.8). Stall speed V_{stall} is estimated using the stall speed equation 4.11 as given in the Mid-Term report [9] and would only increase with approximately $0.2\,\mathrm{m/s}$. The outcomes are shown in table 4.3. Flying at lower altitude with a rough wing can still produce up to 38 kW, just below the required 40 kW.

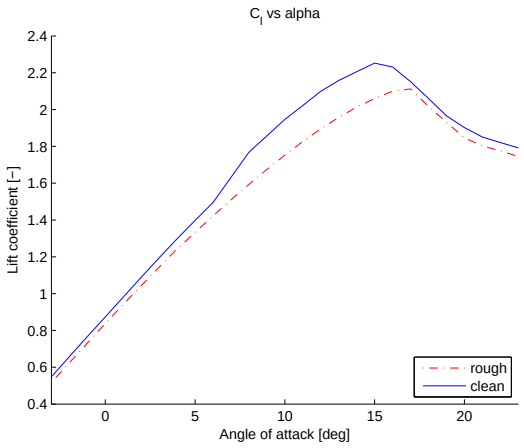

Figure 4.13: Clean versus rough lift coefficient

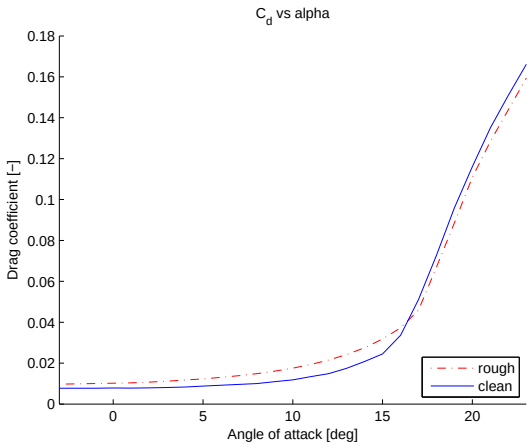

Figure 4.14: Clean versus rough drag coefficient

$$V_{\text{stall}} = \sqrt{\frac{2W}{C_{\text{L}_{\text{max}}} S \rho}} \tag{4.11}$$

Table 4.3: Clean versus rough airfoil

	Clean	Rough
$C_{\text{l}_{\text{max}}}$ -	2.25	2.10
$C_{\text{d}_{\text{k}}}$ -	0.02	0.037
V_{stall} m/s	4.9	5.1
$h_{\text{P}\approx 40\text{kW}}$ m	350	150

This method shows that the system would still be able to generate up to 38 kW if the wing accumulates dirt. If during a period of time more and more dirt accumulates, the kite system can still generate the required 40 kW by flying at lower altitude (with shorter tether length). During maintenance after landing the kite should be washed to remove the dirt. This also resolves the problem that the increased drag would influence its take-off properties.

4.5 Wing optimization

In this section further optimization of the wing has been investigated. This was done using different concepts: planform optimization, winglets and high lift devices.

4.5.1 Planform

To achieve an optimal elliptical lift distribution, for minimum induced drag, an elliptical planform can be used. This would be a solution with direct results. However, since this is very complex to manufacture, other methods are looked for. The elliptical planform can also be approximated with a taper ratio. The entire wing can be given one taper ratio or different sections with different ratios. The baseline for this planform was the concept wing with a $\lambda = 0.4$. For a

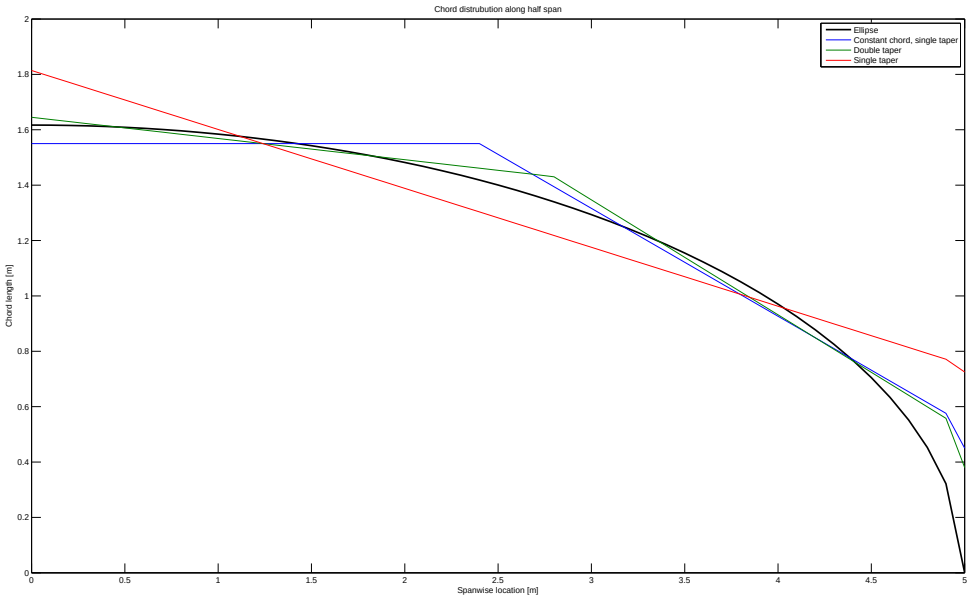

Figure 4.15: Spanwise chord distribution of new shapes versus perfect ellipse

single tapered wing this is already the optimum. The chord distributions of the new planforms were developed to closely approximate a quarter ellipse with surface area $S/2 = 6.35\,\mathrm{m}^2$. This ellipse is given by equation 4.12.

$$\frac{x^2}{a^2} + \frac{y^2}{b^2} = 1 \tag{4.12}$$

With a =5 m and b =1.62 m.

The first new planform has a portion of constant chord up to approximately half-span and then tapers to the tip. The power increase with the same surface area was only 200 W. The second new planform had two differently tapered sections. Although it would make sense that the ellipse can be approximated much better using this planform, the power increase was only 100 W. Both chord distributions, along with the baseline planform and the perfect ellipse are shown in figure 4.15.

Because both new planforms would be more complex to manufacture and the gain in power is only little, these options are not investigated in further detail.

4.5.2 Winglets

Winglets are small vertical wing sections on the wingtips. They are created to reduce induced drag by alleviating and displacing tip vortices. The first approximation was done, based on dimension ratios of sailplane airfoils. From this approximation, an initial guess was taken and then refined iteratively in accordance with the process shown in section 4.3. The final winglet layout is shown in figure 4.16. It is one tip chord high, $2/3c_\mathrm{t}$ at the winglet root and $1/3c_\mathrm{t}$ at

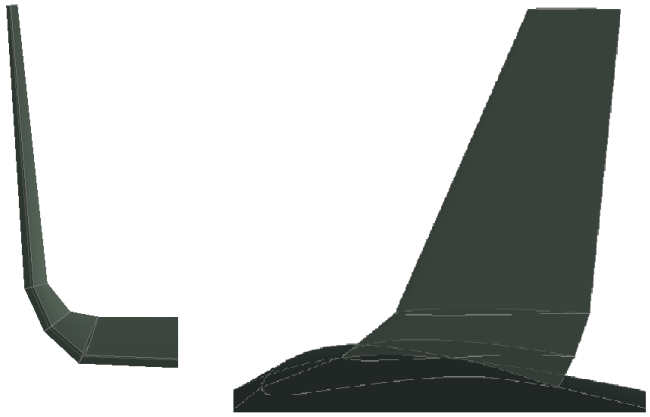

Figure 4.16: Winglet layout

the winglet tip. The airfoil chosen on the winglet was the PSU-90-125. The new power with this winglet was approximately 43.6 kW. This gain is too low to justify the increase in weight and complexity of the system. Also a resizing would result in a lower wing area, but with the added weight of the winglet, compromising V_{stall}.

4.5.3 High lift devices

For the reduction of V_{stall}, high lift devices were investigated. This was done using the XLFR5 function for flaps. The outcomes were, that although the maximum lift coefficient was reached at a lower angle of attack, the $C_{\text{L}_{\text{max}}}$ did not increase. This is because of the characteristics of the airfoil, which is already highly cambered. The increase in camber due to a flap causes the flow to separate early, which in turn limits the α-range. XFLR5 does not have any options for gaps between wing and flap. This would re-energize the boundary layer causing possible reattachment of the flow to the flap. Also the extra weight and complexity of such a system overshadows the benefits.

Chapter 5

Structure

In this chapter the structure of the kite is determined; which materials it will consist of, and how much material is required to meet safety standards and operational requirements. Since the kite is mostly constructed out of carbon fiber reinforced polymer (CFRP) most of the calculations will consider the minimal obtainable wall thicknesses before ultimate failure or buckling occurs. In section 5.1 the loading conditions, material properties, stress and failure calculations of the main wing will be presented. This is followed by the structural sizing of the tailboom in section 5.2.

5.1 Main wing

In this section the design of the structure of the kite will be presented. In section 5.1.1 the wingbox loadcase will be determined, followed by an investigation of material properties that are used for further calculations in section 5.1.2. The internal stress and buckling calculations methods are explained in sections 5.1.3 and 5.1.4.

5.1.1 Load case

The load case is determined by the maximum lift distribution, the drag distribution, and the bridle forces. Both bridle forces are assumed equal, leading to symmetry. Because of this symmetry will be assumed to reduce the problem to half the wing.

The kite will be designed with two attachment points since this appeared optimal in earlier analysis done on the problem. The bridling will not be designed to the highest detail, because this is a multidisciplinary design optimization problem.

The free body diagrams of the tapered wing are displayed in figures 5.1a and 5.1b. The total lift force it needs to transfer is 20 kN, which is multiplied with a safety factor of 2. This safety factor is determined by taking a safety factor of 1.44 on the wind speed due to gusts, since load increases quadratically to the windspeed. The lift force distribution over half the span from the tip for a total lift force of 40 kN is then described by:

$$q_l = 18000\sqrt{1 - \left(\frac{y}{5}\right)^2} \tag{5.1}$$

The distributed drag force q_d follows from the viscous drag distribution and the induced drag distribution. An elliptical drag distribution which integrates to the same total drag as found in XFLR5 is used since an accurate definition for this distribution could not be found. This should have relatively low consequences to the safety margins of the design, since the lift force is approximately 10 times higher than the drag. The spanwise location of the bridle force F_b can be chosen freely, and is limited chordwise by stability requirements.

With these load distributions and the bridle location from the final design iteration the loads result in the normal force, shear force and moment distributions displayed in 5.2.

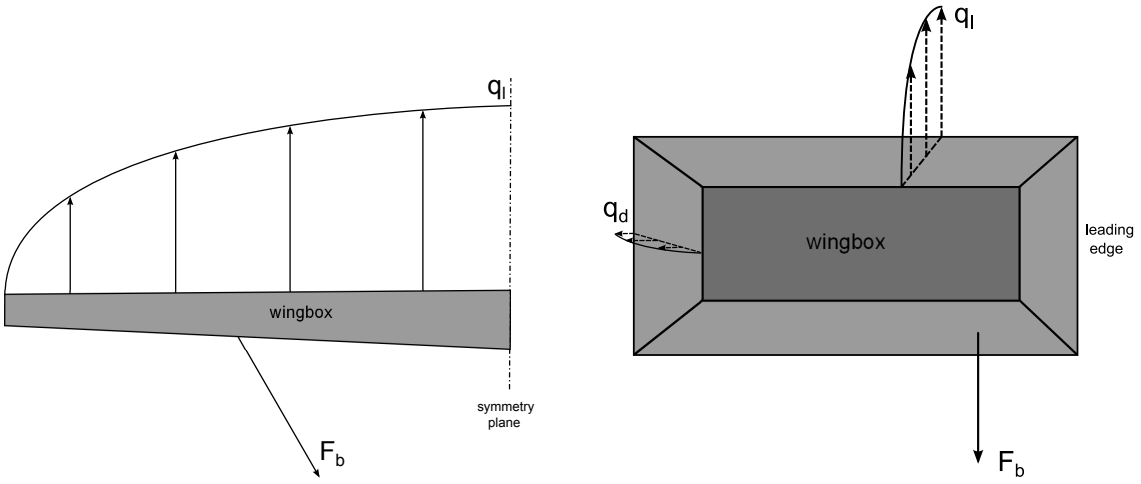

(a) Front view (b) Side view

Figure 5.1: Free body diagrams

5.1.2 Material properties

This section contains properties of materials for the design of the wing. The scope of materials that are considered consists of composite fiber materials and sandwich core materials. These materials are selected for a range of requirements.

A laminate needs to have at least four orientations of fibers, 0, 90, 45 and -45 deg. A rule of thumb is that it should contain at least 10% of fibers in any of these directions in order to comply with secondary loads.

The laminate should also be balanced and symmetric, otherwise unwanted coupling effects occur between normal and bending strains. These coupling effects could also warp the structure out of shape as it cools down from curing. A balanced layup is where there is an equal number of positive angled plies as negative angled plies. A laminate is symmetric when the plies above the mid-plane are a mirror image of those below the mid-plane. This means that for a laminate to be effective, at least 8 plies are required.

The forces in the wingbox appear to be very low from analysis done during the midterm phase. As a result the initial sizing for skin thickness is around 0.5 mm.

Using the fact that weaves are on average 1 mm thick per $^{kg}/_{m^2}$ the average weight of the weave should be 125 $^{g}/_{m^2}$ or less, since a weave consists of two plies.

The type of fiber should be selected for the specific load case. In this case it is approximately

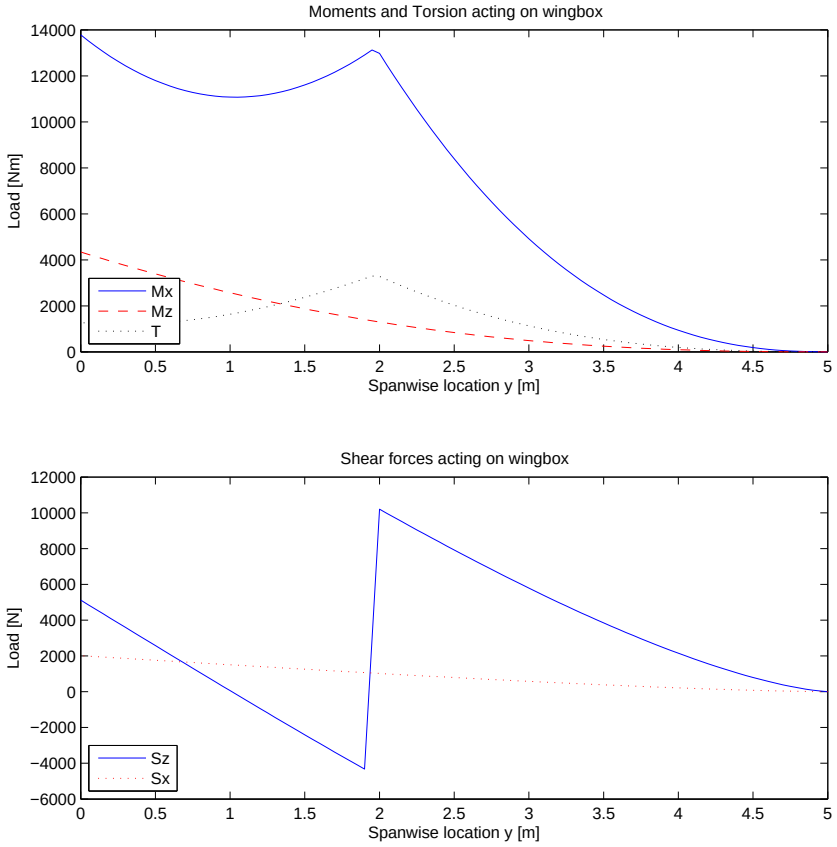

Figure 5.2: Loads on wingbox structure as a function of y-location

200 MPa of maximum von Mises stress in an isotropic approximation of the structure. The maximum compressive force is approximately 31 kN, so buckling will likely be a critical case for the wingbox. In material selection this means that stiffness is a more important characteristic than strength for the material. This almost exclusively leaves different types of carbon fibers, a combination of high strength and high stiffness fibers could be used. In table 5.1 properties of commonly used fibers can be found, the Torayca T300, T700S and M40J. The T300 is a commonly available fiber with average properties, The T700S is a high strength fiber and the M40J is a high stiffness fiber. Datasheets for these fibers can also be found in website [1]. A choice between these fibers will follow from section 5.1.3.

Table 5.1: CFRP material properties

	Fiber data			Laminate data		
Fiber Type	T300	T700S	M40J	T300	T700S	M40J
Tensile Strength [MPa]	3,530	4,900	4,410	1,860	2,550	2,450
Young's Modulus [GPa]	230	230	377	135	135	230
Maximum Strain [%]	1.5%	2.1%	1.2%	1.3%	1.7%	1.1%

Another countermeasure to buckling is to add geometrical stiffness to the skins, this can be

[1] URL: `http://www.toraycfa.cm/product` [cited 14 january 2015]

done with either stiffeners or by using sandwich structure. For this reason core materials would also be needed. Within the lightweight category of materials there are two major categories of materials, honeycomb and construction foam. However honeycomb comes with a few disadvantages, firstly it is not compatible with resin infusion techniques, which would be a cheap option for producing such large composite surfaces. It also requires multiple cure cycles, meaning it would be significantly more expensive to produce with than foams. Furthermore, production with honeycombs is not suitable for these thin laminates, since the production would very easily induce dimpling of the skin into the honeycomb cells. This leaves foam as the only suitable option, however a choice is to be made between two types. Since such a large surface of the wing would consist of sandwich structure, resin absorption of the foam could result in a large addition of weight. As a solution two foam materials will be presented in Table 5.2, Rohacell IGF31 and RIMA51. Rohacell IGF31 is an extremely low density foam, and RIMA51 is a slightly heavier foam which has a lower resin absorption per surface area. The datasheets of these materials can be found in website[2] and the resin absorption values have been obtained in communication with the company.

Table 5.2: Core material properties

Rohacell foam	IGF31	RIMA51
Density [kg/m^3]	32	52
Resin Absorption [g/m^2]	125	75
Young's Modulus [MPa]	36	75
Shear Modulus [MPa]	13	24
Tensile Strength [MPa]	1.0	1.6
Compressive Strength [MPa]	0.4	0.8
Shear Strength [MPa]	0.4	0.8

Since the properties for these materials are not extremely important when dealing with distributed loads the lightest solution per surface area will be chosen. In section 5.1.4 a core thickness of 10 mm will be chosen for the sandwich panels, so comparing the weight of these foams for this thickness yields:

$$32 \cdot 10 + 2 \cdot 125 = 570 g/m^2$$
$$52 \cdot 10 + 2 \cdot 75 = 670 g/m^2$$

It follows that for these thicknesses IGF31 proves lighter, and is the better option assuming it is capable of carrying the loads.

5.1.3 Stress analysis

For the stress analysis the wing structure is modeled as multiple data-points. At each of these data-points the stress is calculated. The calculations are based on chapter 20 of Aircraft Structural Analysis [14].

At each spanwise location, the total number of spanwise locations is n, the wing box outline is constructed using the airfoil data points and the front and rear spar positions. The portions of

[2] URL: `http://www.rohacell.com` [cited 14 january 2015]

the skin located in front of the front spar and behind the rear spar are assumed to not carry any load.

This wingbox outline is divided into multiple areas, booms (B), using the thicknesses of the skin and spars and the distances between the individual data points. The total number of booms at each spanwise location is m. The stiffener cross-sectional area is added to the booms which are located on the stiffener positions. In this way, the effect of stiffeners on the stress distribution can also be examined. Using the boom areas, the structural characteristics like neutral axes and area moments of inertia can be calculated.

The cross-sectional area (A_{cs})of the wingbox at each span wise location is calculated according to equation 5.2.

$$A_{cs} = \sum_{i=1}^{m} B_i \tag{5.2}$$

The vertical ($\bar{x}$) and horizontal neutral axis position ($\bar{z}$) of the wingbox at each spanwise location are calculated according to equation 5.3 and equation 5.4 respectively. The shear axes are assumed to coincide with the neutral axes.

$$\bar{x} = \frac{\sum_{i=1}^{m} B_i z_i}{A_{cs}} \tag{5.3}$$

$$\bar{z} = \frac{\sum_{i=1}^{m} B_i \xi}{A_{cs}} \tag{5.4}$$

The area moment of inertia around the horizontal axis (I_{xx}), the vertical axis (I_{zz})and the asymmetric area moment of inertia (I_{xz}) of the wingbox at each span wise location are calculated according to equation 5.5, 5.6 and equation 5.7 respectively.

$$I_{xx} = \sum_{i=1}^{m} B_i (z_i - \bar{x})^2 \tag{5.5}$$

$$I_{zz} = \sum_{i=1}^{m} B_i (\xi - \bar{z})^2 \tag{5.6}$$

$$I_{xz} = \sum_{i=1}^{m} B_i (z_i - \bar{x})(\xi - \bar{z}) \tag{5.7}$$

Using the loads from section 5.1.1 and the structural properties, the stresses are calculated. First the bending stress (σ_b) is calculated at each boom position with equation 5.8

$$\sigma_b = \frac{M_z \cdot I_{xx} - M_x \cdot I_{xz}}{I_{xx} \cdot I_{zz} - {I_{xz}}^2} \cdot (x - \bar{z}) + \frac{M_x \cdot I_{zz} - M_z \cdot I_{xz}}{I_{xx} \cdot I_{zz} - {I_{xz}}^2} \cdot (z - \bar{x}) \tag{5.8}$$

Before the shear stresses are calculated, the shear flows resulting from torsion and shear force are determined. The shear flow resulting from torsion (q_t) is calculated according to equation 5.9.

$$q_t = \frac{T}{2 \cdot A_{enclosed}} \tag{5.9}$$

The shear flow resulting from the shear force has two components; the open section shear flow (q_b) and the zero value of shear flow at the cut ($q_{s,0}$), which results from the eccentricity of the cut relative to the shear center. They are calculated according to equation 5.10 and 5.11. $A_{enclosed}$ is the enclosed area by the wing box, and x_{cut} is the x-location of the cut. And as mentioned before, the shear axes are assumed to be located on the neutral axes.

$$q_{s,0} = \frac{(z_{cut} - \bar{x})S_x + (x_{cut} - \bar{z})S_z}{2A_{enclosed}} \tag{5.10}$$

$$q_b = -\frac{S_x I_{xx} - S_z I_{xz}}{I_{xx} I_{zz} - {I_{xz}}^2} \sum_{i=1}^{m} B_i(\xi - \bar{z}) - \frac{S_z I_{zz} - S_x I_{xz}}{I_{xx} I_{zz} - {I_{xz}}^2} \sum_{i=1}^{m} B_i(z_i - \bar{x}) \tag{5.11}$$

The shear stress τ_s is calculated by dividing the sum of the shear flows by the local material thickness (t) at the boom position; see equation 5.12.

$$\tau_s = \frac{q_t + q_{s,0} + q_b}{t}; \tag{5.12}$$

Finally, the Von Mises stress σ_{mises} is calculated at each boom position. This is done by combining the bending stress and the shear stress as is done in equation 5.13

$$\sigma_{mises} = \sqrt{{\sigma_b}^2 + 3\tau_s^2}; \tag{5.13}$$

In figures 5.3, 5.5 and 5.7 the results of the stress analysis on the unstiffened panel are displayed, and in figures 5.4, 5.6 and 5.8 the results on the stiffened panel. In these figures the bending, shear and Von Mises stress is indicated in color on the wingbox structure, the maximum calculated Von Mises stress is 288 MPa for an unstiffened skin (possibly sandwich), and 242 MPa for the stiffened skin. These values are below the allowable value for stress of high strength fiber composite of 375 MPa but are higher than the allowed stress of 220 MPa of standard composites, therefore the structure requires the high strength fiber composite; CFRP with T700S fibers.

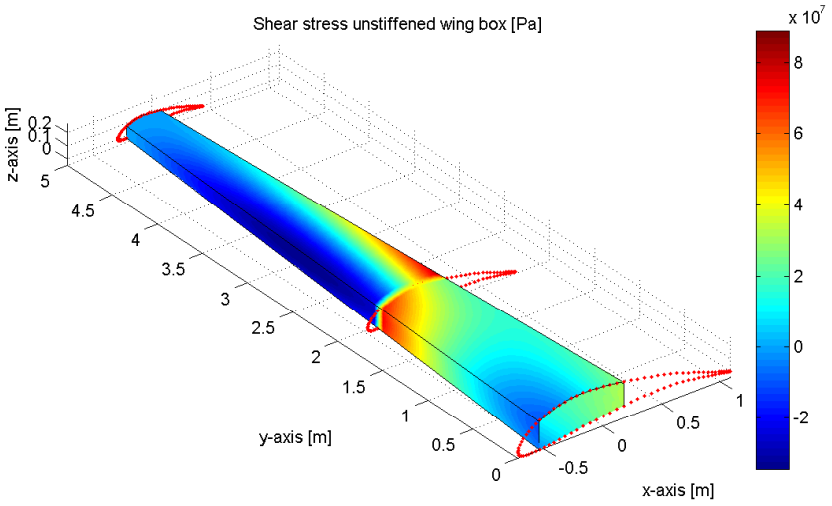

Figure 5.3: 3D surface plot of shear stress on unstiffened wingbox structure

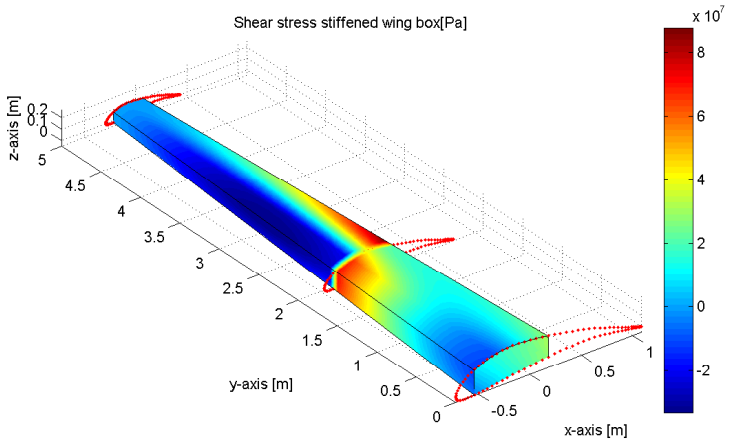

Figure 5.4: 3D surface plot of shear stress on stiffened wingbox structure

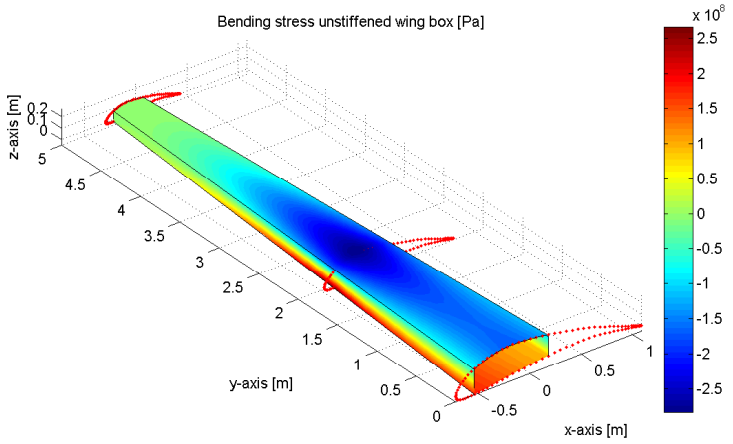

Figure 5.5: 3D surface plot of bending stress on unstiffened wingbox structure

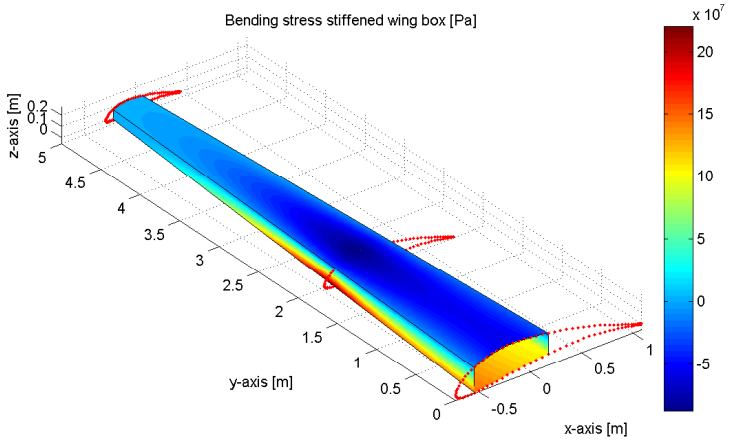

Figure 5.6: 3D surface plot of bending stress on stiffened wingbox structure

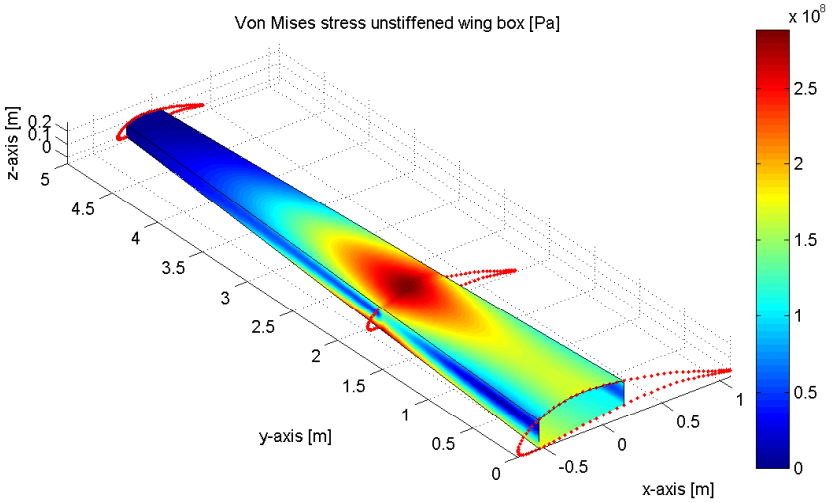

Figure 5.7: 3D surface plot of von Mises stress on unstiffened wingbox structure

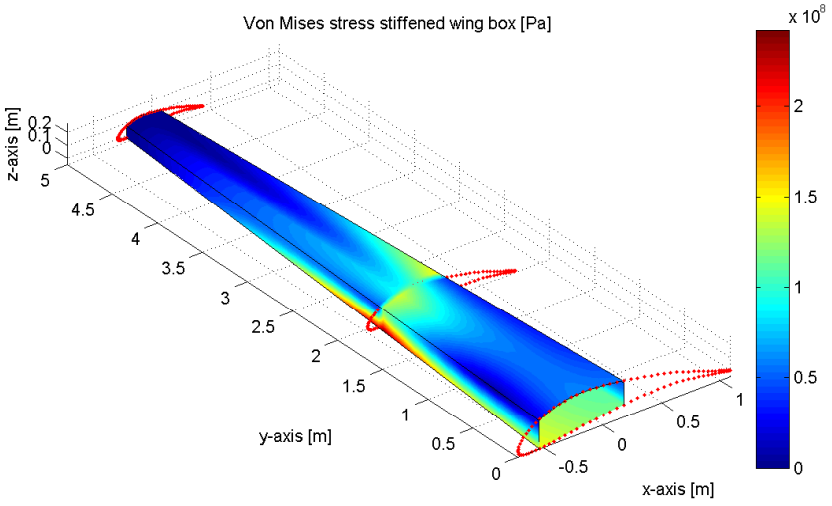

Figure 5.8: 3D surface plot of von Mises stress on stiffened wingbox structure

5.1.4 Buckling analysis

Although the structure is strong enough to withstand the applied stresses, the wing box panels have not been checked for compressive buckling. Failure of the skin panels due to buckling is very likely if these panels do not have additional stiffness, as their thickness is only 0.48 mm.

Two ways of stiffening the skin are considered in multiple configurations; the usage of sandwich panels or the attachment of stiffeners to the skin panel. The construction is discussed in section 3.1. For the calculations in this project the stiffeners are assumed to be L-shaped, in future research hat-stiffeners could also be considered. The reduction of stress in the stiffened panel, is considered in section 5.1.3. The usage of a variable stiffness configuration along the span is not considered, in other words; the amount of stiffeners or the sandwich core thickness is uniform

along the span.

The performed calculations are based on the course "Advanced Design and Optimization of Composite Structures I" by Prof. C. Kassapoglou and on an article found on ESDU for the calculation of buckling of curved, composite plates [15]. Shear buckling of the spar panels is not considered, as the shear stress is relatively low compared to the bending stress, which were both calculated in the stress analysis.

The stiffness of composite plates is summarized in three 3x3 matrices; the A, B and D matrices. The A matrix gives an indication of the extensional stiffness (in-plane loads). The B matrix defines the coupling stiffness, which is zero for symmetric layups. And in the D matrix the bending stiffness is summarized, this is therefore the governing matrix for buckling strength calculations. The matrices have been calculated using the ABD matrix calculator on efunda[3].

To account for the additional bending stiffness for the sandwich plate a correction of the D matrix is included. The sandwich panel correction is found in equation 5.14, where D_{fs} is the sandwich facesheet D matrix, A_{fs} is the facesheet A matrix, t_{r_c} is the core (foam) thickness and t_{fs} is the facesheet thickness.

$$D_{\text{sw}}(i,j) = 2D_{\text{fs}}(i,j) + 2A_{\text{fs}}(i,j)(\frac{t_{\text{r}_\text{c}} + t_{\text{fs}}}{2})^2 \tag{5.14}$$

Not just the type of composite has an effect on the buckling resistance; also the shape of the plate increases its buckling strength. As the wing box top and bottom panel follow the airfoil shape, a buckling strength calculation method which takes this curvature into account is used [15]. For this method the average radius of curvature of the top and bottom panels are considered.

This radius of curvature is calculated according to equation 5.15, using the derivatives of a 5th order polynomial fitted to the airfoil data-points. This polynomial is easily constructed using Matlab's build-in function 'polyfit'.

$$R_{\text{curv}} = \frac{[1 + (\frac{dy}{dx})^2]^{\frac{3}{2}}}{|\frac{d^2y}{dx^2}|} \tag{5.15}$$

It turns out that the effect of shape is so large that with the current shape of the wing box, it would be the lightest option to position the bridles such that only the top panel is in compression. In this way the bottom panel requires no additional stiffness to cope with buckling loads and maximum advantage is taken from the top panel's curvature.

For the calculation of the critical buckling load (N_{crit}) it is important to know what buckling modes will occur. The buckling mode indicates the buckling pattern; it indicates the number

[3]URL: `http://www.efunda.com/formulae/solid_mechanics/composites/comp_intro.cfm` [cited 09 january 2015]

of half-waves in two directions that occur during a buckling deformation. The biggest compressive stresses act in spanwise direction, the buckling modes in this direction are indicated as m. Possible values of m are multiples of 1, because the panel constraints at the ribs are considered hinged. The most probable value of m during loading depends on the rib to rib distance. The number of half-waves perpendicular to the spanwise direction are different for a sandwich panel, which is constraint by the spars, compared to a stiffened panel, of which the considered panel for buckling is constrained by stiffeners. The number of half-waves in this direction is indicated as n. The sandwich panel is considered hinged at the spars at well, which means that n is, just like m, a multiple of 1. However, because the panel aspect ratio (distance between ribs divided by distance between spars) is quite large, only the first buckling mode (1) will be considered, as this one is the most likely to occur. The buckling mode between stiffeners is explained in the course "Advanced Design and Optimization of Composite Structures I" and is set to 5/12, as one side of the panel is considered hinged, and the other free. The constraints for the two panels are displayed in figure 5.9, in which SS stands for Simply Supported.

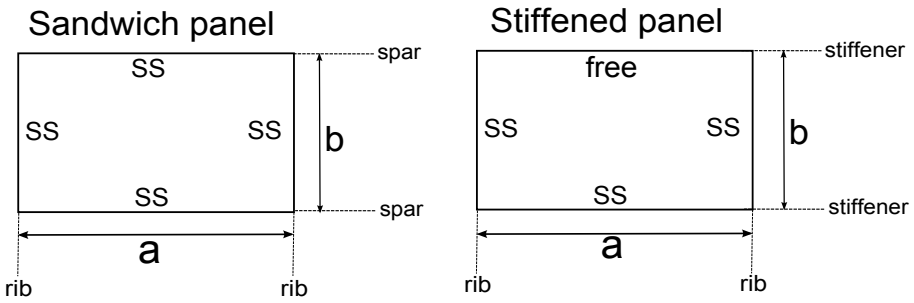

Figure 5.9: Constraints and dimensions of skin panels for buckling

The buckling modes and panel dimensions are used to calculate the factors λ_f and η_f, these factors are calculated according to equations 5.16 and 5.17, where a is the spanwise length of the panel and b width of the panel as indicated in figure 5.9.

$$\lambda_f = \frac{m\pi}{a} \tag{5.16}$$

$$\eta_f = \frac{n\pi}{b} \tag{5.17}$$

The calculation of the critical buckling load (N_{crit}) is done according to equation 5.18, where H_{11}, H_{12}, H_{22} and S are expressed in equations 5.19, 5.20, 5.21 and 5.22 respectively.

$$N_{\text{crit}} = -(\frac{H_{12}^2}{H_{11}} + H_{22})/{\lambda_{\text{f}}}^2 \tag{5.18}$$

$$H_{11} = {\lambda_{\text{f}}}^4 S_{22} + 2(S_{12} + \frac{S_{12}}{2}){\lambda_{\text{f}}}^2 \eta_{\text{f}}^2 + S_{11}\eta_{\text{f}}^4 \tag{5.19}$$

$$H_{12} = \frac{{\lambda_{\text{f}}}^2}{R} \tag{5.20}$$

$$H_{22} = {\lambda_{\text{f}}}^4 D_{11} + 2(D_{12} + 2D_{33}){\lambda_{\text{f}}}^2 \eta_{\text{f}}^2 + D_{22}\eta_{\text{f}}^4 \tag{5.21}$$

$$\boldsymbol{S} = \boldsymbol{A}^{-1} \tag{5.22}$$

$$\tag{5.23}$$

To account for transverse shear effects in the sandwich panel the critical buckling load needs to be reduced according to equation 5.24.

$$N_{\text{crit}_{\text{ts}}} = \frac{t_{\text{r}_\text{c}} G_{\text{c}}}{\frac{t_{\text{r}_\text{c}} G_{\text{c}}}{N_{\text{crit}}} + 1} \tag{5.24}$$

For the stiffened panel the stiffeners have to be checked for buckling as well, equation 5.25 gives an expression for the column buckling load for a stiffener that is hinged on both sides with a length a, Young's modulus E and area moment of inertia I.

$$F_{\text{b}_{\text{crit}}} = \frac{\pi^2 EI}{a^2} \tag{5.25}$$

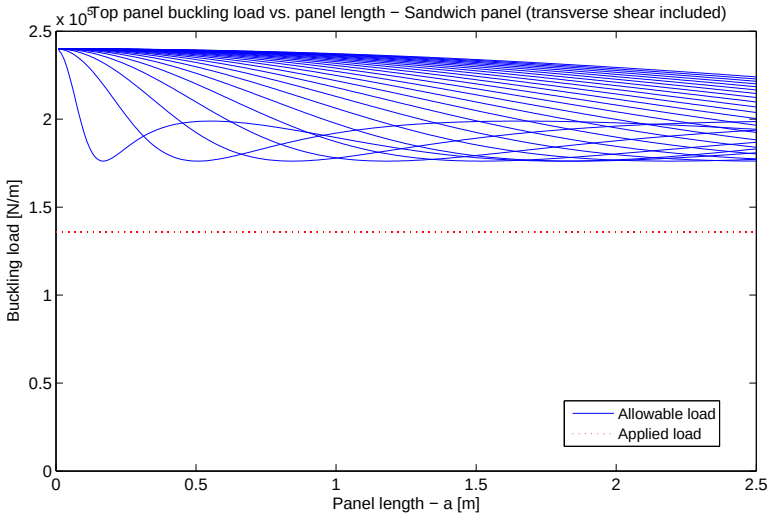

Figure 5.10: Critical buckling load for sandwich panel and applied load as a function of panel length

The results of the buckling analysis are displayed in figures 5.10 and 5.11. For these results a sandwich panel with a core of 10 mm is considered and a stiffened panel with 10 L-shaped stiffeners with cross-sectional dimensions of 20x20x2 mm. The applied load are calculated by

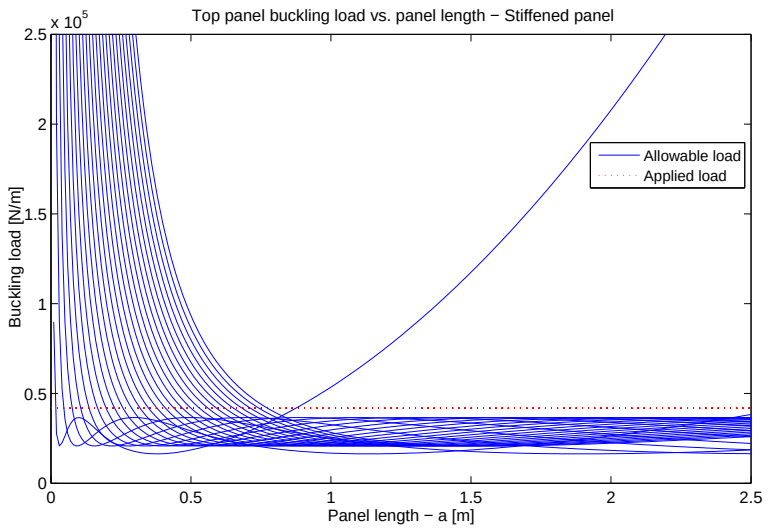

Figure 5.11: Critical buckling load for stiffened panel and applied load as a function of panel length

multiplying the maximum bending stresses obtained from the stress analysis by the skin thickness, in that way obtaining the maximum compressive line load $^{N}/_{m}$. For the applied column buckling load N the maximum compressive stress is multiplied with the cross-sectional area of the stiffener. The required rib spacing for the stiffened panel is calculated to be 0.61 m.

Important to note is that the stiffened panel buckles under the applied load while the sandwich panel is able to withstand the loads. Adding more stiffeners could be an option to improve the buckling capability of the stiffened panel. However, this option was not considered as the wing box weight difference (excluding ribs and attachments) between the sandwich panel reinforced wing box and the stiffened wing box is already 8 kg, and on top of that the stiffened wing box would require more ribs. The total weight of the sandwich panel reinforced wing box is 13.9 kg, while the stiffened wing box has a weight of 22.1 kg. These weights were calculated by using the material properties of section 5.1.2.

5.2 Tail boom

In this section the sizing of the tail boom, that connects the tail to the main wing, will be explained. Two options have been investigated, namely a rectangular and an elliptical cross-section. The rectangular would be beneficial for manufacturing, though the elliptical cross-section results in better aerodynamic properties of the kite. A schematic view on both cross-sections is given in figure 5.12a. An explanation of the dimensions of the elliptical cross-section is also given in section 3.1.2 about the overall design. In figure 5.12b only the schematic view of the elliptical boom is shown, though both cross-sections have same values for height and width. At the main wing the height of the boom is equal to the thickness of the wing airfoil, while at the tail the width of the boom is equal to the the thickness of the vertical tail airfoil. Also along the entire boom the height is twice the weight.

A larger height of the boom would increase its structural capabilities to cope with stresses caused

by the tail. Maximum height results in a tapered boom. For structural calculations the length of the boom is approximated to be $l_{\text{boom}} \approx 4\,\text{m}$, keeping in mind a length of 4.5 m between leading edge of the wing and the aerodynamic center of the tail, as well as that the boom starts at where the wing airfoil is thickest and ends where the vertical tail airfoil is thickest. Also the boom is considered to be straight for calculations, though in fact it has a small deflection of 9 deg upward at the trailing edge of the main wing.

For both options the minimum thickness of the skin has been calculated based on bending stress (5.2.2), maximum shear calculation (5.2.3) and von Mises stress (5.2.4) caused by the positive lift from the tail. With a certain skin thickness, the accompanying weight of the rectangular and elliptical tail boom can be calculated. Taking into account the weight and aerodynamic properties of each option, a choice can be made for the tail boom.

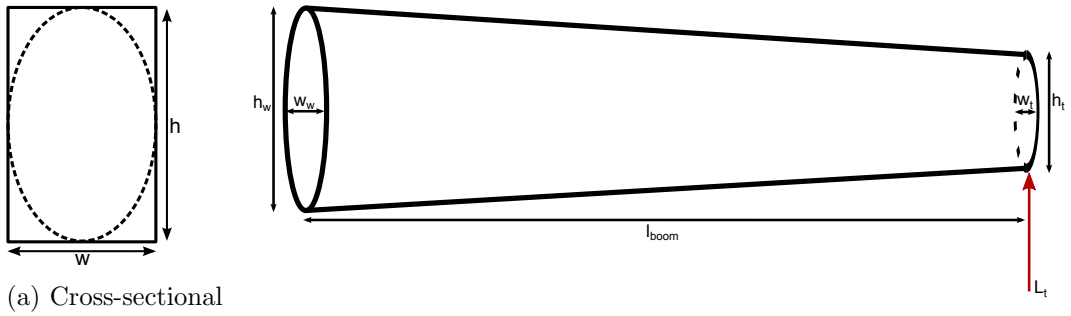

(a) Cross-sectional view

(b) Schematic view of tail boom

Figure 5.12: Dimensions of the tail boom

5.2.1 Mass of the boom

As can be seen in figure 3.2 both booms are tapered. When the required thickness is known, the mass of both tapered booms is calculated. The volume of a tapered boom can be calculated by finding the average area of the cross-section and multiplying this area with the length of the boom. Multiplying the volume with the density of CFRP results in the weight of the boom. The density of CFRP is $\rho_c = 1400\,\text{kg/m}^3$.

5.2.2 Bending stress

To come up with the bending stress first the area moment of inertia has to be calculated. Then the lift force of the tail and the resulting bending moment are calculated. The maximum bending moment will occur at the main wing, as the distance to where the lift force acts is maximum. After this the maximum bending stress can be calculated, comparing this with the ultimate stress of the material the minimum thickness can be found. Afterwards, the weight of both concepts can be calculated for comparison.

Rectangular

First, the area moment of inertia is calculated using equation 5.27. This equation follows from taking the moment of inertia of a solid rectangular cross-section where the width is w_w and the height is h_w, minus the moment of inertia of a solid rectangular cross-section where the

thickness t is subtracted from the width $(w_w - 2t)$ and height $(h_w - 2t)$. Height and width are taken at the main wing, as there the bending moment due to the tail lift force will be highest.

$$I_{yy_{r,solid}} = \frac{1}{12} w h^3 \tag{5.26}$$

$$I_{yy_r} = \frac{1}{12} w_w {h_w}^3 - \frac{1}{12}(w_w - 2t)(h_w - 2t)^3 \tag{5.27}$$

Now the total lift force from the tail L_t is calculated, which will result in a maximum bending moment M_y at the main wing. The density of air is $\rho_a = 1.213$ at $h = 100\,\text{m}$ (figure 4.2) while the maximum apparent kite velocity is $V_a = 40\,\text{m/s}$, following from figure 4.4b where the peak is around $V_a = 40\,\text{m/s}$ at $h = 100\,\text{m}$. This is only during normal reel-out operation, and therefore for a more robust thickness calculation a higher apparent kite velocity is used of $V_a = 50\,\text{m/s}$. The maximum apparent kite velocity results in the highest lift force, and therefore the highest bending moment and stress. Table 5.3 states all values required to calculate the lift force of the tail.

Table 5.3: Tail lift properties

Parameter	Definition	Value
$\rho_a[\text{kg/m}^3]$	Atmospheric density	1.213
$V_a[\text{m/s}]$	Apparent kite velocity	50
$S_t[\text{m}^2]$	Tail surface area	1.523
$C_{L_t}[-]$	Lift coefficient tail	0.6623

$$L_t = \frac{1}{2} \rho_a {V_a}^2 S_t C_{L_t} \tag{5.28}$$

Now the bending moment at the main wing becomes:

$$M_y = L_t l_{boom} \tag{5.29}$$

Bending stress is calculated using the classic bending formula 5.30:

$$\sigma_b = \frac{M_y z}{I_{yy}} \tag{5.30}$$

Bending stress will be maximum at maximum z, which is the maximum distance from the neutral axis at the top and bottom of the boom at the main wing. Therefore $z = \frac{1}{2} h_w$. This results in the maximum bending stress for the rectangular boom of:

$$\sigma_r = \frac{\frac{1}{2} M_y h_w}{I_{yy_r}} \tag{5.31}$$

Using MATLAB for different thicknesses the maximum bending stress can now be calculated. This has been compared with the ultimate stress of carbon $\sigma_u = 250\,\text{MPa}$, resulting in a thickness and a weight where $\sigma_r < \sigma_u$.

Elliptical

For the elliptical boom, the same steps are taken, though only for the moment of inertia the formula for an elliptical shape should be used 5.32. Now using the same bending moment from equation 5.29 and filling in I_{yy_e} from 5.33 into equation 5.30 (for same reason as rectangular, $z = \frac{1}{2}h_w$), the bending stress σ_e is found. This again is compared with the ultimate stress σ_u, to come up with a thickness and a weight.

$$I_{yy_{e,solid}} = \frac{\pi}{4}\frac{w_w}{2}\left(\frac{h_w}{2}\right)^3 \tag{5.32}$$

$$I_{yy_e} = \frac{\pi}{4}\left(\frac{w_w}{2}\left(\frac{h_w}{2}\right)^3 - \left(\frac{w_w}{2} - t\right)\left(\frac{h_w}{2} - t\right)^3\right) \tag{5.33}$$

5.2.3 Shear stress

After the tail boom is analyzed for bending, a shear analysis is carried out to ensure that the structure withstands the shear force generated by the lift of the elevator. Again, both the cross-section (rectangular and elliptical) are analyzed separately and results are compared at the end.

It is assumed that the shear force acts through the shear center. Both the cross-section has at least one axis of symmetry, which leads to I_{zy} equal 0. There is only lift acting in the longitudinal direction (S_z), so S_y is 0. This means only I_{yy} is of interest and this simplifies the shear flow equation to:

$$q_b = -\frac{S_z}{I_{yy}}\int_0^s tzds \tag{5.34}$$

First, the rectangular cross-section will be analysed. A cut is made where the force acts on the cross-section. The shear flow on the cut is zero. The arrangement is shown in the figure 5.13.

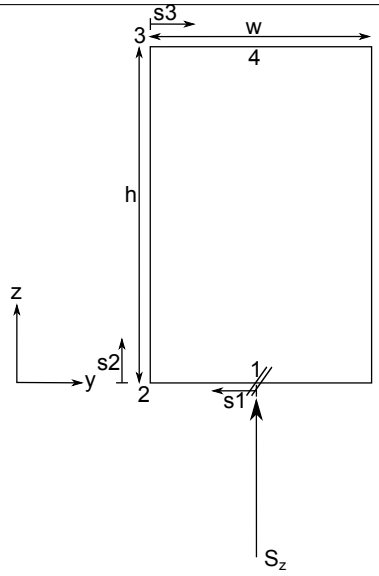

Figure 5.13: Shear flow positions in rectangular cross section

Due to symmetry, only half of the cross-section has to be analyzed for the shear flows. The shear flows across the left half of the cross-section was calculated as follows:

$$q_1 = 0 \tag{5.35}$$

$$q_{1,2} = -\frac{S_z}{I_{yy}} \int_0^{s1} \left(-\frac{h}{2}\right) ds \tag{5.36}$$

$$q_2 = q_{1,2}\left(s = \frac{w}{2}\right) = \frac{S_z t}{4I_{yy}} hw \tag{5.37}$$

$$q_{2,3} = \frac{S_z t}{4I_{yy}} hw - \frac{S_z t}{I_{yy}} \int_0^{s2} \left(s - \frac{h}{2}\right) ds \tag{5.38}$$

$$q_3 = q_{2,3}(s = h) = \frac{S_z t}{4I_{yy}} hw \tag{5.39}$$

$$q_{3,4} = \frac{S_z t}{4I_{yy}} hw - \frac{S_z t}{I_{yy}} \int_0^{s3} \left(\frac{h}{2}\right) ds \tag{5.40}$$

$$q_4 = q_{3,4}\left(s = \frac{w}{2}\right) = \frac{S_z t}{4I_{yy}} hw - \frac{S_z t}{4I_{yy}} hw = 0 \tag{5.41}$$

Shear flow is 0 at position 1 and 4. At position 2 and 3 shear flow is equal and has a value. But it is not sure whether this value is maximum as there might be a value in between position 2 and 3 where there is a maximum shear flow. To check this, the shear flow equation 5.38 is differentiated twice.

$$\frac{\mathrm{d}q_{2,3}}{\mathrm{d}s} = -\frac{S_z t}{I_{yy}}(s - \frac{h}{2}) \tag{5.42}$$

$$\frac{d^2 q_{2,3}}{ds^2} = -\frac{S_z t}{I_{yy}} \tag{5.43}$$

As the 2nd derivative is negative, this implies that there is maximum between position 2 and 3. To get the location of this maximum, the first derivative is set to 0 and the value of s where maximum occurs is found to be at B. The maximum shear flow position is shown in figure 5.14.

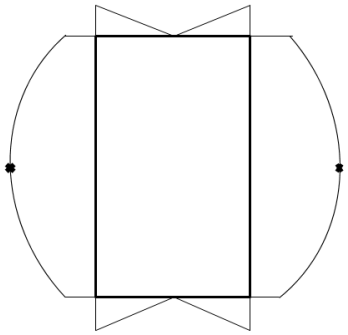

Figure 5.14: Maximum Shear flow positions in rectangular cross section

The maximum shear flow is then divided by skin thickness to get the maximum shear stress. Knowing the maximum shear stress from the material properties, the minimum thickness can be determined numerically.

Now, lets analyze the elliptical cross-section. Boom theory is used in this case to calculate the shear flows.

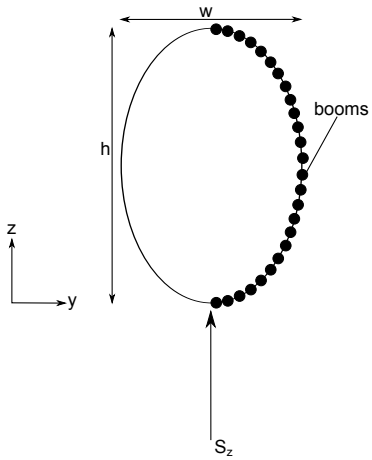

Figure 5.15: Booms position in elliptical cross section

The cross-section is divided in the same manner as in section 5.1.3. The area of each boom is found by dividing the perimeter of the ellipse by the total number of booms and multiplying these with the skin thickness. Once the area of each boom is known, the moment of inertia is calculated by multiplying the boom area with the corresponding distance from the neutral axis.

Finally the shear flows are found with equation 5.44:

$$q_{\mathrm{s}} = -\frac{S_{\mathrm{z}}}{I_{\mathrm{yy}}} \sum_{r=1}^{n} B_{\mathrm{r}} Z_{\mathrm{r}} ds \tag{5.44}$$

The B_r in the equation is the boom area and the Z_r is the distance of the boom from the neutral axis.The maximum shear flow is divided by the thickness to get the maximum shear stress and is compared with the maximum shear stress of the material to get the minimum thickness by iteration.

5.2.4 Von Mises stress

Thirdly, Von Mises stresses σ_{mises} are calculated for both booms by combining bending stress from section 5.2.2 and shear stress from section 5.2.3, using equation 5.13. Values for Von Mises stress are compared with the ultimate stress of $\sigma_{\mathrm{u}} = 350\,\mathrm{MPa}$, to find a thickness where $\sigma_{\mathrm{mises}} < \sigma_{\mathrm{u}}$.

5.2.5 Results

The resulting thicknesses and weights are presented in table 5.4. The Von Mises stress is critical compared to shear and bending stresses, which will give higher required thicknesses for both rectangular and the elliptical boom. A safety factor of two (SF2) is included to cope with unexpected loads, uncertainties and classification, therefore the minimum required thickness is doubled. This leads to a thickness of 0.8 mm for the rectangular boom (t_r) and 1.4 mm for the elliptical boom(t_e). Though the thickness is almost twice as high for the elliptical boom, the weight of the elliptical boom is only approximately 1 kg higher. This difference in weight is negligible, keeping in mind a total system weight of approximately 40 kg while the elliptical beam will only weigh(W_e) approximately 3.5 kg (rectangular beam weighs (W_r) approximately 2.5 kg). On the other hand, the aerodynamic properties of an elliptical shape are much better than a rectangular one, which leads to the choice for using an elliptical tail boom. Also the boom is blended with the main wing, reducing the final weight of the tail boom. The connection method between the tail boom and the main wing, as well as the connection between the tail boom and the vertical tail, will be bolted joints. As both connections are highly critical, a durable and reliable method should be used. Therefore common bolts are preferred over adhesive bonding methods. Further investigation has to be done to determine induced stresses using this jointing method.

Table 5.4: Resulting thicknesses and weights

	Bending	Shear	Von Mises	SF2
t_r (mm)	0.388	0.0340	0.389	0.8
W_r (kg)	1.298	0.114	1.301	2.668
t_e (mm)	0.661	0.270	0.687	1.4
W_e (kg)	1.733	0.710	1.801	3.652

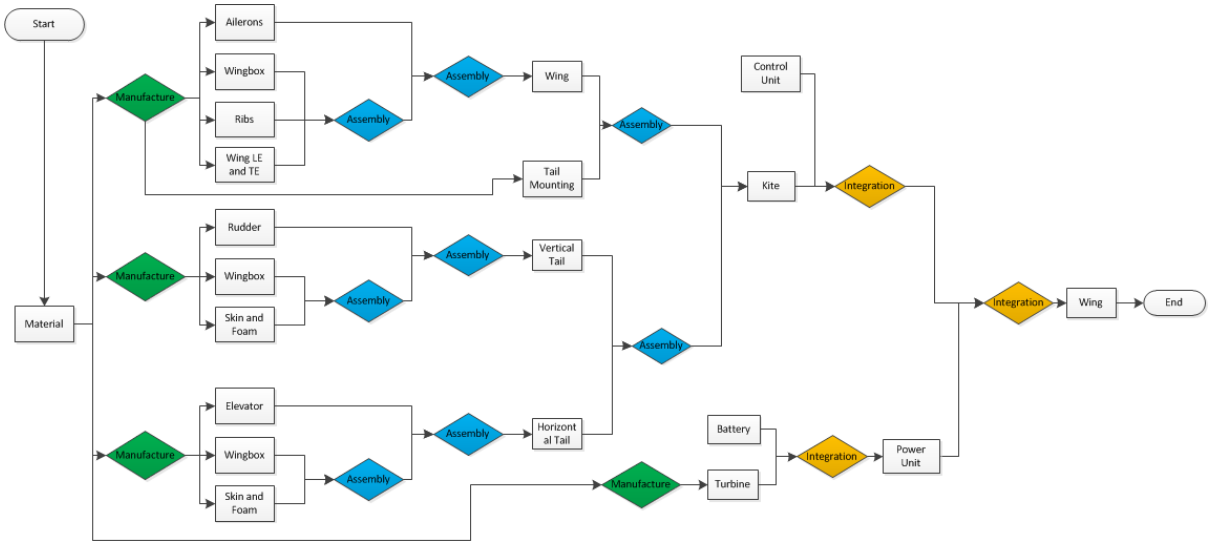

Figure 5.16: Manufacturing, Assembly and Integration outline

5.3 Manufacturing, assembly and integration

The Manufacturing, Assembly, Integration (MAI) plan consist of a time-ordered outline of the activities required to construct the total kite system from its constituents. In figure 5.16 it is shown that the production process starts with the manufacturing of the different elements, like the wingbox parts, ribs and control surfaces. During this stage, most of the structural components are formed in moulds. After the elements are completed they are put together during the assembly process, for example the control surfaces, wingbox parts and the leading edge are combined to form the wing component. In order to prevent time delay in the process the tail elements are manufactured and assembled simultaneously. At the end of the process the additional components like the power supply, transceiver and the control unit are integrated in the kite.

Chapter 6

Stability

Stability is defined as the ability to maintain a uniform flight condition and return to that condition after being disturbed. The preferred condition is when the kite is in equilibrium, when all forces are in balance. The initial tendency to return to the equilibrium when disturbed from that state is called (positive) static stability. When a kite demonstrates an increase in its displacement from the equilibrium state, it has a negative stability. When no extra displacement occurs, the kite is neutral stable. Dynamic stability is about the motion and time required for a response to disturbances. So dynamic stability refers to the way the kite oscillates when responding to disturbances. Positive dynamic stability means that the oscillations increase over time and negative dynamic stability is when the oscillations die out over time. When the oscillations remain constant, there is neutral dynamic stability.

For the kite concepts, positive stability is necessary, so that less control input is needed to bring the kite back in equilibrium. To achieve that, it is necessary to make sure that the kite can be in force equilibrium. This can be achieved by changing the elevator deflection angle of the horizontal tail. To make sure the kite is statically stable, manipulating the location of the center of gravity and sizing the tail volume is required. For dynamic stability, some of the eigenvalues will be calculated to determine what kind of stability is present. In this chapter, inputs from the structures and aerodynamic part are used for calculations with respect to equilibrium and stability. This will result in a location of the center of gravity and a tail sizing. This data can be passed back to the structural and aerodynamic sizing of the kite.

6.1 Assumptions

Before any calculations can be made, a number of assumptions have to be made. This is to reduce the complexity of the calculations. For these assumptions, the different situations are taken into account. The first one is during the traction phase. Here, the forces acting on the kite are at a maximum value, while operating at the maximum altitude. The second one is during the reel in phase, where the kite is descending as a glider plane. Here, lift forces are at a minimum. All these assumptions are listed and briefly explained in this section. Argumentation why these can be made and what their effects are, will also be discussed in this section.

Linearization
It is assumed that only small changes in angle of attack are present during calculations. Therefore, linearization can be assumed when calculating the lift coefficient from the lift slope.

Mass-less kite
The kite weight is estimated to be in a range from 30-50 kg. This weight, compared to a lift load of 20 kN, achieved during the traction phase, is therefore negligible. The assumption is made that the mass of the kite is zero. This will result in that the kite has no real center of gravity caused by its own weight. Note that this assumption is only valid during the traction phase and not during the reel in phase.
Small Earth
In contrast with conventional aircraft, where a flat Earth is assumed, a small Earth assumption is made. This means that the Earth can be seen as a point mass and therefore as a ground station. The tether force can then be compared to the gravitational force, always pointing to the ground station. Together with the mass-less kite assumption, the placement of the tether to the kite, can be seen as its center of gravity. Again, this assumption is only valid during the traction phase.
Fixed tether location
It is assumed that the tether is fixed to the kite and does not move during operation. This will result that during traction mode, combined with previous assumptions, that the center of gravity does not move during operation.
Constant flight angle
It is assumed, that during its flight, the angle with respect to the airspeed, is constant. So the kite will always fly parallel to the airspeed. Because of the assumption that the kite is mass less, there will be no slide slip due the gravity in the cross wind phase. This will eventually result in a constant equilibrium when flying in the crosswind, comparing it to the conventional situation.
Symmetry
The kite is assumed to be symmetrical around its x-axis. This will mean that forces on the left and right of the kite are equal to each other.

6.2 Force equilibrium

Using the previous assumptions, the stat7e where all the forces are in equilibrium can be found. Due the fact that the kite is symmetric with respect to the xz-plane, only the equilibrium in z_k and x_k has to be determined. This is done by first drawing the free body diagram. When the diagram is known, the moment equilibrium will be stated. To achieve this equilibrium, an elevator deflection can be required. The equation to calculate the required deflection of the elevator in the tail will therefore also be presented. Required for calculating this elevator deflection, the tail volume and center of gravity location of the static stability section are used.

To calculate the equilibrium, three positions of the kite are assumed. The first one is horizontal, which occurs during the traction phase and the gliding phase. Here, the kite has only small changes in angle of attack. For the traction phase, the weight is neglected and for the gliding phase, the tether force in assumed to be zero. The third situation is the diving phase. Here, the kite is at a negative angle of attack. Both tether force and the weight have great influence during the diving phase.

6.2.1 Horizontal state

First, the free body diagram (FDB) is stated for the horizontal state. For now, only the traction phase is taken into consideration. The gliding phase is comparable, only instead of a tether

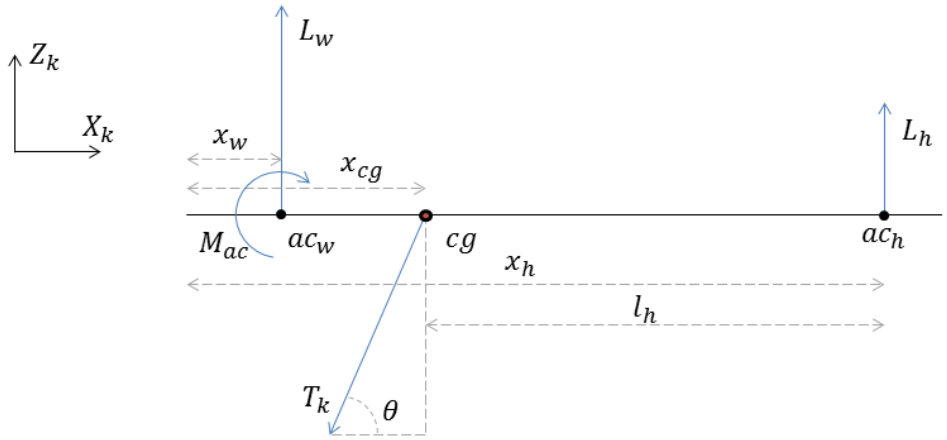

Figure 6.1: Free body diagram of the kite

force, there is a weight of the kite.

Due to the assumption of a constant flight angle, the free body diagram can be drawn as in figure 6.1.

The symbols are explained in table 6.1.

Table 6.1: Symbols for figure 6.1

Parameter	Defintion
L_w	Lift force due the wing
L_h	Lift force due horizontal tail
T_k	Tether force at the kite
θ	Elevation angle
M_ac	Moment in the aerodynamic center

From this FBD, the force equilibrium in z_k direction can be made:

$$\sum F_\mathrm{z} = L_\mathrm{w} + L_\mathrm{h} - T_\mathrm{k}\cos(\theta) = 0 \tag{6.1}$$

Here, the lift forces are equal to:

$$L_\mathrm{w} = \frac{1}{2}\rho {V_\mathrm{w}}^2 S_\mathrm{w} C_{\mathrm{L_w}} \tag{6.2}$$

$$L_\mathrm{h} = \frac{1}{2}\rho {V_\mathrm{h}}^2 S_\mathrm{h} C_{\mathrm{L_h}} \tag{6.3}$$

The air velocity of the wing and tail are represented as V_w and V_h, S_w and S_h are the surfaces of the wing and tail, $C_{\mathrm{L_w}}$ and $C_{\mathrm{L_h}}$, the lift coefficients and the atmospheric density is noted as ρ.

From the force equilibrium follows that the tether force at the kite is:

$$T_{\mathrm{k}} = \frac{L_{\mathrm{w}} + L_{\mathrm{h}}}{\cos(\theta)} \tag{6.4}$$

For the moment equilibrium around the y-axis, all the forces acting in x and z direction are taken into account. Due to the assumption that the tether attachment location can be seen as the center of gravity, the tether force on the kite has no contribution on the overall moment. How the moment about the center of gravity is calculated can be found in equation 6.5.

$$\sum M_{\mathrm{y}} = M_{\mathrm{ac}} + L_{\mathrm{w}}(x_{\mathrm{cg}} - x_{\mathrm{ac}}) - L_{\mathrm{h}}(x_{\mathrm{h}} - x_{\mathrm{cg}}) \tag{6.5}$$

Here, M_{ac} is the moment in the aerodynamic center of the wing. The distances can be found in figure 6.1.

Equation 6.5 divided by $\frac{1}{2}\rho {V_{\mathrm{w}}}^2 S_{\mathrm{w}} \bar{c}$, results in the dimensionless equation for the moment equilibrium:

$$C_{\mathrm{M}} = C_{\mathrm{M_{ac}}} + C_{\mathrm{L_w}} \frac{(x_{\mathrm{cg}} - x_{\mathrm{ac}})}{\bar{c}} - C_{\mathrm{L_h}} \frac{(x_{\mathrm{h}} - x_{\mathrm{cg}})}{\bar{c}} \frac{S_{\mathrm{h}}}{S_{\mathrm{w}}} \left(\frac{V_{\mathrm{h}}}{V_{\mathrm{w}}}\right)^2 \tag{6.6}$$

Defining the tail length as:

$$L_{\mathrm{h}} = x_{\mathrm{h}} - x_w \approx x_{\mathrm{h}} - x_{\mathrm{ac}} \tag{6.7}$$

And the tailplane volume as:

$$\frac{(x_{\mathrm{h}} - x_{\mathrm{ac}})}{\bar{c}} \frac{S_{\mathrm{h}}}{S_{\mathrm{w}}} = \frac{S_{\mathrm{h}} L_{\mathrm{h}}}{S_{\mathrm{w}} \bar{c}} \tag{6.8}$$

Implementing these definitions in equation 6.6 results in equation 6.9:

$$C_{\mathrm{M}} = C_{\mathrm{M_{ac}}} + C_{\mathrm{L_w}} \frac{(x_{\mathrm{cg}} - x_{\mathrm{ac}})}{\bar{c}} - C_{\mathrm{L_h}} \frac{S_{\mathrm{h}} L_{\mathrm{h}}}{S_{\mathrm{w}} \bar{c}} \left(\frac{V_{\mathrm{h}}}{V_{\mathrm{w}}}\right)^2 \tag{6.9}$$

When $C_{\mathrm{M}} = 0$, the kite is in equilibrium.

6.2.2 Required elevator deflection in horizontal state

To ensure that the moment coefficient is zero, and therefore that the kite is in equilibrium, multiple sizing can be done. Tail sizing, which consists of the tail surface and location, and the lift coefficient of the tail, which can be manipulated using the elevator. The latter is now elaborated on.

Using linearization, the lift coefficients of the wing and tail can be rewritten:

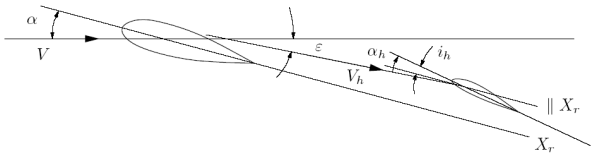

Figure 6.2: Present angles on tail

$$C_{\mathrm{L_w}} = \frac{dC_w}{d\alpha}(\alpha - \alpha_0) = C_{\mathrm{L_{w,\alpha}}}(\alpha - \alpha_0) \tag{6.10}$$

(6.11)

$$C_{\mathrm{L_h}} = \frac{dC_h}{d\alpha}(\alpha - \alpha_0) = C_{\mathrm{L_{h,\alpha}}}\alpha + C_{\mathrm{L_{h,\delta e}}}\delta \tag{6.12}$$

For the angle of attack of the tail, equation 6.13 is determined from figure 6.2

$$\alpha_h = \alpha - \epsilon + i_{\mathrm{h}} \tag{6.13}$$

Here, α is the angle of attack of the wing, ϵ is the downwash angle and i_{h} is defined as the difference between the angle of the main wing and the tail. The downwash angle can be approximated with equation 6.14.

$$\epsilon = (\alpha - \alpha_0)\frac{d\epsilon}{d\alpha} \tag{6.14}$$

Substitution of equation 6.14 into 6.13 yields:

$$\alpha_{\mathrm{h}} = (\alpha - \alpha_0)\left(1 - \frac{d\epsilon}{d\alpha}\right) + (\alpha_0 + i_{\mathrm{h}}) \tag{6.15}$$

Note that α_0 is the angle of attack where zero lift is generated.

Now the moment equation can also be rewritten as follows:

$$C_{\mathrm{m}} = C_m r m_0 + C_{\mathrm{m_\alpha}}(\alpha - \alpha_0) + C_{\mathrm{m_{\delta E}}} \tag{6.16}$$

With:

$$C_m rm_0 = C_{\mathrm{Mac}} - C_{\mathrm{L_{h,\alpha}}}(\alpha_0 + i_{\mathrm{h}})\alpha_{\mathrm{h}} \frac{S_{\mathrm{h}} L_{\mathrm{h}}}{S_{\mathrm{w}} \bar{c}} \left(\frac{V_{\mathrm{h}}}{V_{\mathrm{w}}}\right)^2 \tag{6.17}$$

$$C_{\mathrm{m_\alpha}} = C_{\mathrm{L_{w,\alpha}}} \frac{(x_{\mathrm{cg}} - x_{\mathrm{ac}})}{\bar{c}} - C_{\mathrm{L_{h,\alpha}}} \left(1 - \frac{d\epsilon}{d\alpha}\right) \frac{S_{\mathrm{h}} L_{\mathrm{h}}}{S_{\mathrm{w}} \bar{c}} \left(\frac{V_{\mathrm{h}}}{V_{\mathrm{w}}}\right)^2 \tag{6.18}$$

$$C_{\mathrm{m_{\delta E}}} = -C_{\mathrm{L_{h,\delta}}} \frac{S_{\mathrm{h}} L_{\mathrm{h}}}{S_{\mathrm{w}} \bar{c}} \left(\frac{V_{\mathrm{h}}}{V_{\mathrm{w}}}\right)^2 \tag{6.19}$$

$$\tag{6.20}$$

Rearranging these equations, the equation for the required elevator deflection can be determined.

$$\delta_e = -\frac{1}{C_{\mathrm{m_{\delta E}}}} \left[C_m rm_0 + C_{\mathrm{m_\alpha}}(\alpha - \alpha_0)\right] \tag{6.21}$$

As can be seen in equation 6.17, the tail volume is needed to determine the elevator angle. In section 6.3, the tail sizing is done and the tail volume is calculated. Most of the other input values can be determined from the aerodynamic calculations in chapter 4. All are depending on the chosen airfoils and the sizing of the wing (and tail). Only $C_{\mathrm{L_{h,\delta}}}$ depends on the elevator. In this phase of the design, this value can not yet be calculated. It is possible to estimate it with data provided from [1], see figure 6.3.

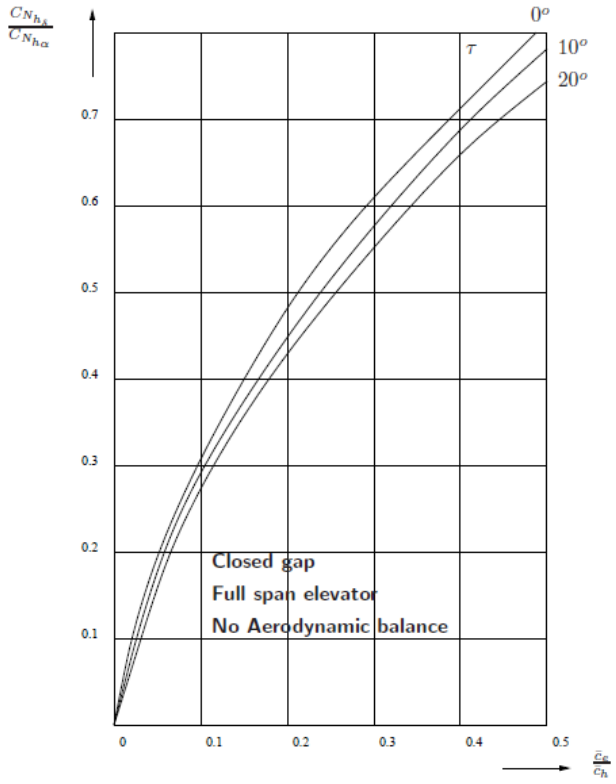

Figure 6.3: Elevator curve [1]

With the chord ratio known, determined from the tail volume, and with a trailing edge angle τ of zero degrees, the $C_{L_{h,\delta}}$ can be estimated. The values used and the corresponding results are presented in tables 6.2 and 6.3.

Table 6.2: Input variables during horizontal flight

Parameter	Traction	Glide
C_{L_w} [−]	2.08	0.1557
S_w [m^2]	12.695	12.695
V/Vh [−]	1	1
$\bar{c}$ [m]	1.347	1.347
x_{ac} [m]	0.34 c	0.34 c
$C_{L_{w,\alpha}}$ [rad^{-1}]	4.68	4.68
$C_{M_{ac}}$ [-]	-0.1992	-0.1992
b_w [m]	10	10
α [deg]	18	0
i_h [deg]	3.5	3.5
α_0 [deg]	-7.5	-7.5
A_h [-]	4	4
$C_{L_{\alpha_h}}$ [rad^{-1}]	3.76	3.76
S_h [m^2]	0.15 S_w	0.15 S_w
x_h [m]	4.5	4.5

Table 6.3: Results for horizontal flight

Parameter	Traction	Glide
$c/\bar{c}$ [-]	0.4643	0.4643
$C_{L_{\delta_h}}$ [-]	2.7824	2.7824
δ [deg]	-4.9791	-11.3707

6.2.3 Non-horizontal state

During the reel-in phase, the kite is no longer in a horizontal state, but it dives down. For this state, the free body diagram is drawn in figure 6.4. The symbols are explained in table 6.4

From this FBD, the force equilibrium in x and z direction can be stated and should be zero. In x direction equation 6.22 is used and equation 6.23 is used for the z direction. Note that the Earth reference system is used here.

$$\sum F_x = sin(\phi)L_w + sin(\phi L_h + cos(\phi)D_w + cos(\phi)D_h - sin(\theta)F_{reel} = 0 \tag{6.22}$$

$$\sum F_z = cos(\phi)L_w + cos(\phi)L_h - sin(\phi)D_w - sin(\phi)D_h - W - cos(\theta)F_{reel} = 0 \tag{6.23}$$

To satisfy equilibrium, the moment coefficient C_M should also be zero during the diving phase. This coefficient is calculated using equation 6.24.

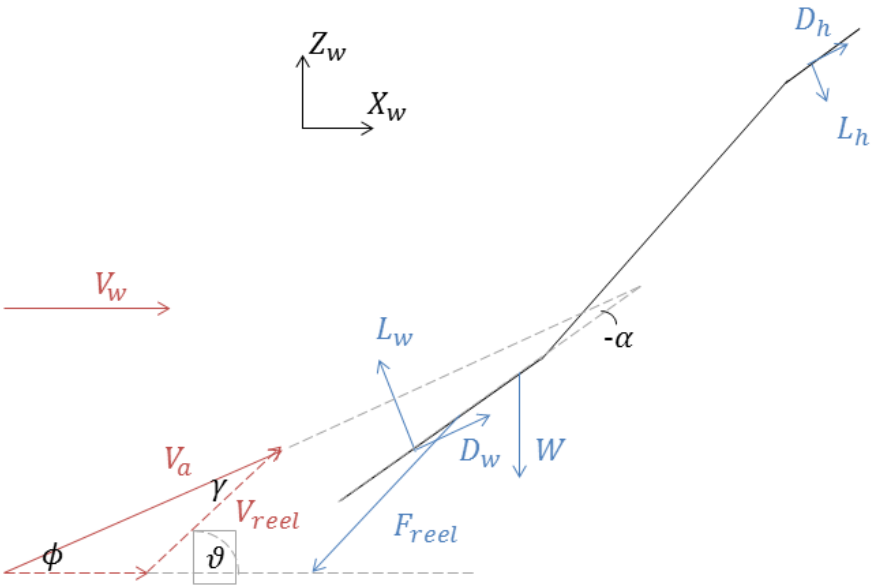

Figure 6.4: Free body diagram dive flight

$$C_{\mathrm{M}} = C_{\mathrm{M_{ac}}} + C_{\mathrm{L_w}} cos(\alpha) \left(\frac{x_{\mathrm{ta}} - x_{\mathrm{ac}}}{\bar{c}} \right) - C_{\mathrm{W}} cos(\alpha) \left(\frac{x_{\mathrm{ta}} - x_{\mathrm{ac}}}{\bar{c}} \right) - C_{\mathrm{L_h}} cos(\alpha) \frac{S_{\mathrm{h}} L_{\mathrm{h}}}{S_{\mathrm{w}} \bar{c}} \left(\frac{V_{\mathrm{h}}}{V_{\mathrm{w}}} \right)^2 + C_{\mathrm{D_h}} sin(\alpha) \frac{S_{\mathrm{h}} L_{\mathrm{h}}}{S_{\mathrm{w}} \bar{c}} \left(\frac{V_{\mathrm{h}}}{V_{\mathrm{w}}} \right)^2 \quad (6.24)$$

Here, $C_{\mathrm{L_w}}$, $C_{\mathrm{L_h}}$, $C_{\mathrm{D_w}}$ and $C_{\mathrm{D_h}}$ are a function of the angle of attack α. The angles γ and ϕ are a function of the reel-in speed V_{r}. Both parameters can be optimized to make sure that C_{M} is zero and therefore is in equilibrium.

6.2.4 Required elevator deflection in non-horizontal state

During the diving phase, the tail encounters a negative angle of attack. Due to the fact that the tail has a symmetric profile, this negative α creates a negative lift. To establish a zero moment coefficient at this negative pitch angle, a positive lift force from the tail is required. To create this, an elevator deflection is required, see equation 6.12.

With the reel in speed and angle of attack determined in chapter 9, the required deflection angle can be calculated. The values used and the deflection angle can be found in table 6.5.

6.3 Static stability

With the equilibrium of the kite known, the ability to return to that state after a disturbance can be looked into. The static stability in longitudinal and lateral direction are discussed in this

Table 6.4: Symbol explanation for figure 6.4

Parameter	Definition
D_{w}	Drag due the wing
D_{h}	Drag due the horizontal tail
F_{reel}	Reel in force
V_{a}	Apparent air speed
V_{w}	Wind speed
V_{r}	Reel in speed
α	Angle of attack (negative)
γ	Angle between V_a and V_{r}
θ	Angle of the tether
ϕ	Angle between V_{w} and V_a

Table 6.5: Values and results dive motion

Parameter	Value
α [deg]	-7.0
$C_{\mathrm{L_w}}$ [-]	0.0892
V_{r} $[m/s]$	45
ϕ [deg]	25.5952
δ [deg]	5.6763

section. First, the related free body diagrams are drawn. With the acting forces determined, the conditions for stability are stated.

6.3.1 Longitudinal

First, the stability in longitudinal direction is discussed. Here, the pitch moment stability is of great importance. When a sudden change in angle of attack occurs, the kite can react with a counter moment to return to its original state. When this happens, the kite has (positive) pitch stability. A positive stability is necessary, because the original state of the kite is optimal with respect to power generation. It is also preferred to be stable when the kite is descending, so it can glide downwards and needs less pulling force from the ground station. Therefore, the longitudinal static stability for both situations is determined. The kite achieves this when the pitching moment coefficient derivative with respect to α is negative, see equation 6.25.

$$\frac{dC_{\mathrm{M}}}{d\alpha} < 0 \tag{6.25}$$

To calculate this pitch moment with respect to the angle of attack C_{m_α}, the same FBD of the force equilibrium is used as given in section 6.2. From this equilibrium, the moment coefficient is stated as:

$$C_{\mathrm{M}} = C_{\mathrm{M_{ac}}} + C_{\mathrm{L_w}} \frac{(x_{\mathrm{cg}} - x_{\mathrm{ac}})}{\bar{c}} - C_{\mathrm{L_h}} \frac{S_{\mathrm{h}} L_{\mathrm{h}}}{S_{\mathrm{w}} \bar{c}} \left(\frac{V_{\mathrm{h}}}{V_{\mathrm{w}}} \right)^2 \tag{6.26}$$

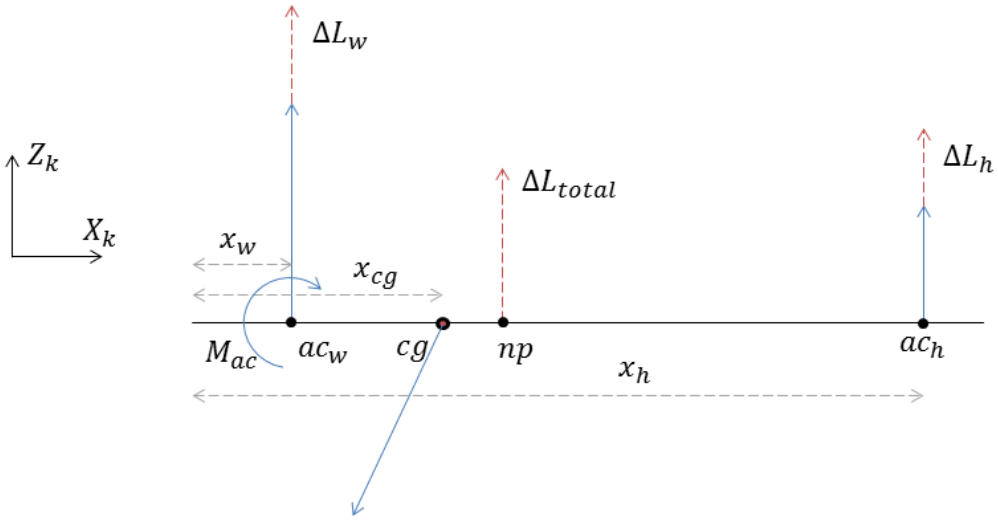

Figure 6.5: Change of lift for positive pitch movement

In section 6.2, the moment derivative with respect to angle of attack was stated as well, being:

$$C_{\mathrm{m}_\alpha} = C_{\mathrm{L_{w,\alpha}}} \frac{(x_{\mathrm{cg}} - x_{\mathrm{ac}})}{\bar{c}} - C_{\mathrm{L_{h,\alpha}}} \left(1 - \frac{d\epsilon}{d\alpha}\right) \frac{S_{\mathrm{h}} L_{\mathrm{h}}}{S_{\mathrm{w}} \bar{c}} \left(\frac{V_{\mathrm{h}}}{V_{\mathrm{w}}}\right)^2 < 0 \tag{6.27}$$

It is possible to rewrite this equation to determine the range of center of gravity location, where the kite is still pitch stable:

$$\frac{(x_{\mathrm{cg}} - x_{\mathrm{ac}})}{\bar{c}} < \frac{C_{\mathrm{L_{h,\alpha}}}}{C_{\mathrm{L_{w,\alpha}}}} \left(1 - \frac{d\epsilon}{d\alpha}\right) \frac{S_{\mathrm{h}} L_{\mathrm{h}}}{S_{\mathrm{w}} \bar{c}} \left(\frac{V_{\mathrm{h}}}{V_{\mathrm{w}}}\right)^2 \tag{6.28}$$

Here it is shown that both the location of the tether attachment to the kite (cg) and the tail volume $\left(\frac{S_{\mathrm{h}} L_{\mathrm{h}}}{S_{\mathrm{w}} \bar{c}}\right)$ determine if the kite has pitch stability. The location of x_{cg}, where the moment derivative is zero, is called the neutral point. When the x_{cg} lies on this point, the kite is neutrally stable. This x_{np} (neutral point) is also the point where the resulting change in lift force acts on, when a change in angle of attack occurs. See figure 6.5 for a graphical description.

To conclude, as can be seen from equation 6.5, positive stability in longitudinal direction is achieved when the center of gravity lies in front of this neutral point and behind the aerodynamic center of the wing.

As stated earlier, three phases are calculated for the tail volume and also for the required elevator deflection. For the phase in traction mode, the values that are used can be found in table 6.6.

Using these values and equations 6.26-6.28, a stability plot has been made. In this plot, the ratio $\frac{S_{\mathrm{h}}}{S_{\mathrm{w}}}$ is plotted against the center of gravity. If the x_{cg} is left of the curve for a certain ratio, the kite is stable. Besides the analytical method, a numerical method is also used to calculate the curve. Here, the lift coefficients are not determined with the DATCOM method,

Table 6.6: Input variables for static stability

Parameter	Value
C_{L_w} [-]	2.08
S_w [m^2]	12.695
V_w [m/s]	40
$x_{ac}/\bar{c}$ [m]	0.34
$C_{L_{\alpha_w}}$ [rad^{-1}]	4.68
$C_{M_{ac,w}}$ [-]	-0.2145
b_w [m]	10
V_h [ms]	40
A_h [-]	4
γ [deg]	1.41
R [J/kgK]	287.05
T [K]	285.689
ρ [kg/m^3]	1.1137

but calculated using an XFLR5 model. The results are shown in table 6.7. This difference in values results in a negligible difference in the stability curve of the kite, as can be seen in figure 6.6.

Table 6.7: Lift slope from DATCOM and XFLR5

Parameter	DATCOM	XLFR5
$C_{L_{h,\alpha}}$ [-]	3.7811	3.7201

From this graph, a tether attachment point and a horizontal tail surface are determined for during traction phase. To reduce the torsion force in the main wing, it is preferred to have the center of gravity behind the center of pressure. From the aerodynamics chapter 4, it is known that the center of pressure is estimated to be around half chord. Therefore, the *cg* should be between the 0.5 c and the stability curve. The results for the surface ratio, the center of gravity and the tail volume are presented in table 6.8.

Table 6.8: Results for longitudinal stability

Parameter	Value
x_{cg} [-]	0.55 c
S_h/S_w [-]	0.15
Tail volume [-]	0.4360

6.3.2 Lateral

Besides stability in longitudinal direction, it is also possible to achieve stability in lateral direction. Roll and yaw movement occur on the kite and require a counter moment that will result in less required control input. Therefore, the roll and yaw stability are looked into in this section. First, the free body diagrams are determined, with all the relevant forces and moments stated. Then the configuration is reasoned to achieve stability if there is a counter moment present. If this is the case for a motion, it is positively stable.

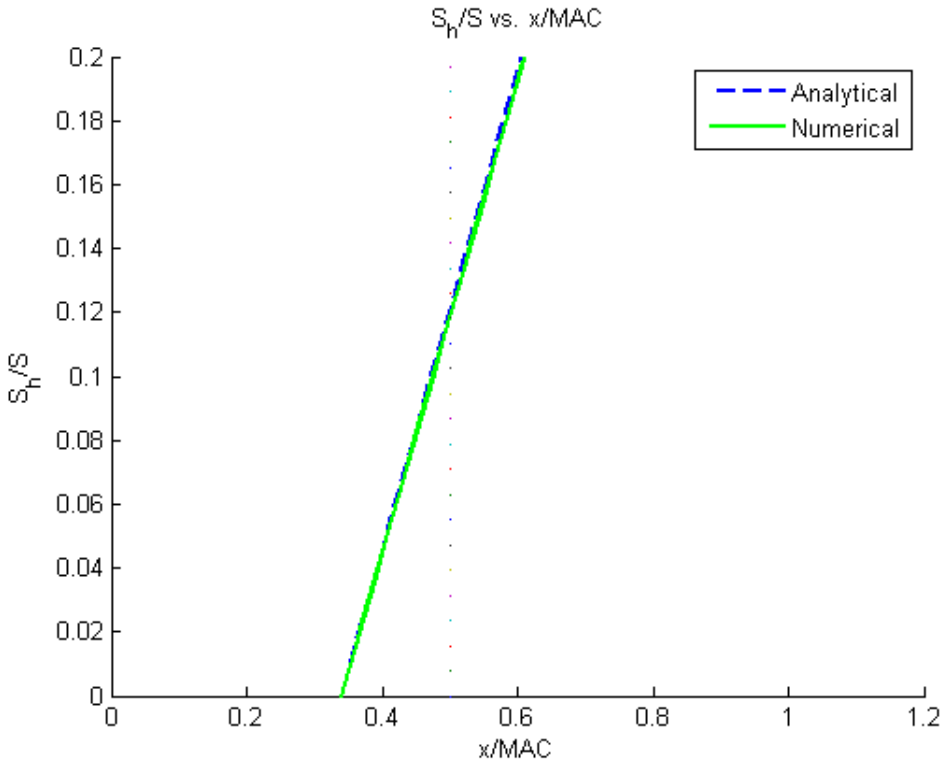

Figure 6.6: Stability curve

For roll motion, the FBD can be seen in figure 6.7. Here, a positive roll rate p is assumed. Other parameters are summarized in table 6.9.

Table 6.9: Symbol explanation for figure 6.7

Parameter	Definition
$L_{\mathrm{w,l}}$	Lift force due left wing
$L_{\mathrm{w,r}}$	Lift force due right wing
$T_{\mathrm{k,l}}$	Tension force in left tether
$T_{\mathrm{k,r}}$	Tension force in right tether
$L_{\mathrm{h,l}}$	Lift force due left horizontal tail
$L_{\mathrm{h,r}}$	Lift force due right horizontal tail
L_{v}	Lift force due vertical tail
Γ	Dihedral angle

When in roll motion, one wing moves down and the other one moves up. In this situation, the left wing moves upwards and the right wing downwards. The lower, right wing will have an increased angle of attack and therefore will have a larger lift force compared to the higher, left wing. So, the resulting difference in lift force will create a moment in the opposite direction of the roll movement. For the horizontal tail happens the same: the right wing will produce more lift then the left, so it will create a counter moment to the roll movement. The vertical tail also has an increase in angle of attack due the roll motion and will create a lift force. This force creates a moment in the opposite direction of the movement. As assumed in chapter 5, the forces on both tethers are equal. These forces therefore cancel out each other and do not create a moment around the x-axis.

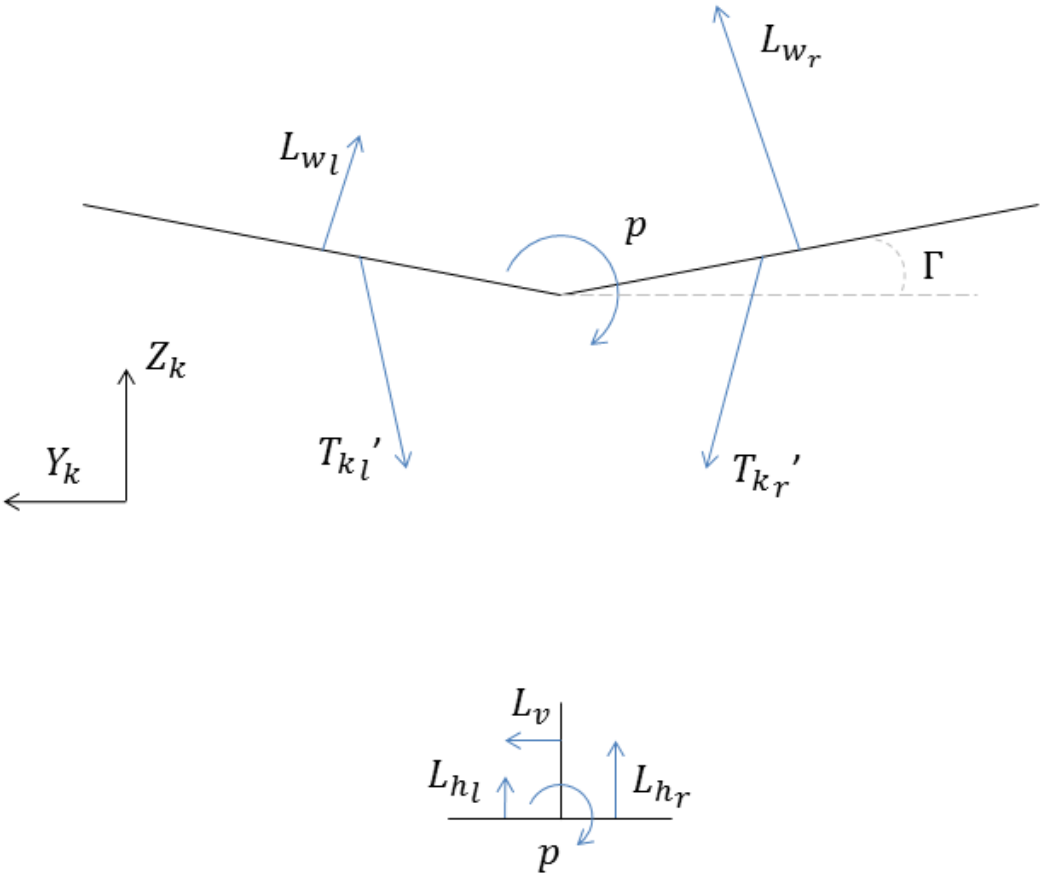

Figure 6.7: Free body diagram during roll motion

Overall, the resulting forces created by the roll rate create a counter moment that acts in the opposite direction. Therefore;

$$\frac{dC_{m_x}}{d\alpha} < 0 \tag{6.29}$$

That would mean the kite has roll stability.

Another motion in lateral stability a kite can have is the yaw motion. The forces that play a significant roll for yaw stability can be found in figure 6.8.

The forces drawn in the figure are also listed in table 6.10. Note that the lift forces on the wing are only components of the total lift force acting in the relevant direction.

With a positive yaw motion assumed, the left wing will have a higher velocity than the right wing. Due the fact the drag and lift force are a function of airspeed, both forces will increase on the left wing and decrease on the right wing. The drag force will act in the opposite direction of the motion and therefore will contribute to yaw stability. The component of the lift force in y-direction will create a moment in the direction of the motion and make the kite unstable. For the horizontal tail, the same situation occurs. However, the tail has no dihedral and therefore no lift component that has a contribution on the yaw motion. Here only the drag in opposite

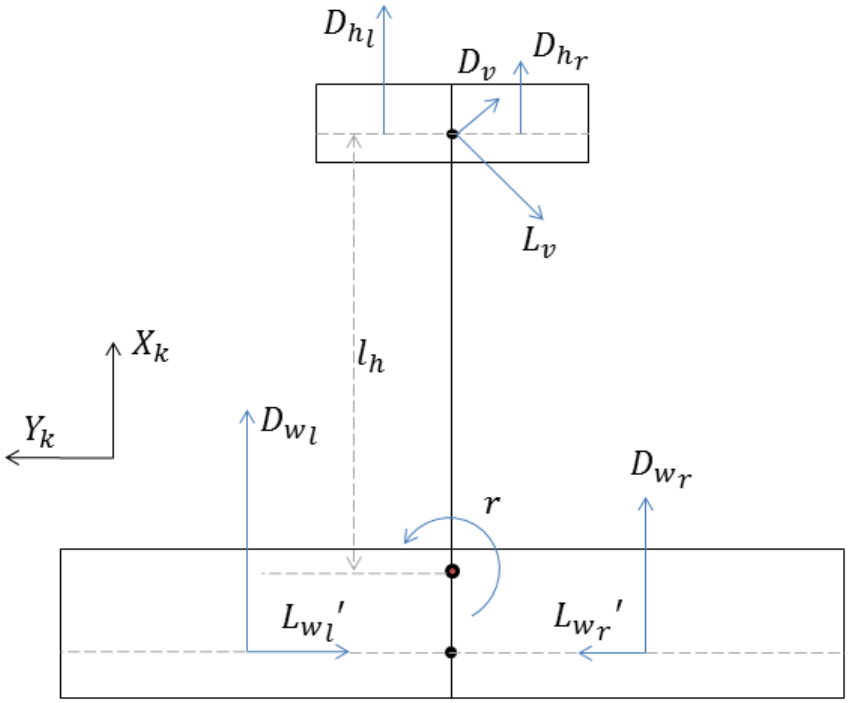

Figure 6.8: Free body diagram during yaw motion

airspeed direction is present and will contribute to the moment to counter the yaw motion. The vertical tail gets into a location where is has an angle of attack and will generate lift and drag force. Both the lift and drag of the vertical tail act in opposite direction to the yaw motion and will create a counter moment. Overall, the moment derivative with respect to the angle of attack can be seen as negative:

$$\frac{dC_{\mathrm{M_z}}}{d\alpha} < 0 \tag{6.30}$$

Therefore, this kite configuration has positive yaw stability.

6.4 Dynamic stability

Now the kite is designed for static stability, the design is analyzed to check if dynamic stability is also present. For this analysis, only the symmetrical eigenmotions are considered. The asymmetrical motions are not taken into account because not all the required stability derivatives are known in this phase of the design. All stability derivatives for the symmetrical motion are approximated with the use of Roskam [16]. In this section the short period and the phugoid motion will be analyzed and the corresponding eigenvalues will be calculated. From these eigenvalues, a statement can be made about the dynamic stability. At last, the period and half time of each motion will be calculated.

Table 6.10: Symbol explanation for figure 6.8

Parameter	Definition
$L_{w,l}$	Lift force due left wing
$L_{w,r}$	Lift force due right wing
$D_{w,l}$	Drag force due left wing
$D_{w,r}$	Drag force due right wing
$D_{h,l}$	Drag force due left horizontal tail
$D_{h,r}$	Drag force due right horizontal tail
L_v	Lift force due vertical tail
D_v	Drag force due vertical tail

6.4.1 Stability derivatives

To calculate the eigenmotions of the kite, several stability derivatives are necessary. For an analytical approximation of these derivatives, Roskam [16] is used. Equation 6.31 to 6.44 are the formulas used to obtain the stability derivatives. Here, the force coefficients are stated as follows from table 6.11.

Table 6.11: Force coefficients for calculation of stability derivatives

Parameter	Definition
C_D	Drag force coefficient
C_L	Lift force coefficient
C_M	Moment coefficient
C_T	Trust force coefficient
C_X	Force in x-direction coefficient
C_Z	Force in z-direction coefficient

With respect to the initial mode (gliding/traction), the derivatives are defined as follows:

$$C_{D_0} = C_{D,mode} \tag{6.31}$$
$$C_{L_0} = C_{L,mode} \tag{6.32}$$
$$C_{T_0} = C_{D_0} + C_{L_0} \tan(\theta) \tag{6.33}$$
$$C_{Z_0} = -C_{L_0} \tag{6.34}$$
$$C_{X_0} = 0 \tag{6.35}$$

Here, the $C_{D,mode}$ and $C_{L,mode}$ are the drag and lift coefficient during normal flight. These values were calculated using XLFR5.

The derivatives with respect to airspeed u are defined in equations 6.36-6.39:

$$C_{T_u} = -3C_{T_0} \tag{6.36}$$
$$C_{Z_u} = -2C_{L_0} \tag{6.37}$$
$$C_{X_u} = -2C_{D_0} \tag{6.38}$$
$$C_{M_u} = 0 \tag{6.39}$$

It is assumed that the moment does not change with airspeed. Therefore, C_{M_u} is assumed to be zero.

The derivatives with respect to the angle of attack α are:

$$C_{D_\alpha} = \frac{2C_{L_0}}{\pi A_w e} C_{L_\alpha} \tag{6.40}$$

The slope of the lift and moment coefficient with respect to the angle of attack, C_{L_α} and C_{m_α}, follow from previous calculations done in section 6.3.

With respect to the pitch rate q, the stability derivatives are defined as follows:

$$C_{M_q} = -2\left(\frac{V_h}{V}\right)^2 \frac{L_h}{\bar{c}} TV \cdot C_{L_{\alpha_h}} \tag{6.41}$$

$$C_{Z_q} = -2\left(\frac{V_h}{V}\right)^2 TV \cdot C_{L_{\alpha_h}} \tag{6.42}$$

$$C_{X_q} = 0 \tag{6.43}$$

With TV as the tail volume, which is equal to $\frac{S_h L_h}{S_w \bar{c}}$. It is assumed that the force in x-direction does not change wing the angle of attack and therefore also does not change with the pitch rate. So, C_{X_q} is assumed zero.

The derivates with respect to angle of attack rate $\dot{\alpha}$:

$$C_{Z_{\dot{\alpha}}} = -2\left(\frac{V_h}{V}\right)^2 TV \frac{d\epsilon}{d\alpha} \cdot C_{L_{\alpha_h}} \tag{6.44}$$

$$C_{M_{\dot{\alpha}}} = -2\left(\frac{V_h}{V}\right)^2 \frac{L_h}{\bar{c}} TV \frac{d\epsilon}{d\alpha} \cdot C_{L_{\alpha_h}} \tag{6.45}$$

Here, $\frac{d\epsilon}{d\alpha}$ is calculated earlier in this chapter for this kite design. The parameters for calculating the derivatives can be found in table 6.12.

Table 6.12: Values used to calculate stability derivatives

Parameter	Traction	Glide
C_L [-]	2.08	0.5623
C_D [-]	0.215	0.112
$\frac{V_h}{V}$ [-]	1	1
$\bar{c}$ [m]	1.386	1.386
S_w [m^2]	12.695	12.695
TV [-]	0.4360	0.4360
L_h [m]	3.9948	3.9948
S_h [m^2]	1.5234	1.5234
$\frac{d\epsilon}{d\alpha}$ [-]	0.4050	0.4050
C_{L_α} [-]	4.680	4.680
$C_{L_{\alpha_h}}$ [-]	3.760	3.760
$C_{L_{\delta_h}}$ [-]	2.7072	2.7072

Using these parameters, the derivatives could be calculated and are presented in table 6.13.

Table 6.13: Stability derivatives for traction and glide phase

Parameter	Traction	Glide		Traction	Glide
C_{D_0} [-]	0.2150	0.2150	C_{D_α} [-]	0.8741	0.0660
C_{L_0} [-]	2.080	0.1570	C_{M_q} [-]	-9.5307	-9.5307
C_{T_0} [-]	1.416	0.3056	C_{Z_q} [-]	-3.0324	-3.2788
C_{X_0} [-]	0	0	C_{X_q} [-]	0	0
C_{Z_0} [-]	-2.080	-0.1570	$C_{Z_{\dot\alpha}}$ [-]	-1.2280	-1.3278
C_{T_u} [-]	-4.2477	-0.9169	$C_{M_{\dot\alpha}}$ [-]	-3.3013	-3.8597
C_{Z_u} [-]	-4.1600	-0.3140	C_{Z_δ} [-]	-0.4061	-0.4061
C_{X_u} [-]	-0.4300	-0.4300	C_{M_δ} [-]	-1.0917	-1.1804
C_{M_u} [-]	0	0	-	-	-

6.4.2 Phugoid

The first longitudinal eigenmotion that is analyzed, is the phugoid motion. To determine if the kite is stable during phugoid, the equations of motion are needed. The full equations of motion of a symmetric flight are presented as equation 6.46.

$$\frac{\bar{c}}{V}\begin{bmatrix} \frac{-2\mu_c}{V} & 0 & 0 & 0 \\ 0 & C_{Z_{\dot\alpha}} - 2\mu_c & 0 & 0 \\ 0 & 0 & -1 & 0 \\ 0 & C_{M_{\dot\alpha}} & 0 & \frac{-2\mu_c K_y^2 \bar{c}}{V} \end{bmatrix} \begin{bmatrix} \dot{u} \\ \dot{\alpha} \\ \dot{\theta} \\ \dot{q} \end{bmatrix} + \begin{bmatrix} \frac{C_{X_u}}{V} & C_{X_\alpha} & C_{Z_0} & \frac{C_{X_q}\bar{c}}{V} \\ \frac{C_{Z_u}}{V} & C_{Z_\alpha} & -C_{X_0} & \frac{(C_{Z_q}+2\mu_c)\bar{c}}{V} \\ 0 & 0 & 0 & 1 \\ \frac{C_{M_u}}{V} & C_{m_\alpha} & 0 & \frac{C_{M_q}\bar{c}}{V} \end{bmatrix} \begin{bmatrix} u \\ \alpha \\ \theta \\ q \end{bmatrix} + \begin{bmatrix} C_{X_{\delta e}} \\ C_{Z_{\delta e}} \\ 0 \\ C_{m_{\delta E}} \end{bmatrix} \delta_e = \mathbf{0} \tag{6.46}$$

In this form the equations are both analogous to:

$$C_1\dot{\mathbf{x}} + C_2\mathbf{x} + C_3\mathbf{u} = \mathbf{0} \tag{6.47}$$

The matrices C_1, C_2 and C_3 as well as the vectors $\mathbf{x}$ and $\mathbf{u}$ are acknowledged for the symmetric equations.

Here the vector $\dot{\mathbf{x}}$ consists of air speed u, the angle of attack α, the pitch angle θ and the pitch rate q. For the elevator deflection angle δ only the value of -11.371 deg (gliding) is used. This is because a phugoid motion is not possible during the traction and dive phase. During these phases, the kite stays at the same altitude due to the tether. Therefore, the calculations for the phugoid are only done for the glide phase. By substituting the stability derivatives in the equations of motion, the eigenvalues can be calculated. With the use of MATLAB the eigenvalues corresponding to the phugoid motion were determined and are presented in table 6.14.

Table 6.14: Eigenvalues for phugoid motion

	Traction	Glide
λ_{p1}	-0.0269 + 0.1864i	-2.0758
λ_{p2}	-0.0269 - 0.1864i	-0.0043

In table 6.14 the eigenvalues are presented in the form of $\lambda = \xi \pm i\eta$, where ξ is the real part and η is the imaginary part. For the kite to be stable during the phugoid motion, the real part

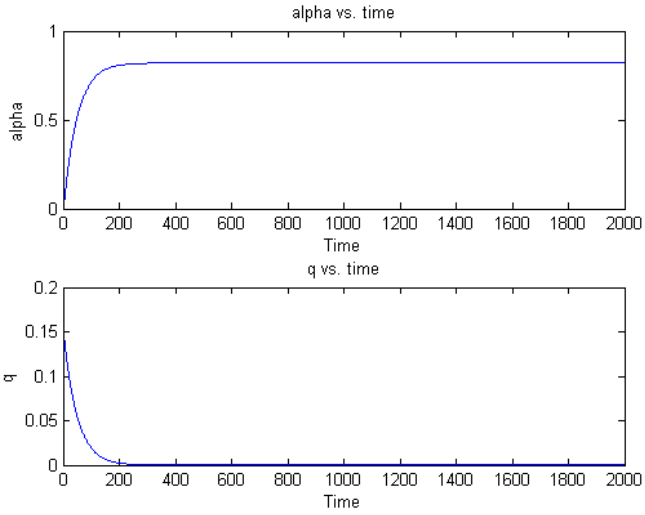

Figure 6.9: Phugoid motion: glide

should be negative. The eigenvalue has a negative real part and therefore is stable. These can be seen in the plots in figure 6.9. Here, the angle of attack and the pitch rate are plotted against time. Also, the motion's half time $T_{\frac{1}{2}}$ and period P are calculated in equations 6.15 for both phases.

$$P = \frac{2\pi\bar{c}}{\xi V} \tag{6.48}$$

$$T_{\frac{1}{2}} = \frac{-0.693\bar{c}}{\eta V} \tag{6.49}$$

Table 6.15: Period and halftime phugoid mode

Parameter	Glide
P [s]	-
$T_{\frac{1}{2}}$ [s]	159.4663

6.4.3 Short period

The other symmetrical motion is the short period. For this eigenmotion, the eigenvalues can also be calculated with the symmetrical equations of motion 6.46. This again is done for both the traction phase and the gliding phase. For the elevator deflection angles δ the value of -11.3707 deg (glide) and -4.979 deg (traction) is used. See table 6.16 for the results.

Table 6.16: Eigenvalues short period

Parameter	Traction	Glide
λ_{s1}	-0.8374 + 0.2296i	-49.5531
λ_{s2}	-0.8374 - 0.2296i	-16.5041

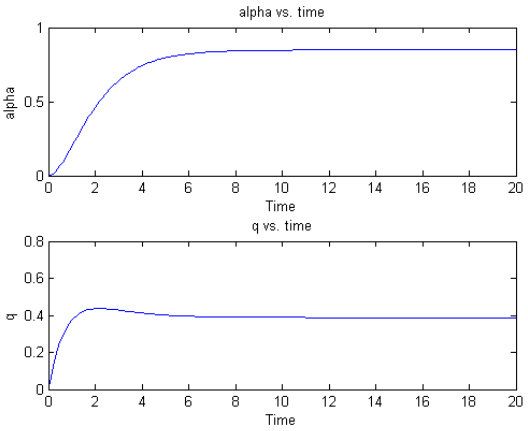

Figure 6.10: Short period: traction

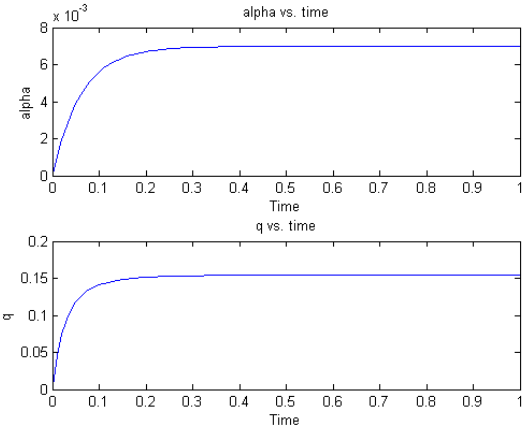

Figure 6.11: Short period: glide

Here, the real parts of both eigenvalues are negative, meaning that these motions are dynamically stable. This can be seen in figures 6.10 and 6.11. Also, the period and half time is calculated for both modes. These values can be found in table 6.17.

Table 6.17: Period and halftime for short period

	Traction	Glide
P [s]	-	-
$T_{\frac{1}{2}}$ [s]	0.9529	0.0420

Chapter 7

Control

In order to control the kite, control surfaces need to be designed. These control surfaces are the aileron on the main wing, elevator on the horizontal tail and rudder on the vertical tail. In the first section, the aileron design procedure is described and in the following two sections the design of the rudder and the elevator. In the fourth section, the calculations for the resulting hinge moments of the control surfaces are described. Finally the resulting characteristics of the control surfaces are described. All equations and derivations for the design of the control surface are from the book 'Airborn Design: A System Engineering Approach' [17].

7.1 Aileron design

Aileron are the primary control surfaces that allows the kite to be rolled. The differential operation of the two ailerons produces a moment around the longitudinal axis causing a rolling motion. The aileron has an effect on the yawing motion as well. The ailerons are located on the outer portions of the wing, so the lift force generated by the ailerons causes a more effective rolling moment. This is shown in equation 7.1.

$$L_{\mathrm{A}} = 2\Delta L y_{\mathrm{A}} \tag{7.1}$$

Here L_{A} is the rolling moment due to the aileron deflection, ΔL is the difference in the lift and y_{A} the distance from the center of gravity to the center of the aileron. The L_{A} moment can also be calculated with equation 7.2, with S being the wing surface area, b the wing span, C_{R} the rolling moment coefficient and $\bar{q}$ being the dynamic pressure. This dynamic pressure is determined with equation 7.3. Here ρ is the atmospheric density and V_{a} is the apparent airspeed of the kite.

$$L_{\mathrm{A}} = \bar{q} S C_{\mathrm{R}} b \tag{7.2}$$

$$\bar{q} = \frac{1}{2}\rho {V_{\mathrm{a}}}^2 \tag{7.3}$$

C_{R} is calculated with equation 7.4. It is assumed that there is neither sideslip nor rudder deflection.

$$C_{\mathrm{R}} = C_{\mathrm{R}_{\delta\mathrm{A}}} \delta_{\mathrm{A}} \tag{7.4}$$

$C_{\mathrm{R}_{\delta\mathrm{A}}}$ is the aircraft rolling moment coefficient due to aileron deflection and δ_{A} is the aileron deflection.

The kite's rolling drag is calculated with equation 7.5.

$$D_{\mathrm{R}} = \frac{1}{2} \rho V_{\mathrm{R}}^2 S_{\mathrm{tot}} C_{\mathrm{D}_{\mathrm{R}}} \tag{7.5}$$

In equation 7.5, $C_{\mathrm{D}_{\mathrm{R}}}$ is the drag coefficient for the roll motion, S_{tot} denotes the sum of the area of the wing planform, the horizontal and vertical tail area and V_{R} is the velocity in roll. V_{R} is determined with equation 7.6.

$$V_{\mathrm{R}} = P_{\mathrm{R}} y_{\mathrm{A}} \tag{7.6}$$

This velocity is sourced from roll rate P_{R} multiplied by the distance between the kite's center of gravity and the rolling drag center y_{A}.

$C_{\mathrm{R}_{\delta\mathrm{A}}}$, as stated in equation 7.4, is the derivative of the rolling moment coefficient with respect to the aileron deflection. An integration method is used to evaluate this derivative. The solution, after elaboration, is shown in equation 7.7. Where: $C_{\mathrm{L}_{\alpha_{\mathrm{w}}}}$ is the wing lift slope, τ_{A} is the control surface effectiveness of the aileron (see section 7.5), c_{r} is the root chord and λ the taper ratio.

$$C_{\mathrm{R}_{\delta\mathrm{A}}} = \frac{2 C_{\mathrm{L}_{\alpha_{\mathrm{w}}}} \tau_{\mathrm{A}} c_{\mathrm{r}}}{S b} \left[\frac{y^2}{2} + \frac{2}{3} \left(\frac{\lambda - 1}{b} \right) y^3 \right]_{y_{\mathrm{i}_{\mathrm{A}}}}^{y_{\mathrm{o}_{\mathrm{A}}}} \tag{7.7}$$

Using an average value of aileron deflection from the left and right aileron, equation 7.8 is derived. The steady state value of the roll rate $P_{\mathrm{R}_{\mathrm{ss}}}$ comes as a result of the kite rolling with a constant rate. This means that the aerodynamic rolling moment generated by the aileron is equal to the moment of the kite drag in the rolling motion, which leads to equation 7.9. Implementing equation 7.6 in equation 7.5 for the aircraft roll drag where P_{R} is equal to $P_{\mathrm{R}_{\mathrm{ss}}}$, the equation for the steady state roll is derived and shown in equation 7.10.

$$L_{\mathrm{A}} - D_{\mathrm{R}} y_D = J_x \dot{P}_{\mathrm{R}} \tag{7.8}$$

$$L_{\mathrm{A}} = D_{\mathrm{R}} y_D \tag{7.9}$$

$$P_{\mathrm{R}_{\mathrm{ss}}} = \sqrt{\frac{2 L_{\mathrm{A}}}{\rho S_{\mathrm{tot}} C_{\mathrm{D}_{\mathrm{R}}} {y_D}^3}} \tag{7.10}$$

The end goal is to achieve an aileron design that will accommodate the necessary roll requirements within the time limit to achieve a desired bank angle. The required time for the kite to reach the desired bank angle, is a combination of the time to get to the steady state roll rate (t_1) and the time during a steady state roll rate to achieve the desired bank angle (t_{ss}), see equation 7.11.

$$t_{\mathrm{tot}} = t_1 + t_{\mathrm{ss}} \tag{7.11}$$

t_1 is calculated by equation 7.12.

$$t_1 = \sqrt{\frac{2\Phi_1}{\dot{P}_\mathrm{R}}} \tag{7.12}$$

$$\tag{7.13}$$

Where:

$$\Phi_1 = \left(\frac{J_x}{\rho {y_D}^3 S_\mathrm{tot} C_{\mathrm{D_R}}}\right) \ln({P_{\mathrm{R_{ss}}}}^2)) \tag{7.14}$$

$$\dot{P}_\mathrm{R} = \frac{{P_{\mathrm{R_{ss}}}}^2}{2\Phi_1} \tag{7.15}$$

From equation 7.14 one can see that a steady state roll rate higher than $1\,^{\mathrm{rad}}/_{\mathrm{s}}$ is required, because otherwise the bank angle will be negative - actually the roll will be in the opposite direction. t_ss is determined with equation 7.16, where Φ_ss is defined by equation 7.17,

$$t_\mathrm{ss} = \frac{\Phi_\mathrm{ss}}{P_{\mathrm{R_{ss}}}} \tag{7.16}$$

$$\Phi_\mathrm{ss} = \Phi_\mathrm{des} - \Phi_1 \tag{7.17}$$

In the case where Φ_1 is equal or larger than the desired bank angle, the total time to get to the bank angle is calculated by using equation 7.18.

$$t_\mathrm{tot} = \sqrt{\frac{2\Phi_\mathrm{des}}{\dot{P}_\mathrm{R}}} \tag{7.18}$$

7.2 Rudder design

The rudder is used to make the turns (figures-of-eight) in the traction phase. The turn is desired to be small to have a more optimum flight path with respect to the wind. This requires a high bank angle (Φ), but this will results in losing lift due to a less effective wing lift surface area. Therefore a desired turn radius is set to 10 m to perform an acceptable turn and not exceeding a bank angle of 45 deg.

The turn radius (R_t) is determined by implimenting equation 7.19 and equation 7.20 in equation 7.21. This leads to a required radius for a certain value of bank angle. The weight (F_tether) is derived from the tether force, which during powering phase is set as the 'weight' of the kite and equals the resulting wing force (R_w), which is 16 kN. During turns the resulting lift force stays constant and therefore the weight can be determined with this resulting wing force and a certain bank angle. For the speed of the kite V_a and for the mass of the kite m is used.

$$F_\mathrm{tether} = R_\mathrm{w} \cos(\Phi) \tag{7.19}$$

$$F_\mathrm{C} = F_\mathrm{tether} \sin(\Phi) \tag{7.20}$$

$$R_\mathrm{t} = \frac{m{V_\mathrm{a}}^2}{F_\mathrm{C}} = \frac{m{V_\mathrm{a}}^2}{F_\mathrm{tether} \sin(\Phi)} \tag{7.21}$$

With this airspeed and bank angle, the related pitch rate (Q_1) and yaw rate (R_1) are calculated with equations 7.22 and 7.23. This results in a yawing moment (N) for the turn by equation 7.24.

$$Q_1 = \frac{g \sin^2(\Phi)}{V_\mathrm{a} \cos(\Phi)} \tag{7.22}$$

$$R_1 = \frac{g \sin(\Phi)}{V_\mathrm{a}} \tag{7.23}$$

$$N = J_{xz} R_1 Q_1 \tag{7.24}$$

Assuming a coordinated turn, β is equal to zero. The yawing moment coefficient derivative with respect to the turn motion $C_{\mathrm{n_r}}$ is determined with equation 7.25, where $(C_{\mathrm{Y_r}})_v$ is found with equation 7.26.

$$C_{\mathrm{n_r}} = -(C_{\mathrm{Y_r}})_v \frac{l_\mathrm{v}}{b} \tag{7.25}$$

$$(C_{\mathrm{Y_r}})_v = 2 C_{\mathrm{L}_{\alpha_\mathrm{v}}} \left(\frac{V_\mathrm{v}}{V_\mathrm{a}}\right)^2 \frac{S_\mathrm{v} l_\mathrm{v}}{S b} \tag{7.26}$$

The yaw moment coefficient derivative with respect to a change in aileron deflection $C_{\mathrm{n}_{\delta_\mathrm{A}}}$ is determined from the difference in lift of the left and right wing due to the deflection of the aileron. With the related lift over drag ratio, the yawing moment slope due to aileron deflection $C_{\mathrm{n}_{\delta_\mathrm{A}}}$ is derived. This last coefficient consists of the parameters in equation 7.27, and so the rudder characteristics (τ_R) and ($\frac{b_\mathrm{R}}{b_\mathrm{v}}$) are determined to satisfy the coordinated turn requirement.

$$C_{\mathrm{n}_{\delta_\mathrm{R}}} = -C_{\mathrm{L}_{\alpha_\mathrm{v}}} \bar{V}_\mathrm{v} \eta_\mathrm{v} \tau_\mathrm{R} \frac{b_\mathrm{R}}{b_\mathrm{v}} \tag{7.27}$$

These parameters are used in equation 7.28 and will lead to the yawing moment coefficient due to the deflection of the rudder $C_{\mathrm{n}_{\delta_\mathrm{R}}}$.

$$N = \frac{1}{2} \rho {V_\mathrm{a}}^2 S b \left(C_{\mathrm{n}_\beta} \beta + C_{\mathrm{n_r}} \frac{R_1 b}{2 V_\mathrm{a}} + C_{\mathrm{n}_{\delta_\mathrm{A}}} \delta_\mathrm{A} + C_{\mathrm{n}_{\delta_\mathrm{R}}} \delta_\mathrm{R} \right) \tag{7.28}$$

7.3 Elevator design

To design the elevator, the horizontal tail lift slope curve $C_{\mathrm{L}_{\alpha_\mathrm{h}}}$ of $4.68\,{}^1\!/_\mathrm{rad}$ is used as derived in chapter 6. To set up the requirement for the elevator characteristics, equations 7.29-7.33 are used.

$$C_{M_\delta} = -C_{L_{\alpha_h}} \eta_h \bar{V}_h \frac{b_E}{b_h} \tau_E \tag{7.29}$$

$$\bar{V}_h = \frac{l_h S_h}{bS} \tag{7.30}$$

$$\Delta C_m = C_{M_\delta} \delta_E \tag{7.31}$$

$$\Delta M = \Delta C_m \bar{q} S \bar{c} \tag{7.32}$$

$$\Delta M = \ddot{\theta} J_y \tag{7.33}$$

The angular pitch acceleration is determined at the beginning and end of the traction phase. At the start of the reel-in phase the kite will pitch down in the direction of the ground unit and then roll 90 deg to dive back to the start of the traction phase. At the end of the reel-in phase, the kite rolls 90 deg in the direction of the new traction phase velocity, followed by a pitch up maneuver to start the figure-of-eight maneuver again. The angular pitching acceleration $\ddot{\theta}$ required to start the pitch up and down, is the requirement for the elevator design, which is negative for the first maneuver and positive for the second situation. According to table 9.6 from [17], this is determined to be 15 $^{deg}/_{s^2}$ because the kite is highly maneuverable and 15 $^{deg}/_{s^2}$ is the average value for this type of aircraft for a comparable angular pitch acceleration during take-off. Then, with equations 7.29-7.33, the elevator characteristics are determined.

7.4 Hinge moment

Next to the configurations of the control surfaces, also the required hinge moment is determined. This is done to determine the required power. To determine the hinge moment of the control surface, equation 7.34 is used.

$$H = \frac{1}{2} \rho V_a S_c C_c C_h \tag{7.34}$$

Where H is the hinge moment and S_c and C_c are the control surface area and mean aerodynamic chord, respectively. C_h is determined with equation 7.35, where C_0 is the hinge moment coefficient when there is no angle of attack and no deflection present. α_{LS} is the angle of attack of the lifting surfaces and δ_c is the deflection of the control surface.

$$C_h = C_0 + C_{h_\alpha} \alpha_{LS} + C_{h_{\delta_c}} \delta_c \tag{7.35}$$

The angle of attack of the lifting surface is the angle of attack of the kite except for the case of the rudder design. In the case of rudder design, the angle of attack of the lifting surface is determined with equation 7.36. Where the angle is determined with the turn radius (R_t) and the distance of the vertical tail to the tether attachment (l_v).

$$\alpha_{LS} = \arcsin\left(\frac{l_v}{R_t}\right) \tag{7.36}$$

Due the fact that both the horizontal and vertical tail have a symmetrical airfoil, α_{LS} is zero. Also for case for the aileron it is assumed to be zero. The control heaviness parameter ($C_{h_{\delta_c}}$) affects mainly the hinge moment and is assumed to have a typical value of -0.3 $^1/_{rad}$. The other parameter is the control floating parameter (C_{h_α}) and is assumed to be -0.1 $^1/_{rad}$.

7.5 Control surface characteristics

The maximum deflection of the control surfaces is set to 20 deg and the related control surface chord is determined for this deflection. This control surface chord is derived from the control surface effectiveness. This control surface effectiveness is related to the ratio of the control surface chord over lifting surface chord $\frac{C_c}{c}$. This is equal for all control surfaces and determined from figure 7.1 [17].

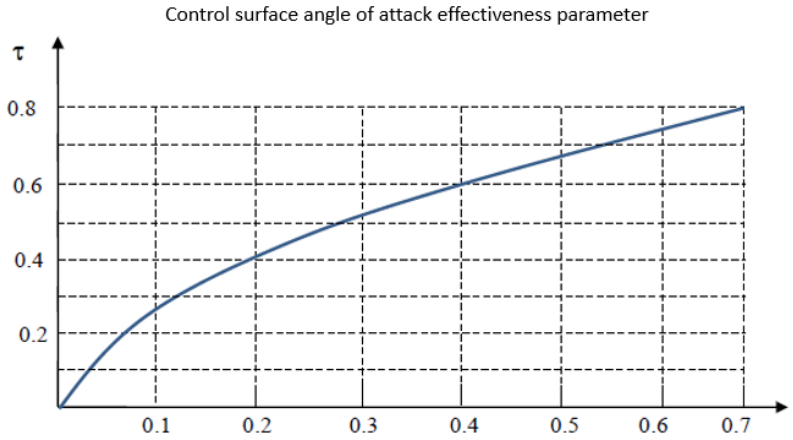

Figure 7.1: Control surface effectiveness parameter as a function of control surface to lifting surface chord ratio

This is followed by the determination of the required deflection angle for the other conditions. The maximum deflection conditions are for the operations at the lowest velocities, because of the squared contribution of the low velocity the control surfaces are less effective. The conditions wherefore the rudder is designed are the turns at 32 m/s and 40 m/s at altitudes of both 100 m and 350 m altitude. For the aileron and the elevator the other conditions are a velocity of 40 m/s at 350 m altitude and the end of dive velocity of 25 m/s at an altitude of 100 m.

7.5.1 Aileron characteristics

The time to bank 90 deg at the start and end of the powering phase is set to 0.6 s (Highly maneuverable aircraft [17]) and leads to the characteristics of the aileron, as shown in table 7.1. As can be seen, a higher aileron deflection is required for lower airspeed, but the aileron deflection stays under the limit of 20 deg. The resultant roll slope coefficient with this aileron configuration is 0.235 1/rad. The aileron span per wing is 2.5 m and the aileron chord length is 0.218 m. The aileron starts at 0.41 % of the half span, at the rib where also the bridle attaches. Also the hinge moments is determined and shown in table 7.1. These hinge moments differ at an altitude of 350 m from -10.44 Nm for a velocity of 32 m/s to -4.61 Nm at a velocity of 40 m/s. At the end of the reel-in phase, at an altitude of 100 m, the required hinge moment is -4.61 Nm.

7.5.2 Rudder characteristics

The roll slope coefficient is used for the determination of the elevator characteristics for a coordinated turn, because during a turn an aileron deflection of 1 deg is used to compensate

Table 7.1: Table of aileron characteristics

Altitude [m]	V_a [m/s]	H_A [Nm]	t_{tot} [s]	δ_A [deg]	c_A [m]	b_A [m]	$\frac{y_{i_A}}{0.5b}$ [−]
350	32	-10.44	0.6	8	0.218	2.5	0.41
350	40	-1.40	0.6	3	0.218	2.5	0.41
100	25	-4.61	0.6	12	0.218	2.5	0.41

for adverse roll. The required elevator characteristics for a 10 m radius or 45 deg bank angle coordinated turn, are derived and shown in table 7.2. It shows that for an identical bank angle with an equal apparent airspeed the required rudder deflection is the same, as can be seen for a velocity of 40 m/s and a bank angle of 45 deg the rudder deflection is 8.7 deg. Also it is noticed that the required deflection angle is lower for lower altitudes and bank angles, so for an altitude of 350 m the required deflection is 6.5 deg and 9.4 deg for an altitude of 100 m. Thus the required deflections are not exceeding the deflection limit of 20 deg. The rudder span is 0.6 m, the rudder chord is 0.123 m. There is only one rudder in the center of the vertical tail, so any rudder deflection will not produce a torque in the tail boom. The maximum hinge moment for the rudder is -0.710 Nm at a velocity of 40 m/s at an altitude of 100 m. For the same velocity at an altitude of 350 m, the hinge moment is -0.591 Nm. For 32 m/s, the hinge moment is also decreasing with increasing altitude 0.493 Nm and the lowest hinge moment of 0.397 Nm as shown in table 7.2. For the hinge moment, the related lift surface, i.e. the v angle due to the hinge moment, is also given.

Table 7.2: Table of rudder characteristics

Altitude [m]	V_a [m/s]	α_{LS} [deg]	H_R [Nm]	Φ [deg]	δ_R [deg]	c_R [m]	b_R [m]	R_t [m]
350	32	21.6	-0.397	40	6.5	0.123	0.6	10.0
350	40	17.9	-0.591	45	8.4	0.123	0.6	15.5
100	32	21.6	-0.493	21	9.4	0.123	0.6	10.2
100	40	21.8	-0.710	45	8.4	0.123	0.6	10.7

7.5.3 Elevator characteristics

Finally the elevator characteristics are determined with the requirements given in section 7.3. The results are shown in table 7.3 and it is shown that the required elevator deflections are higher at lower velocities, namely 5 deg at a velocity of 32 m/s and 3.2 deg at a velocity of 40 m/s. For the transfer motion from reel-in to traction phase a deflection angle of -7.9 deg is required. Half the elevator span is 0.31 m, the elevator chord is 0.093 m. The elevators are in the middle of each horizontal tail part. The hinge moment magnitude for the elevator is increasing from -0.284 Nm to -0.372 Nm with decreasing elevator deflection magnitudes and therefore increasing airspeed. At the end of the reel-in phase, the hinge moment is 0.164 Nm.

Table 7.3: Table of elevator characteristics

Altitude [m]	V_a [m/s]	$\ddot{\theta}$ [deg/s^2]	H_E [Nm]	δ_E [deg]	C_e [m]	b_E [m]	$\frac{y_{o_E}}{0.5b_h}$ [-]
350	32	15	-0.210	4.1	0.093	0.31	0.4
350	40	15	-0.280	2.6	0.093	0.31	0.4
100	25	-15	0.114	-6.5	0.093	0.31	0.4

Chapter 8

Verification and validation

In this chapter verification and validation methods will be applied to the calculations done in the previous chapters. In section 8.1 the aerodynamic calculations done in chapter 4 will be verified. The structural calculations from Chapter 5 will be verified in section 8.2. The stability calculations from chapter 6 will be verified in 8.3. The calculations regarding control surfaces done in chapter 7 will be verified in section 8.4.

8.1 Aerodynamics

Because of the unique aerodynamic case of our kite, it was hard to find data to verify and validate the calculations made with XFLR5. Wind tunnel data for the Wortmann FX73-CL3-152 was found in Stuttgart catalogus [18]. The three-dimensional functions in XFLR5 are actually interpolations of the two-dimensional airfoil analyses. Therefore the 2D data is validated with the windtunnel data. This comparison can be found in figure 8.1.

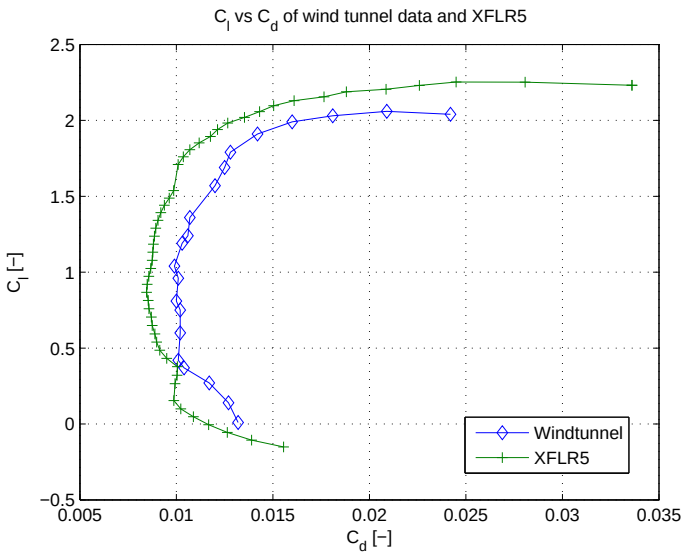

Figure 8.1: Comparison of XFLR5 polars with wind tunnel data.

As can be seen, the lift and drag do differ significantly. Lift is overestimated by ≈6.4 % and drag is underestimated by ≈7 %. The induced drag is calculated in XFLR5 as an addition to pressure drag as a function of C_L. If lift is scaled by its direct decrease and the induced drag component is scaled with $\frac{C_{L_{new}}^2}{C_{L_{old}}^2}$, the total power decrease is only ≈2 kW. This is about 5 %. Therefore for now, the results are considered validated. Further research using more sophisticated software, however, is necessary.

8.2 Structure

There are several structural calculations that require verification. For the main wing the load case calculation, stress analysis and buckling analysis need to be verified.

8.2.1 Stress analysis

The stress analysis consists of a simulation of the wingbox described by a boom model. This model completely describes all loads and the complete shape of the wingbox. In order to verify this calculation a simplified analytical analysis will be applied to a tapered wingbox with a rectangular cross section

In this verification model only the vertical loads are considered, since these are the highest loads. The resulting shear stress due to the shear force, and due to torsion, as well as the normal stress due to bending are calculated at the point of maximum stress. These stresses will then be used to determine a maximum von Mises stress which can be compared to the maximum von Mises stress in the boom model. This maximum von Mises stress occurs at the location where the torsion and shear generate a shear flow in the same direction, and the normal stress due to bending is still maximum, as shown in figure 8.2.

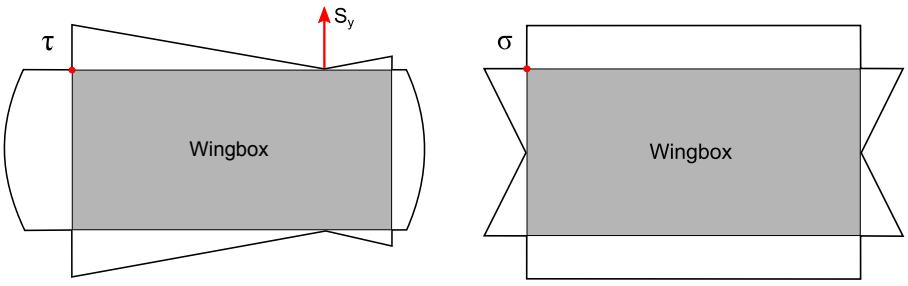

(a) Shear stress (b) Normal stress due to bending

Figure 8.2: The location of maximum von Mises stress

The values for these stresses have been derived in the midterm report [9], the shear flow due due to the shear force S_y generates two shear flows, q_s and q_t:

$$q_s = \frac{S_y w h t}{4 I_{xx}} \tag{8.1}$$

$$q_t = \frac{S_y(\xi - x_{cp})}{2wh} \tag{8.2}$$

Where w is the wingbox width, h is the height, and t the thickness. The expression $\xi - x_{\text{cp}}$ is the distance between the centroid and the center of pressure. These shear flows result in a shear stress through:

$$\tau = \frac{q_{\text{s}} + q_{\text{t}}}{t} \tag{8.3}$$

The normal stress due to bending follows from:

$$\sigma_{\text{z}} = \frac{M_{\text{x}} h}{2 I_{\text{xx}}} \tag{8.4}$$

These can then be used to determine the von Mises stress in the maximum stress point.

$$\sigma_{\text{mises}} = \sqrt{{\sigma_{\text{z}}}^2 + 3\tau^2} \tag{8.5}$$

Finding the values of the wingbox geometry along the span and filling these into the equation results into a distribution of maximum stress along the span which can be compared to the numerical results of the actual wingbox.

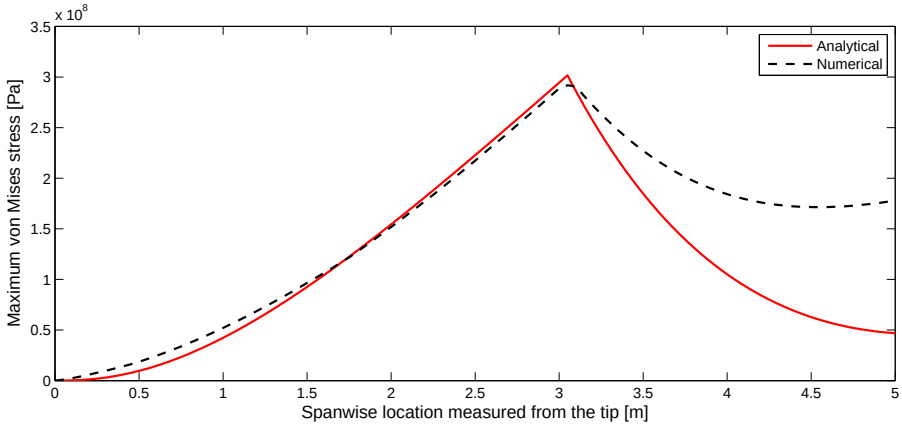

Figure 8.3: Verification of the stress analysis

It shows a clear match until the part where the bending load begins to dominate the stress. After the tether attachment at 3.05 m the discrepancy in moment of area and distance to centroid starts to show in the maximum von Mises stress.

8.3 Stability

For stability, most of the calculation is analytical. This is due the fact that is was not possible to simulate most of the movements of the kite or that the numerical solution was not available. Therefore, verification and validations could often not be done for calculations. For some parts however, verification was accomplished.

The lift slopes C_{L_α}, used for the static stability calculations, determined in XFLR 5 could be verified by the DATCOM method. These calculations are already shown in section 6.3 in the stability chapter. Results for these calculations are found in the same section, table 6.7. Here it

can be seen that the difference between the results of the XFLR5 program and the DATCOM method are negligible.

For the dynamic stability calculations, the full equations of motion obtained from the TU Delft flight dynamics reader are used [1]. In this reader, values from the Cessna Ce500 'Citation' are used to give sample solutions to the equations of motion. The same data is used in the MATLAB code to calculate the eigenvalues and are compared to the solutions given in the reader. The results are presented in table 8.1.

Table 8.1: Verification equation of motion

	Data 'Citation'	Matlab Results
λ_p	-0.0086 ± 0.1954i	-0.0091 ± 0.1930i
λ_s	-1.1601 ± 1.1240i	-1.1698 ± 1.1444i

The difference between the results is less then 1 per cent and can therefore be neglected.

8.4 Control

The calculation done for the design of the control surfaces as shown in chapter 7. These are done algebraically using a file in Matlab to easily adjust the values of the parameters for different conditions for the kite operations or different characteristics of the control surfaces. These calculations are in this section verified by comparing the results to an example. This is done for the aileron, rudder and elevator.

8.4.1 Aileron

To check whether the calculations for the aileron sizing is correct the example for the aileron design of [17] is used. The results of this calculations and from the Matlab code are shown in table 8.2. The only differences present are due to rounding errors. For example the rolling moment coefficient; the small difference affects the further results with around 1 %, thus not significantly

Table 8.2: Table to check aileron calculation

Parameter	Result example	Matlab result
$C_{R_{\delta A}}$ [-]	0.228	0.2279
C_R [-]	0.08	0.0795
L_A [Nm]	42429.6	42430
$P_{R_{ss}}$ [rad/s]	10.181	10.1827
Φ_1 [deg]	9095	9098.2
$\dot{P}_R$ [rad/s^2]	0.327	0.3265
t_{tot} [s]	1.791	1.7909
b_A [m]	2.464	2.4633
c_A [m]	0.29	0.29578
S_c [m^2]	1.4	1.4572

In case when there is no aileron deflections, the Matlab calculations gives a zero lift moment coefficient, which is expected for a symmetrical airfoil.

For the hinge moment Matlab calculations are checked with the result of manual calculations using equations 7.34 and 7.35. Here it can be seen that the only differences between the two way of calculating the solutions is in order of 1 % due to round-off error, as shown in table 8.3

Table 8.3: Table to check the hinge moment

Parameter	manual 1	manual 2	Matlab 1	Matlab 2
ρ [kg/m^3]	1.3	0.9	1.3	0.9
V_a [m/s]	60	70	60	70
S_c [m]	1.4	1.4	1.4	1.4
C_c [m]	0.29	0.29	0.29	0.29
C_0 [-]	0	0	0	0
C_{h_α} [-]	-0.1	-0.1	-0.1	-0.1
α_{LS} [deg]	5	5	5	5
$C_{h_{\delta_c}}$ [-]	-0.1	-0.1	-0.1	-0.1
δ_c [-]	15	20	15	20
C_h [-]	-0.0873	-0.0994	-0.0873	-0.0995
H [Nm]	-82.94	-89.09	-82.9066	-89.0609

8.4.2 Rudder

To check the rudder calculations, manual calculations are made to check with the Matlab code. First the resulting radius turn with the bank angle is evaluated. These calculations are done for all the four condition of the rudder design in section 7.5.2. Then it is compared with the values of the Matlab code with the same conditions as shown in table 8.4. As can be seen the results are exactly the same and it is proven that so far the calculations are valid.

Table 8.4: Table to check radius turn calculations

Condition	manual	Matlab
1	10.0	10.0
2	15.5	15.5
3	10.2	10.2
4	10.7	10.7

Secondly, the yawing moment parameters are determined manually with the results of the rudder and then comparing them with the results from the Matlab calculations. For these calculations the first condition of the rudder design in section 7.5.2 is considered. The results are shown in table 8.5. As can be seen, the results for these parameters have no significant difference. According to these parameters the yawing moment is calculated. The difference in round-off errors is clearly shown. However, when this round-off error is taken into account the result is comparable and it can be concluded that the Matlab code give the desired outputs.

For the calculations of the hinge moment of the rudder the same method and the same parameters are used as in section 8.4.1. The results are the same as in table 8.3, thus these is also correct for the rudder calculation.

Table 8.5: Table to check rudder calculations

Parameter	Manual	Matlab
$C_{n_r} \frac{R_1 b}{2V_a}$ [-]	-0.001839	-0.0018378
$C_{n_{\delta A}} \delta_A$ [-]	0.003668	0.0036586
$C_{n_{\delta R}} \delta_R$ [-]	-0.001769	-0.0018204
$\sum$ [-]	6e(-5)	4e(-7)
$\frac{1}{2} \rho {V_a}^2$ [Nm]	75918	75918
N [Nm]	4.55508	0.0358

8.4.3 Elevator

In order to check the calculations for the elevator design the same procedure is used as for checking the rudder in section 8.4.2. The increase in pitching moment is calculated with the results of the elevator design and compared with the required pitching moment increase according to the requirements following the Matlab calculations, as shown in table 8.6. The difference between the Matlab and manual calculation is neglectable. Also for the hinge moment a check is performed as in the previous sections. The results are again shown in table 8.3. Again can be concluded that the Matlab calculations gives a sufficient way to determine the required control characteristics.

Table 8.6: Table to check elevator calculations

Parameter	Performance (manual)	Requirement (matlab)
ΔM	-11.74667	-11.7548

Part II

AWE system characteristics

Chapter 9

General characteristics

The general characteristics of the AWE system make it possible to do a qualitative comparison, not only with other AWE systems, but with all power generation systems. This chapter will present the method that is used to calculate the average power output of the entire system during one year.

9.1 Optimal reel-in conditions

In the the aerodynamic optimization the reel-out power ($P_{\mathrm{r_{out}}}$) was set to 40 kW, but for the efficiency of the complete system the reel-in power ($P_{\mathrm{r_{in}}}$) needs to be calculated as well. In general, the goal is to maximize the total cycle power output (P_{cycle}), the equation for this power output is indicated in equation 9.1.

$$P_{\mathrm{cycle}} = \frac{P_{\mathrm{r_{out}}} t_{\mathrm{r_{out}}} - P_{\mathrm{r_{in}}} t_{\mathrm{r_{in}}}}{t_{\mathrm{r_{out}}} + t_{\mathrm{r_{in}}} + t_{\mathrm{trans}}} \tag{9.1}$$

Where $t_{\mathrm{r_{out}}}$, $t_{\mathrm{r_{in}}}$ and t_{trans} are the duration of the traction phase, the reel-in phase and the transition phase, respectively. $t_{\mathrm{r_{out}}}$ and $t_{\mathrm{r_{in}}}$ are calculated with equations 9.2 and 9.3, where Δr is variation of tether length during the cycle and $V_{\mathrm{r_{in}}}$ and $V_{\mathrm{r_{out}}}$ are the reel-in and reel-out velocities. t_{trans} is estimated to be 10 s per cycle. $P_{\mathrm{r_{in}}}$ is calculated with equation 9.4, in which the force by which the kite is pulled to the ground station is indicated by $F_{\mathrm{reel-in}}$.

$$t_{\mathrm{r_{in}}} = \frac{\Delta r}{V_{\mathrm{r_{in}}}} \tag{9.2}$$

$$t_{\mathrm{r_{out}}} = \frac{\Delta r}{V_{\mathrm{r_{out}}}} \tag{9.3}$$

$$P_{\mathrm{r_{in}}} = F_{\mathrm{reel-in}} V_{\mathrm{r_{in}}} \tag{9.4}$$

It is clear that for maximum power production $P_{\mathrm{r_{in}}}$ and $t_{\mathrm{r_{in}}}$ need to be minimized. This is done by performing a multivariable analysis where the kite's angle of attack α and reel-in velocity $V_{\mathrm{r_{in}}}$ are optimized for maximum total cycle power output P_{cycle}.

The most important assumptions in this analysis are the following:

- The reel-in phase is a steady state, which means that the velocity is constant and that the kite is in a force equilibrium.
- The flight path of the kite during reel-in has an angle of $\theta = 30\,\text{deg}$ with respect to the Earth reference frame.
- It is considered a 2D problem, where forces in the local y-direction (along the wingspan) are neglected.
- Variation of wind velocity over altitude is not taken into account; the system is optimized for average values of wind velocity at 300 m altitude.
- The weight of the tether has not been taken into account.
- The angle of the tether with the kite is a function of the forces acting on the kite, not depending on the tether weight and reel-in torque at the ground station.

An overview of the forces acting on the kite during reel-in can be found in figure 9.1. In the figure, V_a indicates the apparent wind speed, which is the sum of the reel-in velocity (V_{r_in}) and the wind velocity (V_w), see equation 9.5. Force equilibrium is achieved when equations 9.6 and 9.7 apply, where L and D are the kite's total lift and drag, which are a function of α and V_a according to equations 9.8, 9.9, 9.10 and 9.11. W_kite is the weight of the kite, assumed for this analysis at $45\,\text{kg}\cdot g$. Angles ϕ and γ are calculated according to equations 9.12 and 9.13

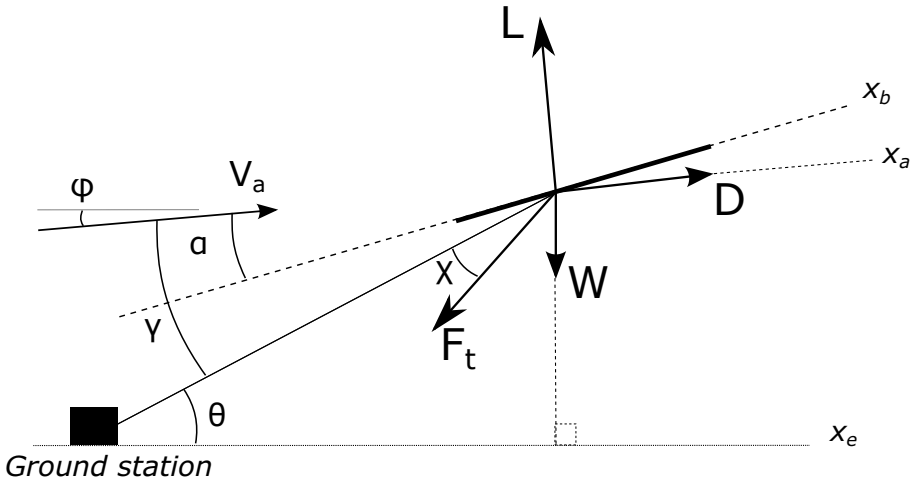

Figure 9.1: FBD of kite during reel-in phase, steady flight assumed

$$\mathbf{V}_\text{a} = \mathbf{V}_\text{w} + \mathbf{V}_{\text{r}_\text{in}} \tag{9.5}$$

$$\Sigma F_\text{z} = 0 = L - W_\text{kite}\cos\phi - F_\text{r}\sin\gamma + \chi \tag{9.6}$$
$$\Sigma F_\text{x} = 0 = D - W_\text{kite}\sin\phi - F_\text{r}\cos\gamma + \chi \tag{9.7}$$

$$C_{\mathrm{L_k}} = \alpha C_{\mathrm{L}_{\alpha_\mathrm{k}}} + C_{\mathrm{L}_0} \tag{9.8}$$

$$C_{\mathrm{D_k}} = C_{\mathrm{D}_0} + \frac{C_{\mathrm{L_k}}^2}{\pi e \mathrm{A}} \tag{9.9}$$

$$L = C_{\mathrm{L_k}} \frac{1}{2} \rho {V_\mathrm{a}}^2 S \tag{9.10}$$

$$D = C_{\mathrm{D_k}} \frac{1}{2} \rho {V_\mathrm{a}}^2 S \tag{9.11}$$

$$\phi = \arctan \frac{V_{\mathrm{r_{in}}} \sin\theta}{V_{\mathrm{r_{in}}} * \cos\theta + V_\mathrm{w}} \tag{9.12}$$

$$\gamma = \theta - \phi \tag{9.13}$$

$$F_\mathrm{r} = \sqrt{(L - W_\mathrm{kite} cos(\phi))^2 + (D - W_\mathrm{kite} sin(\phi))^2} \tag{9.14}$$

$$\chi = \arctan \frac{L - W_\mathrm{kite} cos(\phi)}{D - W_\mathrm{kite} sin(\phi)} - \gamma \tag{9.15}$$

The reel-in force F_r and angle of the tether at the kite χ can be calculated with equation 9.14 and 9.15. The reel-in force is plugged into equations 9.4 and 9.1 to calculate the complete cycle power for multiple reel-in velocities at multiple angles of attack. The results of this analysis are plotted in figures 9.2 and 9.3, where in the first figure the results can be found for a ground wind speed (10 m above ground level) of 5 m/s, and in the second figure the results for a ground wind speed of 12 m/s.

Note the large areas of the graphs that have been set to zero; at these combinations of α and $V_{\mathrm{r_{in}}}$ no force equilibrium could be achieved. In the area on the left of the graph, where α is more negative than -8 deg, the kite produces too little lift to be in equilibrium with the kite's weight; the kite will accelerate towards the ground. In the part of the graph that is equal to zero at angles of attack higher than -8 deg and at low reel-in velocities, there is no force equilibrium along the aerodynamic x-axis; the kite will accelerate into the apparent wind speed direction to reach a velocity at which force equilibrium is obtained.

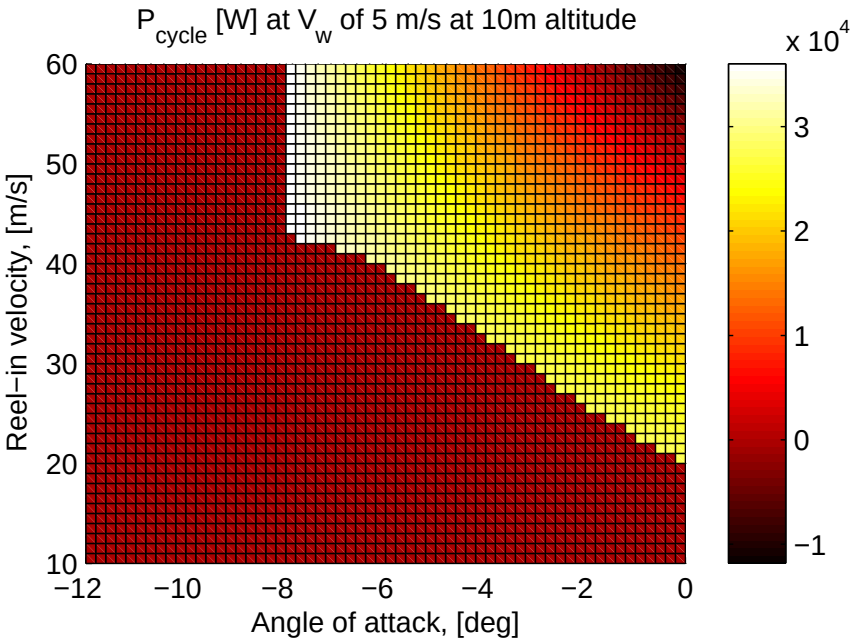

Figure 9.2: P_{cycle} as a function of $V_{\text{r}_{\text{in}}}$ and α at 5 m/s ground wind velocity

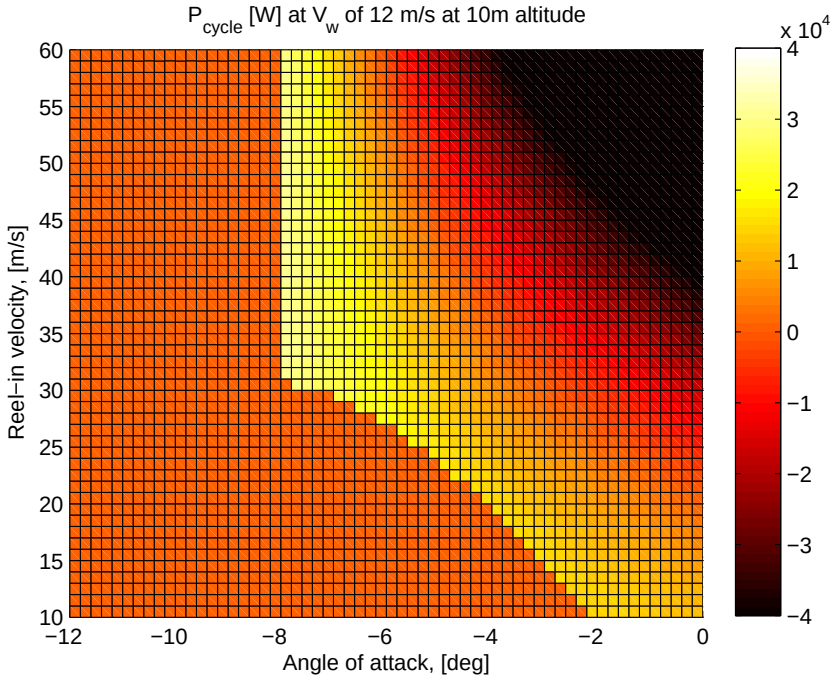

Figure 9.3: P_{cycle} as a function of $V_{\text{r}_{\text{in}}}$ and α at 12 m/s ground wind velocity

Based on the results plotted in figures 9.2 and 9.3, the reel-in velocity ($V_{\text{r}_{\text{in}}}$) is chosen to be 45 m/s and (α) during reel-in is set to -7 deg. The total cycle power output at a ground wind velocity of 5 m/s is 34.6 kW with a reel in force of approximately 0.80 kN. The total cycle power output during a ground wind velocity of 12 m/s is 26.1 kW with a reel in force of approximately 1.3 kN. A plot of the total cycle power output at different ground wind velocities can be found in figure 9.4 in the plot on the right. One can see that with increasing wind speeds the total cycle

power decreases significantly, this is mainly because the reel-out velocity scales with the wind speed, which reduces the duration of the power cycle, while the traction phase power output remains constant. At the same time the required reel-in force increases, which increases the required reel-in power. The decrease in power can be reduced if a lower reel-out velocity is used at higher wind velocities, and trimming the kite to the required traction force by altering the angle of attack in order to reach the required traction phase power output of 40 kW. However, this would require some alterations to the kite; at higher wind velocities the drag of the kite needs to be increased, in this way the kite's velocity will not increase too much.

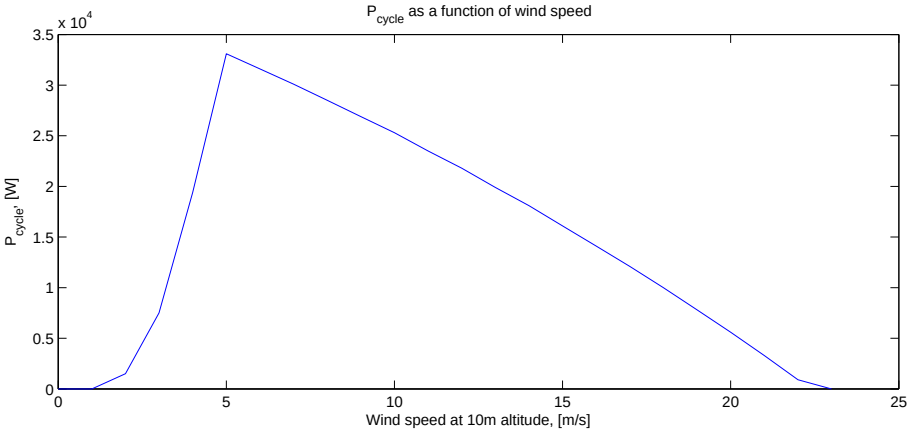

Figure 9.4: Total cycle power output at different wind speeds (with $V_{\mathrm{r_{in}}} = 45\,\mathrm{m/s}$ and $\alpha = -7\,\mathrm{deg}$

9.2 Average cycle power output based on wind data

Now that the total cycle power output is known for multiple wind speeds, the average power output during a year of operation can be calculated by using measurement data on wind velocities. The data that has been used for the wind velocities comes from the Fraunhofer Institute [2] (figure 9 of the document). In figure 9.5 the probability density function (Weibull distribution) of the wind velocities has been visualized. This plot indicates the likeliness of occurrence of a certain wind speed.

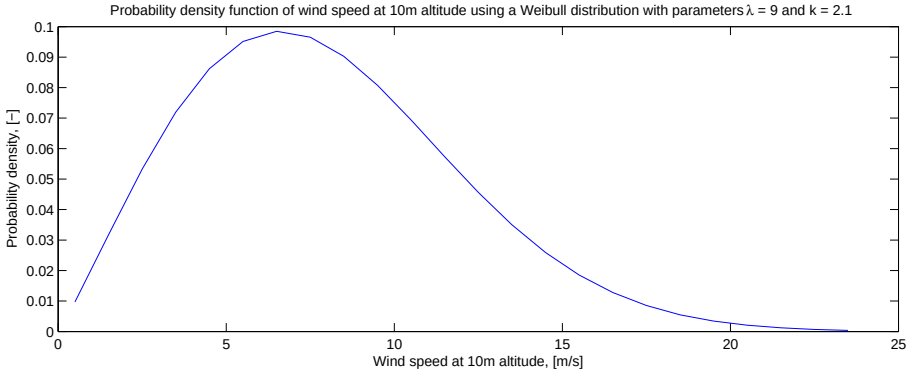

Figure 9.5: the probability density function of the wind speeds based on [2]; a Weibull distribution with parameters $\lambda = 9$ and $k = 2.1$

The Weibull distribution is used as a weight factor on the total cycle power output displayed in

figure 9.4. Taking the sum of the weighted power outputs gives the average cycle power output during a year of operation, which is 22.8 kW. Not taken into account in this average cycle power output, is the time the system will be out of order because of failure, repair and maintenance. This time has been estimated to be 5% of the total operation time. When this factor is included the expected average power output of a single kite system will be 21.6 kW.

Chapter 10

Functional analysis

To get an overview of the pumping kite power generation system its functions are discretized. To get a better feeling of the tasks that will be involved in the system, a Functional Breakdown Structure (FBS) is constructed, which presents the functions in an hierarchical overview. Consequently a Functional Flow Block Diagram (FFBD) is made, which visualizes the logical order of functions the system must perform.

10.1 Functional breakdown structure

In this section the system functions to support the FFBD from figure 10.2 are specified. It divides the system into tasks required to operate the system, without specifying solutions. Therefore the functions in the FBS are performed in parallel, resulting in an hierarchical AND tree. The FBS is shown in figure 10.1.

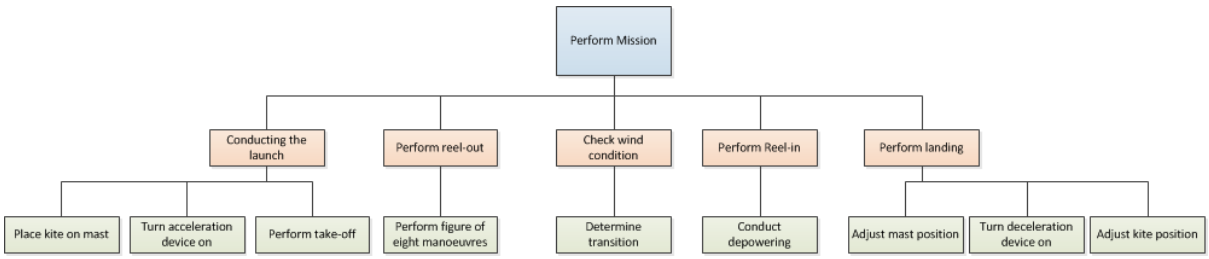

Figure 10.1: Functional breakdown structure

The kite power mission begins with launching the kite. Launching includes placing the kite into the mast,switching on the acceleration device and performing the take-off. Reel-out is performed in a figure of eight. Wind condition check is the part of the mission as it determine the transition phase. Depowering is done by reeling in the kite. Finally landing is performed which include adjusting kite position, turning the deceleration device on and adjusting the mast position.

10.2 Functional flow block diagram

The essential functions in the FFBD are presented in figure 10.2. The functions of the system (in grey) are split up into three main phases, namely the ground phase (green) containing all functions that take place on the ground, normal operation (blue) where the kite is airborne and power is generated, and the safe mode (red). External factors such as weather conditions and inspections during maintenance which lead to different functions are shown in orange. AND and OR decisions during the function flow are displayed in yellow.

Depowering of the kite during normal operation means that the kite needs to let go some pressure, decrease the velocity of the kite and corollary maintain a constant mechanical power supply with the ground station during reel-out. For now it is considered that this can be done by changing the aerodynamic properties of the wing or by adjusting the operational altitude. In the safe mode, the kite will land when the wind speed velocity drops below 6 m/s for a longer period or when there are severe weather conditions. Landing is also required when any components of the kite fails or for routine inspection. When for a short period there is low wind, the kite will go into a reverse 8-trajectory pumping cycle. This cycle requires energy input from the ground station and therefore is only profitable for a shorter period, when a complete landing and take-off causes more energy investment. The wind velocities are based on the requirements from the project objective; a constant mechanical power supply during reel-out at wind speeds between 6 m/s to 12 m/s is required and the maximum operational wind speed is 25 m/s.

In this FFBD the wind conditions are checked only during the transition between reel-out and reel-in to decide if the kite remains in normal operation or should (re-)enter a safe mode. This has been done to clearly show this decision process while keeping the diagram structured. In real life, wind conditions are checked throughout the cycle.

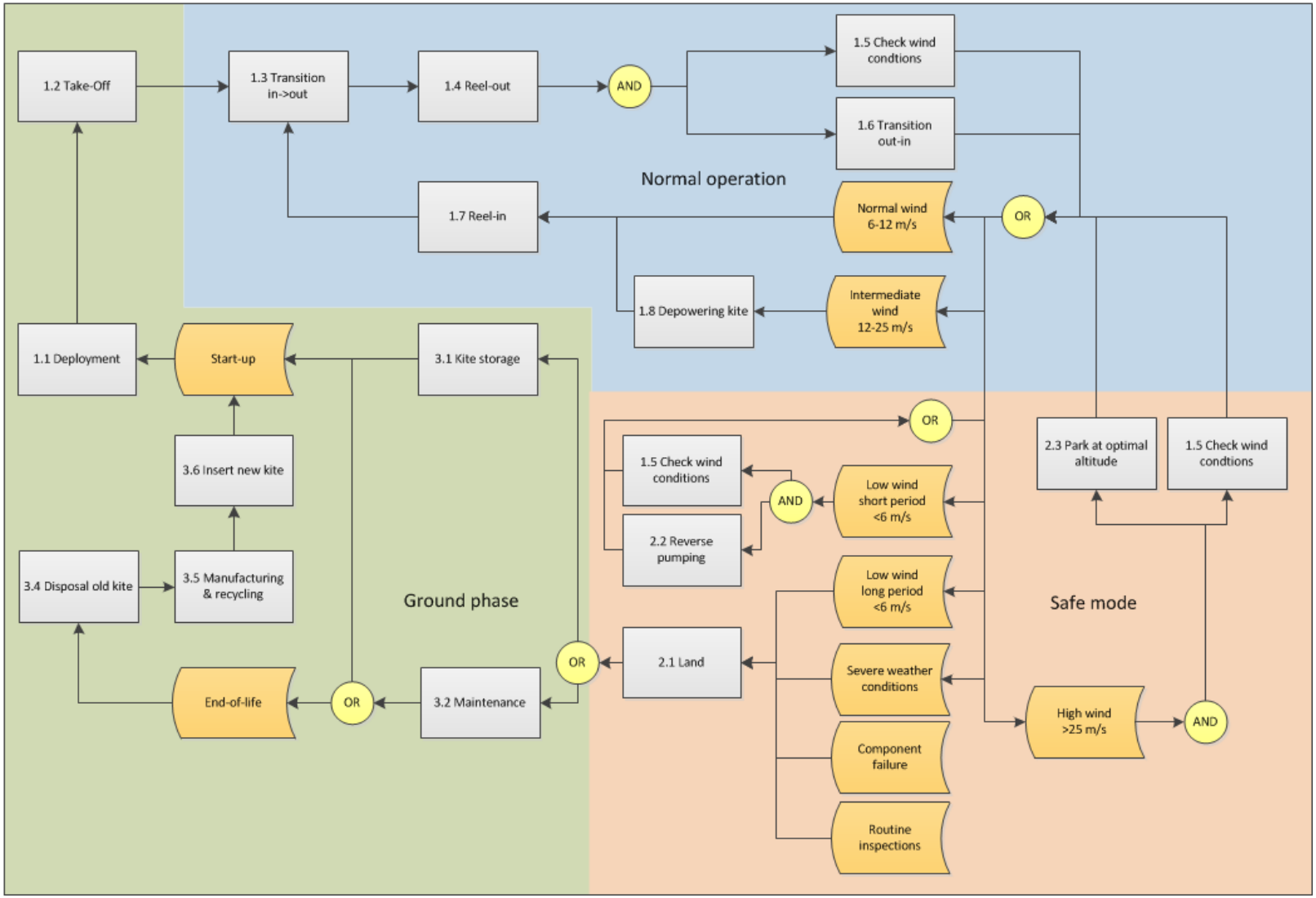

Figure 10.2: Functional flow block diagram

Chapter 11

System interface

After analysing the functions of the AWE system, the system's interaction will now be looked into. The control of an AWE system should be clear and concise. Clear, so that one can always have an overview on the sequences. If there is an error, it can always be traced back. Concise, because each operation takes a certain amount of time. The more operations there are in sequence, the more time it will take. In this chapter the communication between the different subsystems in section 11.1 is provided along with the control architecture, in section 11.2, for the complete system. An explanation of the different control subarchitectures will be presented as well. In section 11.3 an overview of the electrical equipment is given.

11.1 Communication

The different subsystems of the AWE system should be able to communicate with each other. Figure 11.1 shows how these subsystems communicate. It should be noted that all data obtained from the sensors is first send to the control box, amplified and then transmitted to the ground to be processed.

The ground station can receive additional information from either the weather centre or compulsory commands as manual input. The appropriate procedure is determined and then transmitted to either the sensors (to start data acquisition) or to the actuators (to steer the kite with control surfaces).

11.2 Control architecture

A control architecture is used in order to have a detailed view on the interfaces of the subsystems. In this way, not only the control protocol can be monitored, but it also makes it more accessible when correcting for malfunctions. Figure 11.2 shows the main control architecture.

The main control architecture is subdivided into four subarchitectures; namely, take-off, landing, safe mode and operational manoeuvre. These subarchitectures are given in figures 11.3 to 11.9. The

"Transition determination" box is used in order to discern from the different inputs which output is the correct one. Per sequence there will be only one output. All data processing will

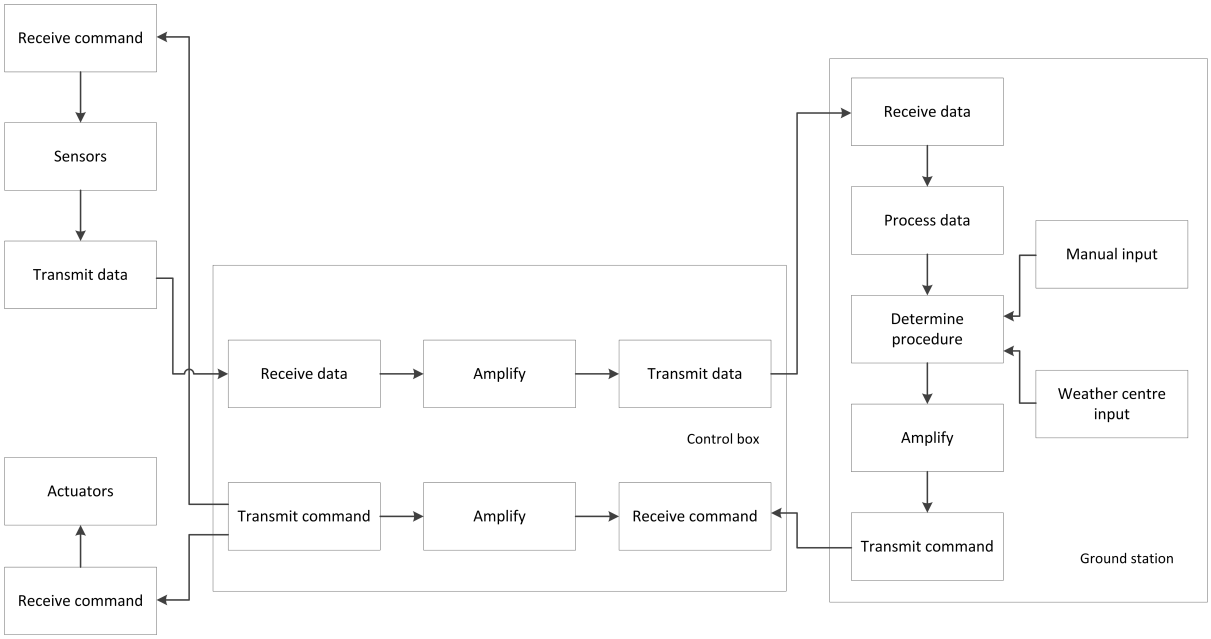

Figure 11.1: The communication flow diagram for the AWE system

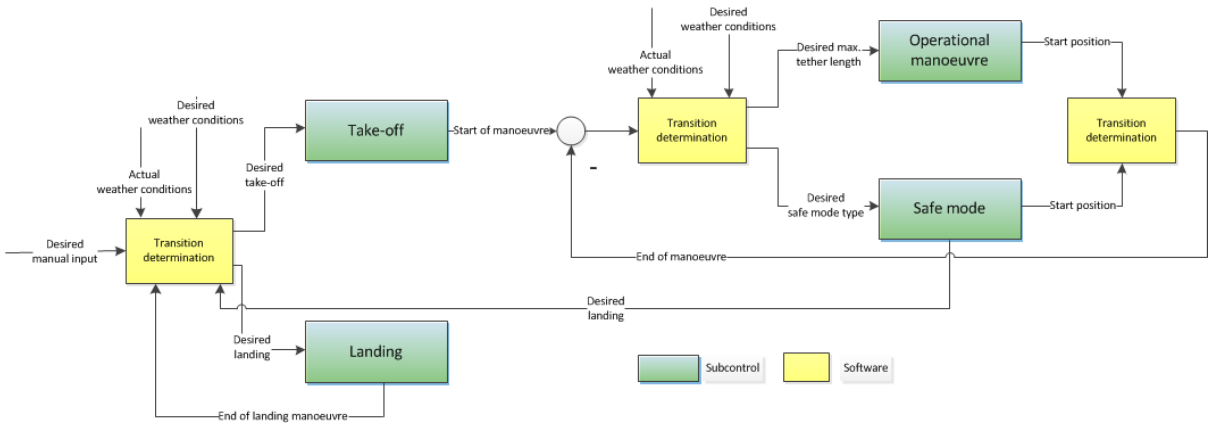

Figure 11.2: Main control architecture for the AWE system

be done at the ground station. In addition, a distinction is made between the colour of the boxes (as indicated in the legend of each architecture) in order to specify the types of actions undertaken by the hardware from those done by the software.

11.2.1 Operational maneuvre

During operation the kite will be doing two maneuvres in sequence, which make up two phases, the traction phase and the reel-in phase.

11.2.2 Maneuvres

The traction phase architecture, as shown in figure 11.4, will be done more than once per sequence depending on whether the maximum tether length is reached.

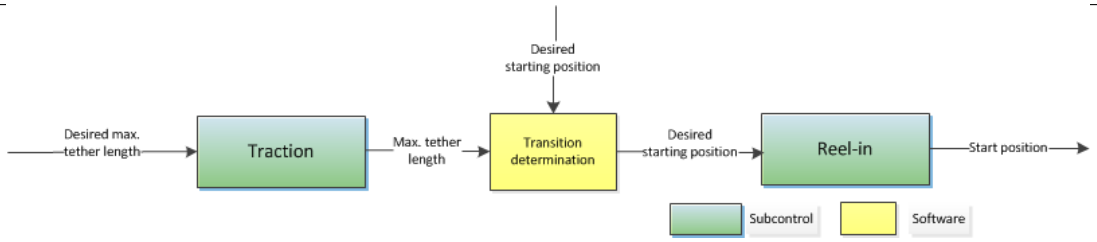

Figure 11.3: Operational maneuvre

The attitude of the kite will be monitored at all time and it will make proper adjustments when the kite is subjected by disturbances. Also the altitude is measured. But altitude, in this case, does not refer to the height at which the kite is flying, rather to the tether length at an instance in time. At the end, when the maximum tether length is reached, the system will give an output signal (dotted arrow) so that the de-powering of the kite can begin.

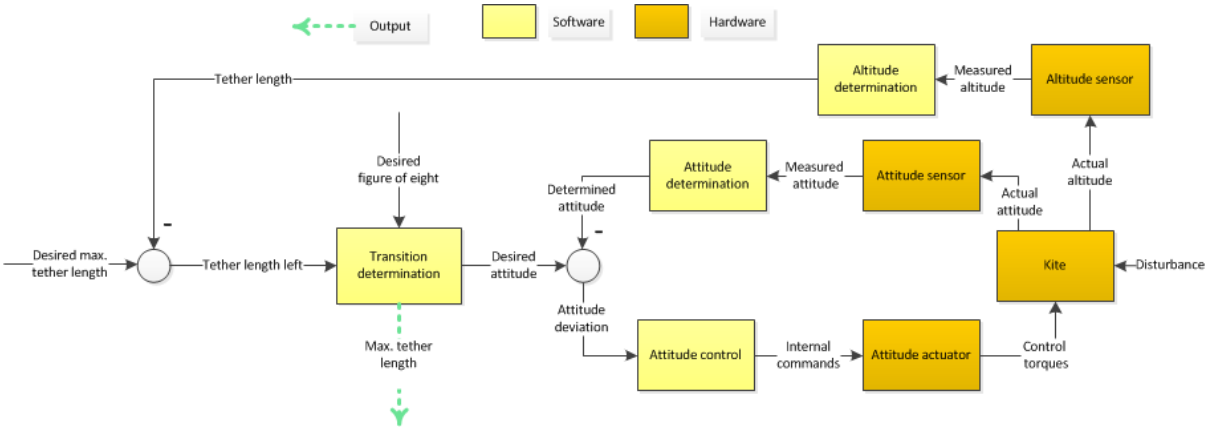

Figure 11.4: Traction phase control subarchitecture for the AWE system

Figure 11.5 shows the reel-in architecture. During de-powering the attitude of the kite will be changed and corrected when disturbances occur. And, since it is the de-powering phase, the maneuvre will end when the kite reaches the position for restarting the traction phase. At that instant, the system will give an output signal that will then be processed (in the transition determination, as shown in figure 11.2.

11.2.3 Safe mode

The safe mode subcontrol consists of two cases. The first case is the high wind safe mode, where the kite is parked at a higher altitude. The second case is the low wind safe mode, where, for short periods of low wind, the kite is kept in the air by reverse pumping (putting energy in the system to keep the kite airborne). When low wind conditions are present for a longer period the kite is landed, this operation will be covered in section 11.2.4. Figure 11.6 and figure 11.7 show respectively the high wind and low wind safe mode control architecture.

During the high wind safe mode the kite will change its attitude in order to get to higher altitude. Effects due to disturbances are also taken into account. Once the desired parking altitude is reached, the sequence will terminate and the system will be pending for a different input. This input will be from either the weather sensors (for restarting the traction phase) or

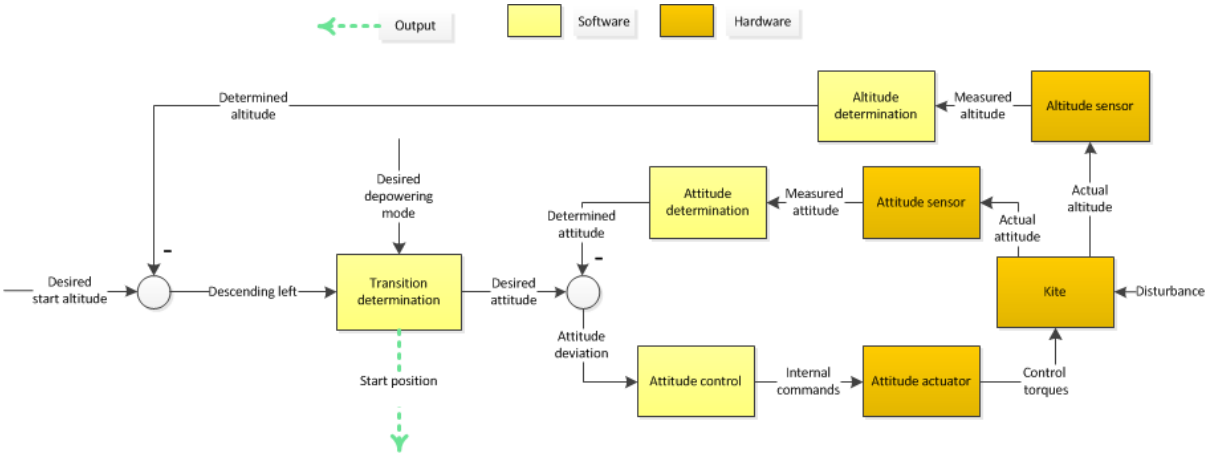

Figure 11.5: Reel-in phase control subarchitecture for the AWE system

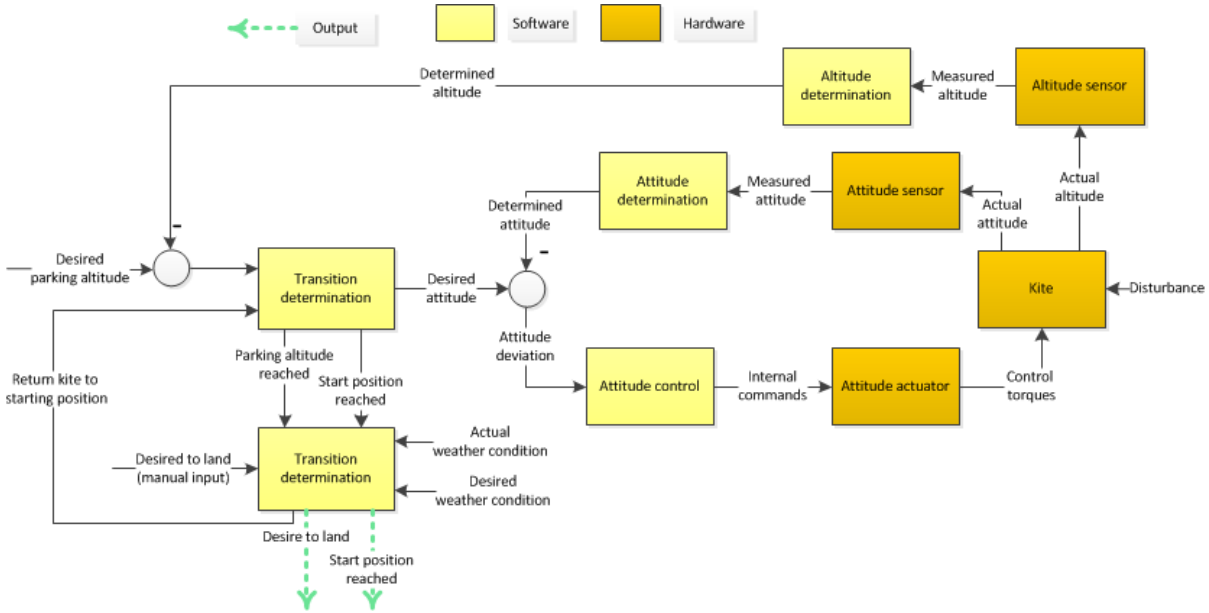

Figure 11.6: High wind safe mode - Parking control subarchitecture for the AWE system

from manual input (for a forced landing).

During the low wind safe mode the kite is reeled-in without depowering the kite, in this way the kite gains altitude from where it glides back on the wind, reeling out the winch. In this way the kite is able to stay in the air endlessly, however this operation requires energy input and is therefore not applicable for longer periods of time. The low wind safe mode architecture is shown in figure 11.7. If the wind speed reaches the operational speed range again, then the kite will do the reel-in subcontrol maneuvre in order to get into the starting position.

11.2.4 Take-off and landing

The launching and landing control architectures are given in figures 11.8 and 11.9, respectively. This project is mainly focused on the kite itself and therefore the launching and landing maneuvres are considered on a lesser level. Therefore the control sequences for these are not expanded.

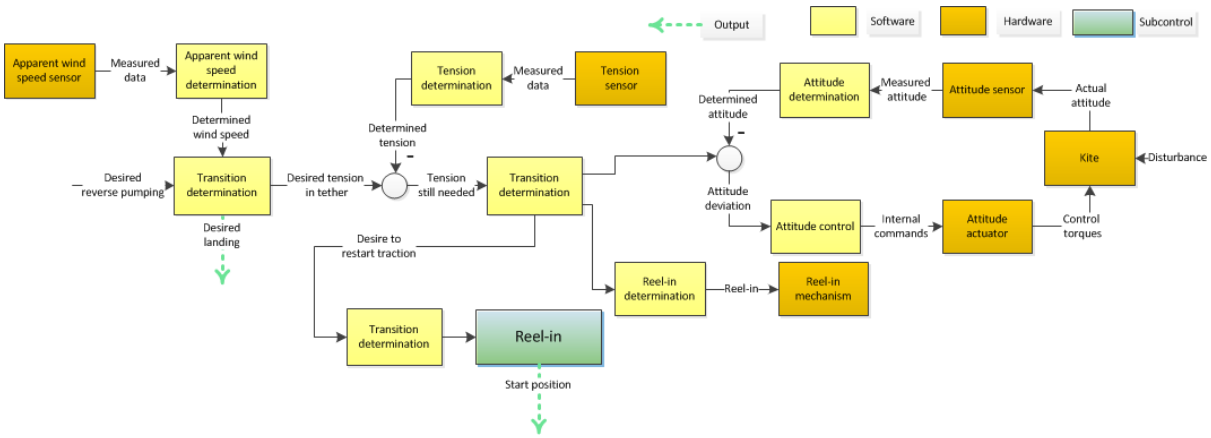

Figure 11.7: Low wind safe mode - Reverse pumping control subarchitecture for the AWE system

An extended explanation on the launching and landing maneuvres can be found in chapter 12.

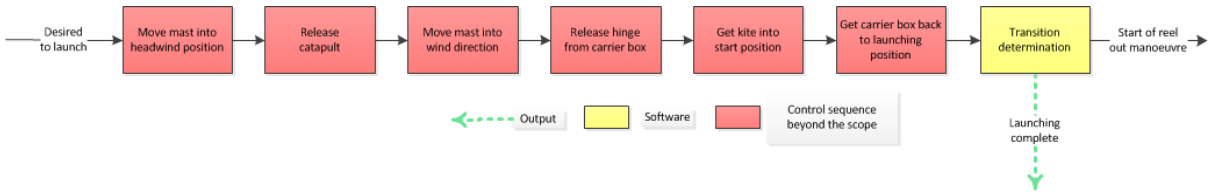

Figure 11.8: Take-off phase control subarchitecture for the AWE system

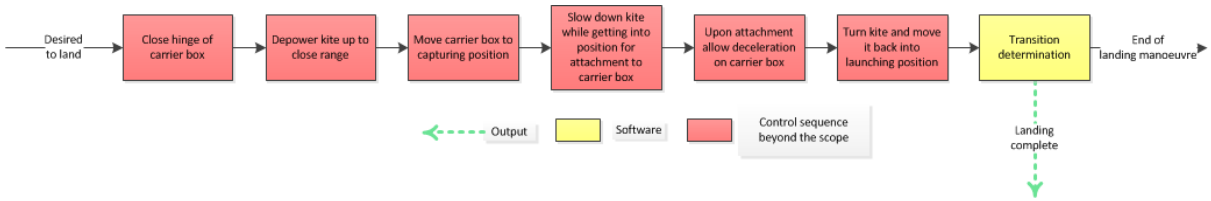

Figure 11.9: Landing phase control subarchitecture for the AWE system

11.3 Electrical equipment

The pumping kite power generation system consists of two different mechanisms that can generate power; namely, a small turbine which is positioned on the kite and the reeling drum-generator located on the ground.

The turbine converts the wind energy into mechanical energy which in turn will be converted into electrical energy using a generator. This electrical energy is send through a Power Processing Unit (PPU) and is then stored into an on board battery. From this battery then the energy is send through the PPU which gets distributed among the actuators, sensors, transmitters and receivers. An overview of these relations is given in figure 11.10a.

The main power generation takes place by using a reeling drum-generator. During the traction phase the kite converts wind energy and gravitational energy into mechanical energy. This is then converted into electrical energy in the generator on the ground. From the generator, as

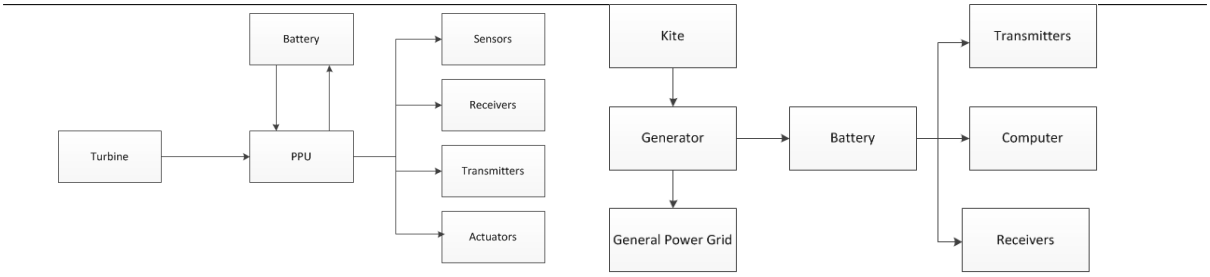

(a) On board power provision

(b) Power provision on the ground

Figure 11.10: Electrical block diagrams

seen in figure 11.10b, a small portion of the energy is send to the battery for the ground station and the rest is send to the general power grid. The transmitters, receivers and processors receive their power from the battery located on the ground.

Chapter 12

Take-off

This chapter covers the take-off system for the kite. First, some options from literature are explored in section 12.1. Then, the chosen concept with associated maneuvers is elaborated upon in section 12.2. This is followed by the energy and power required for the take-off maneuver are calculated and presented along with the assumptions for this system in section 12.3. The system is not worked out in full detail, because the focus of the project was on the kite itself.

12.1 Current methods for take-off

Several options for the launch and landing system have been assessed and a choice is made. The concepts are based on the options currently in use in the market. An important aspect to take into consideration is that the system should be fully automated; keeping this in mind, the following systems are investigated:

1. A telescopic mast: this mast has a telescoping property that allows it to extend to higher altitudes to aid in launch at a higher wind speed. It is suitable especially for flexible kites as they tend to be lighter than their rigid counterparts. On examination of the mast, it was found unsuitable for the intended purpose. The reasons for this are:
    - An increase in the links that are required to make the mast telescope. This involves multiple moving parts and eventually weakened areas due to the connecting links.
    - The cut in speed of the kite is lower than its cut-in wind speed and there is no set altitude at which this wind velocity is to be found. A 'static' start is therefore not considered feasible.
    - Additional required movable parts of the telescopic mast increase the weight of the structure.
2. Propeller launch: propellers are installed on the wings of the kite and they launch the kite from a secure stowed position on a mast. Once the kite has arrived at the operational attitude, it begins to carry out its power generating maneuvers. To land, the opposite actions are carried out to bring it back to the mast and land safely. Although a small turbine is already installed, a redesign of this should be done for the higher power requirements for aiding in a take-off maneuvre. This is deemed to have too much adverse effects on power generating performance since it would require a much larger turbine than currently used, leading to additional drag.

3. Swivelling mast: to launch, the mast rotates at a certain speed at which the kite has enough velocity to climb. Then the tether extends so that the kite can get to operating altitude. The reverse process is followed to land the kite. This concept is not in actual operation, but is still in the development phase. Knowing this, the concept falls out of contention as there is no actual practical data proving this system to work.

4. Winch launch: the kite is brought away from the ground station by some sort of cart. From there, it is pulled towards the ground station by reeling in against the wind. It is similar to a normal sailplane take-off. The automation with which to bring the kite away from the ground station is considered too complex with too many possibilities for failure.

5. A launch system: the kite is launched from a track using a high torque electric motor. It is already used for military drones and has a track record.

System 5 is considered to be the most feasible and is worked out in more detail.

12.2 The take-off concept applied

The concept is a mast with a high torque motor. The launch and landing system to be used involves a mast onto which a high torque motor is mounted. This launches the kite up to a certain altitude. The base of the mast is set on a platform that rotates to allow the mast to be pointed in any direction.

At take-off, the mast is set to a 90 deg angle. The kite is launched to a certain altitude and from there it glides down and with the wind to 200 m distance and 30 m altitude. At the 30m point the kite steers back towards the ground station and is then reeled-in such that the kite gains altitude.

For the landing procedures, the kite is brought down by gliding and is reeled-in towards the ground station. The tether is also being reeled-in simultaneously; the kite is then guided to land on the carrier box on the mast which is now lowered to a horizontal position.

12.3 Feasibility of the take-off concept

The take-off maneuver can be be split into two phases. The first phase is the ascending maneuver followed by a gliding maneuver. The second phase is the reeling-in of the kite to gain altitude. The second phase will not be further discussed in this report, since the ground station itself is already technically capable of this. Figure 12.1 is a sketch of the first phase.

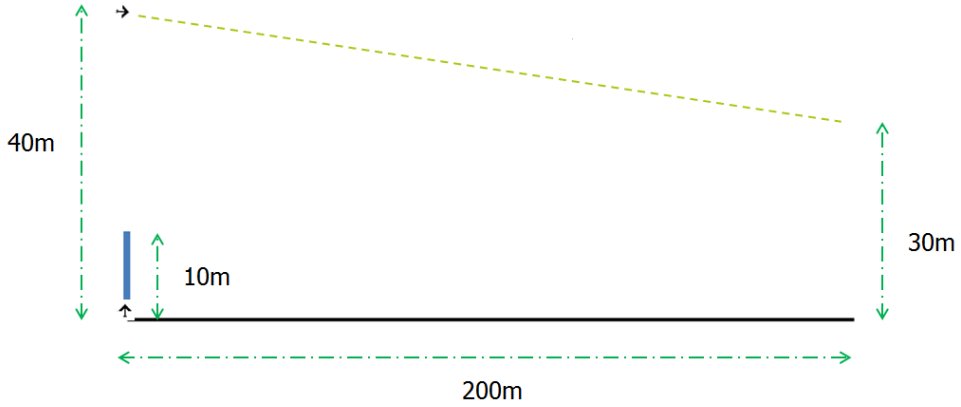

Figure 12.1: Sketch of the first phase of the take-off maneuver

There are two parameters of which their values are specified beforehand. These are: the height reached after gliding ($h_{aft_{gl}} = 30$m) and the distance reached after gliding ($w_{aft_{gl}} = 200$m). The height of the kite after gliding is chosen such that there will be enough space for transitioning. The distance reached after gliding is chosen such, that there will be enough tether length to get the kite into the starting position. Using figure 12.1 along with the conservation of energy method the different parameters can be computed. It should be noted that in these calculations aerodynamic effects are not taken into account. This means lift, drag and wind velocity are omitted from the analysis.

The conservation of energy is applied in equation 12.1. In this equation, the end of the mast, i.e. 10 m with respect to the ground, is defined as the starting point (using subscript '1'). Also, the altitude the kite should reach, i.e. 40 m, is taken as the end point (using subscript '2'). This altitude follows from the kite's glide angle ($\gamma_{\text{glide}} = 2.86$deg). The following calculations follow:

$$E_{k_1} + E_{p_1} = E_{k_2} + E_{p_1} \tag{12.1}$$

With E_{k} as the kinetic energy and E_{p} as the potential energy; each at the respective points. Writing out equation 12.1, gives:

$$\frac{1}{2}mV_1^2 + mgh_1 = \frac{1}{2}mV_2^2 + mgh_2 \tag{12.2}$$

Rearranging and filling in the respective values gives:

$$V_1 = \sqrt{\frac{\frac{1}{2}mV_2^2 + mgh_2}{\frac{1}{2}m}} = 24.99\,\text{m/s} \tag{12.3}$$

Thus, the velocity that the kite has to have at the end of the rail is approximately 25 m/s. The time that is needed to get the kite to reach this velocity is equal to:

$$t_{\text{rail}} = \frac{s_{\text{rail}}}{V_{\text{avg}}} = 0.8\,\text{s} \tag{12.4}$$

with V_{avg} taken as $\frac{V_1}{2}$ since the acceleration (a_{rail}) is assumed to be constant.

Then, the required acceleration is computed as follows:

$$a_{rail} = \frac{s_{rail}}{\frac{1}{2}t_{rail}^2} = 31.25\,\mathrm{m/s^2} \approx 3.2\mathrm{g} \tag{12.5}$$

Also the power required to perform this maneuver is equal to:

$$P_{rail} = \frac{E_{k_1}}{t_{rail}} = \frac{\frac{1}{2}mV_1^2}{t_{rail}} = 17.58\,\mathrm{kW} \tag{12.6}$$

It can be concluded that the motor should be able to give the kite a starting velocity (for the ascending maneuver) of 25 m/s with an acceleration of 3.2g. Now the necessary torque can be computed.

12.4 Take-off torque motor

To launch the kite to the operational attitude, a system that employs a high torque motor is applied. The purpose of this torque motor is to generate a very high torque in a very short period of time and thus launch the kite at the required velocity. It is required that at the end of the launch mast, the kite has to have a velocity of $V_1 = 25\,\mathrm{m/s}$ and a required power level denoted $P_{rail} = 17.58\mathrm{kW}$. The motor is sized for such initial conditions.

To calculate the angular velocity ω_m:

$$\omega_m = c_{RPM}\frac{2\pi}{60} \tag{12.7}$$

with c_{RPM} as the revolutions per minute (RPM).

To find the value of the torque needed, τ_m, the following equation is used:

$$\tau_m = \frac{P_{rail}}{\omega_m} \tag{12.8}$$

Assuming a motor that has a 50% efficiency, table 12.1 is generated that gives several options for radius and torque rating.

c_{RPM}	Angular velocity, ω_m [rad/s]	Torque, τ_m [Nm]	Drum radius, D_m [m]
3450	361.28	48.66	0.07
2000	209.44	83.94	0.12
1000	104.72	167.88	0.24
500	52.36	335.75	0.48

Table 12.1: The various radii and torque ratings of the motor drum at various RPMs and angular velocities

These figures are not a final authority on the sizing of the take-off motor system. There is still room for further development in this area.

Part III

Development projections

Chapter 13

Financial projection

In this chapter the financial part of this project is discussed. In the first section a cost breakdown is performed, and an estimation of the Return on Investment (RoI) is made. In the following section the market is analyzed and the opportunities for this AWE system is investigated.

13.1 Cost analysis and return on investment

The Return of Investment (RoI) is a measure of the efficiency of investment. A positive RoI means the investors gain more than they initially invested.

In order to come up with the RoI value, it is necessary to know the development costs, production costs and operational costs. The table 13.1 shows all the necessary costs relevant to the RoI calculation.

Based on the interest the kitepower system already received during its development it is expected that at least 150 units will be sold and that each kite system has an operational life of 20 years when critical components are replaced regularly. Development costs include costs of facility and services, salaries of employee, design and construction of prototype, testing and certification of product, production tool cost and wind tunnel model and testing cost. Facility and services include renting of office, bills, etc. For salaries, it is assumed that 5 engineers will work full-time for 2.5 years in the development phase for (€50000 per year). Designing and building the prototype includes the construction of a small scale prototype which can be tested. Production tool cost is a high cost contributing to the development costs, this is because expensive moulds will be used to shape the CFRP for the production of the kite. The production costs include all the cost combining the raw materials and labors. Operational costs include replacement costs, insurance costs etc. These values are all estimated based upon reference systems and data. The production costs include all the cost combining the raw materials and labors. Operational costs include replacement costs, insurance costs etc. These values are all estimated based upon reference systems and data.

To determine the RoI, the maximum LCOE is taken as the starting point. An excel spread sheet (supplied by E-Kite) is used to facilitate the RoI calculation.

After completing the cost breakdown for the kite system, it can be seen in table 13.1 that a total of €75000 needs to be invested per unit, of which, €65500 is the production cost and €9500 is the development cost. The calculation of the LCOE and the RoI is summarized in tables 13.2

Table 13.1: Cost breakdown list of the kite power system

General		
expected number of unit sold	150	
Development costs		
	Price [€]	Mass [kg]
Facility and service cost	150,000	
Salaries	625,000	
Des. and constr. of prototype	50,000	
Testing and certification product	50,000	
Production tools cost	500,000	
Wind tunnel model and testing	20,000	
Total	1,395,000	
Production costs		
Kite structural material costs		
Spread tow carbon fibers (120 m^2 at 40 €/m^2)	4,800	15.5
Resin for CFRP (8 kg at 30 €/kg)	240	8
Rohacell IG-F 31 (17 m^2 at 36 €/m^2)	612	8.5
Kite additional component costs		
Tether	800	
Turbine	200	0.5
Onboard control computer	1,000	0.3
On ground computer	1,000	
Batteries	500	2
Wires	50	1
Sensors	4,000	0.4
Tranceiver	1,000	0.5
Actuators (4x15W, 1x7W, 1x1W)	1,250	2.5
Kite manufacturing costs		
Estimated per kite	10,000	
Ground station production costs		
Complete ground station	40,000	
Total production costs	65,452	
Operational and maintenance costs		
Insurance	1,000	
Replcament cost for tether	1,600	
Replacement cost of kite struc.	3,130	
Replcament cost for others	700	
Maintenance	1,500	
Computer aided management	200	
Total operational costs	8,130	
Input for Return on Investment calculation		
Investment per unit	74,752	
Replacement costs per year per unit	5,430	
Maintenance costs per year per unit	2,700	

and 13.3. A plant investment cost (cost related to auxiliary systems and infrastructure for a new development) of €20000 is considered. The operational costs are estimated to be just over €8300 per year.

Two multipliers are considered in the LCOE calculation, which are the inflation correction and the discount rate (sometimes indicated as Weighted Average Cost of Capital). Both these factors are used to convert anticipated returns from an investment project to the current market value. The inflation rate is assumed to be 2 %/year and the discount rate is set to 8 %/year, a value between 5 % and 10 % is considered acceptable by KitePower, 8 % is used by E-Kite for their LCOE calculations.

Two target LCOE's are considered; the 10 ct/kWh, which was initially set as a requirement, and 11.3 ct/kWh, which is according to E-Kite a limit to be competitive in the market. The value of 11.3 ct/kWh is obtained by taking 75 % of the LCOE of PV solar cells (15 ct/kWh).

With an average power output of 21.6 kW during a year of operation, the RoI turn out to be for a target LCOE of 10 ct/kWh -1.9 %. At this LCOE the investment costs are higher than the returns. However, at an LCOE of 11.3 ct/kWh the RoI is 9.8 %.

Table 13.2: LCOE and RoI calculation part 1: input and results of calculation

Parameter	Value
Average power output [kW]	21.6
Assumed annual electricity yield [KWh/yr]	189,346
Replacement costs [€/yr]	5,450
Other operational costs [€/yr]	2,700
AWE system investment [€]	75,000
Balance of plant investment [€]	20,000
Inflation per annum	0.02
Discount rate per annum	0.08
LCOE [ct/kW]	10.19
ROI at LCOE of 10 ct/kW	-1.9%
ROI at LCOE of 10.3 ct/kW	9.8%

Important to note was that this RoI calculation is a theoretical exercise; the 21.6 kW system will not be commercially exploited, it will solely be a step towards a 100 kW power plant. It is expected that the 100 kW system will have a much lower LCOE, as the costs are not expected to scale with the power; the required surface area will be 40 m^2, which is only a factor 3.15 larger than the current 12.7 m^2, and the complexity of the system would in general not increase. If the total cost is considered to scale with the surface area (which can be considered an overestimation) an LCOE of 7 ct/kWh will be feasible at an RoI of 1 %.

13.2 Market analysis

The objective of the Market Analysis is to determine the competitive cost and volume of the market for the new Airborne Wind Energy (AWE) system. As one of the main objectives of the new system is to create energy, the analysis mainly focuses on the market of the products that create energy. First, the new system is compared to contemporary dispatchable and non-dispatchable systems and its value in the current market is determined. The latter part is done by considering the (dis)advantages of the new kite system and at where it can operate. Second, a forecast is made to establish the future market. This forecast not only focuses on the current product's state but also on possible new technology. Then again, the share value of the new AWE system is determined by looking at the relevance and the possible growth or shrinkage.

13.2.1 Current market

In this section, the current available products and technology are listed. Also, data is presented to indicate the share in the current market and what their costs are. Finally, comparable projects are discussed and their share value is determined.

Comparable products

Dispatchable In the table 13.4, the main generators of electricity (dispatchable resources) are presented. The amount of electricity generated in 2011 and the Levelized Costs of Energy (LCOE) are also listed. The data is from the U.S. Energy Information Administration .

Table 13.3: LCOE and RoI calculation part 2: Yearly cost and energy yield of AWE system

		Operational costs		Investment costs		Total costs
Year	Yield [kWh]	Replacement [€]	Other [€]	AWE system[€]	Plant [€]	per year [€]
0	-	-	-	75,000	20000	95,000
1	-	5,559	2,754	-	-	8,313
2	-	5,670	2,809	-	-	8,479
3	-	5,784	2,865	-	-	8,649
4	-	5,899	2,923	-	-	8,822
5	-	6,017	2,981	-	-	8,998
6	-	6,138	3,041	-	-	9,178
7	-	6,260	3,101	-	-	9,362
8	-	6,386	3,163	-	-	9,549
9	-	6,513	3,227	-	-	9,740
10	-	6,644	3,291	-	-	9,935
11	-	6,776	3,357	-	-	10,134
12	-	6,912	3,424	-	-	10,336
13	-	7,050	3,493	-	-	10,543
14	-	7,191	3,563	-	-	10,754
15	-	7,335	3,634	-	-	10,969
16	-	7,482	3,707	-	-	11,188
17	-	7,631	3,781	-	-	11,412
18	-	7,784	3,856	-	-	11,640
19	-	7,940	3,933	-	-	11,873
20	-	8,098	4,012	-	-	12,110

Table 13.4: Non-renewable energy resources

Plant Type	Elec. Generated [Billions kWh]	Sub Type	LCOE [$/MWh]
Coal	1687.9	Coventional	100.1
		Advanced	135.5
Natural Gas	809.2	Conventional	67.1
		Combustion Turbine	104.6
Petroleum	24.1	-	0
Nuclear Electric Energy	790.2	-	108.4
Geothermal	16.7	-	89.6

Non-dispatchable The amount of energy and the costs of main generators is shown in the table 13.5, together with the renewable energy resources. Again, the data was obtained from the U.S. Energy Information Administration.

At 12.37 %, the non-dispatchable energy generation has a smaller contribution to the market compared to the dispatchable resources. Wind energy, which contains AWE, generates 3 % of the total electricity. With respect to the cost, Conventional Natural Gas is the best plant type with a LCOE of 67.1 $/MWh, and is followed by Wind Energy with a LCOE of 86.6 $/MWh. Also it is shown that the cost of Land Wind Energy is much lower than Offshore Wind Energy. That is because it is more expensive to transport to and from offshore. Besides that, offshore project's costs are higher due to harder conditions at sea.

Similar projects

After looking at the overall energy generation, more comparable projects will be discussed in detail. For this part, the projects that are in concept, but not in production, will also be included.

Table 13.5: Renewable energy resources

Plant Type	Elec. Generated [Billions kWh]	Sub Type	LCOE [$/MWh]
Hydroelectric Power	323.1	-	90.3
Solar Power	1.8	Thermal	261.5
		PV	144.3
Wind	119.7	Land	86.6
		Offshore	221.5
Biomass	24.0	-	111.0

E-Kite: The E-kite technology consists of a flexible kite which is connected with two cables to a generator. The controls are integrated in the ground system. According to the company, the E-Kite system can generate 50 kW of power with a 50 % lower cost than a regular wind turbine. The project can focus on highly populated places due to the claimed safety features. As the ground station is mobile, it can be used to deliver power to events, festivals, etc. [1]

TwingTec: TwingTec uses a system consisting of a hybrid kite, two tethers for control and a generator on the ground. It should generate, with sufficient wind speed, 50 kW of power. There are no concrete statements about the cost. This can be attributed to the fact that the TwingTec is still in test phase. It focuses mainly on sparsely populated regions, like farms or industrial areas. [2][3]

Makani (Google X): The Makani system consists of a kite (an airfoil with turbines), a conductive tether and a ground station where a generator produces electricity. The kite flies in circles, and by doing so, pulls the tether and drive the generator. Due to its rigid kite, the project is focusing on uninhabited areas. According to the site, during the test flights, the Makani is 50 % cheaper than a regular turbine and has a capacity factor of 60 %. For a turbine, this is 35 %. [4][5]

EnerKite: The kite for this system is a hybrid, inflatable wing and operates at an altitude between 100 m and 300 m. It has three lines to control the kite, two to control the flight direction and one to lower the kite. The EnerKite expects to achieve 100 kW with a LCOE of 105 $/MWh in 2017. The kite is suited for inhabited places because it is inflatable and has minimal noise and visual impact. [6]

KiteGen: This is an automated system that comprises a lightweight kite tethered on either side of its length to a stem that has the ability to rotate. The stem is part of a ground station in which power is generated due to the motion of the kite in the wind. The system has the ability to achieve high altitudes and thus has access to steady wind at high velocities for power generation. KiteGen states that the new system can achieve a power of 100 kW. KiteGen also claims that when a wind farm (200 kites) was used, the LCOE could be an average of 25 $/MWh. These farms only operate in sparsely inhabited regions. [7]

Kite Power 2.0: The Kite Power system has an inflatable wing attached to a ground station

[1] URL: `http://www.e-kite.com/` [cited 21 november 2014]
[2] URL: `http://twingtec.ch/twingtec-in-the-einstein-swiss-tv-show/` [cited 18 November 2014]
[3] URL: `http://twingtec.ch/twingtec-in-the-news-on-swiss-tv-sf1-tagesschau/` [cited 18 November 2014]
[4] URL: `http://www.google.com/makani/` [cited 18 November 2014]
[5] URL: `http://techcrunch.com/2013/05/22/google-x-acquires-makani-power-and-its-airborne-wind-turbines/` [cited 18 November 2014]
[6] URL: `http://www.enerkite.de/en/` [cited 19 november 2014]
[7] URL: `http://www.kitegen.com/en/` [cited 19 november 2014]

by a tether. It operates at altitudes above 200 m. At these altitudes, the wind is stronger and more steady leading to an increase in capacity factors to approximately 60 % (conventional wind turbines achieve 35 %). With respect to power, it is expected that the system can produce 32 kW. There is no information about the cost because the project is still in early testing phase. [8]

Added value

With respect to the overall energy generation, there is room to extend the production of wind energy. Currently, only 3 % of all the electricity comes from wind energy. This creates an opportunity to increase the amount of wind energy generated and thus also increase the share of renewable energy.

The LCOE for land wind energy is relatively low compared to the other resources. Although the LCOE of 11.3 ct/kWh of the kite system discussed in the previous section is still a lot higher than the 86.6 $/MWh. The up-scaled version of 100 kW average power output is considered to have a significantly lower LCOE, which would be competitive with classic wind turbines.

A weakness of the new AWE system is the limitation of regions in which it can operate. To let the kite operate efficient and safe, a sparsely populated area is required, in which also a sufficient amount of wind occurs. The kite requires a large ground area to operate, this due safety regulations and public acceptance.

This last part bears some uncertainties. The airborne wing energy concept is new, so it does not have its own specifications. Currently, it is or an extension of a building or it will be classified as an aircraft. The choice is made based on the height and how flexible/rigid the kite is. If the kite is checked on the safety regulations of an aircraft, an entire redesign could be necessary. This weakness could also be projected on the public acceptance. As it stands at the moment, the public is in favor of renewable energy. However, if the kite is found to be unsafe, the public opinion could become negative towards the AWE systems. The result of this is that the operational regions would be limited to only uninhabited ones.

To project the new system into the current AWE market, it is assumed that the system meets the requirements that were stated. For instance, the required power of 40 kW will be generated. This would mean that the new AWE could compete with the comparable project mentioned above. Only the EnerKite and TwingTec claim to have a larger power generation but no actual test data is presented. The LCOE is estimated between 50 $/MWh and 100 $/MWh, which is in range with the other companies. These LCOE would decrease when the new system is in large scale production say like wind farms. The production cost of the ground station and generator will relatively not change if the kite power would be increased. So then the LCOE can become even lower. Overall, if the kite meets the chosen requirement, it can have a significant share on the current market. If it is possible to keep the LCOE low and measure up to the regulations, there is a future for this system.

13.2.2 Future market

In this section, the new system will be analyzed with respect to the market in 5-10 years from now. This means a forecast must be made. After the new market, with old and new

[8] URL: `http://www.kitepower.eu/` [cited 19 november 2014]

products/systems, is established, the share of this AWE will be discussed again. Only now, for the future market.

Establishing new market

After examining the 'Electricity Net Generation' data sheet, it can be stated that the fossil fuel share is slightly decreasing the last 10 years and the amount of electricity generated by the renewable energy sources is increasing. Due to the fact that the resources for fossil fuel generations is shrinking and the public opinion is leaning more and more towards green energy, the share of the dispatchable energy generation will keep decreasing for the next 5 to 10 years. This implies that the share of renewable energy would keep increasing. This seems about right, because the amount of green projects has been increasing for the last couple of years and it is expected that this trend will continue. According to the U.S. Energy Information Administration, the prices for the renewable energy plant type are forecasted to decrease. The increasing production scale could have a positive influences on this. Also, new regulations could be more beneficial for the renewable plant types than for dispatchable ones.

The forecast, with respect to comparable systems, is that the amount of AWE institutions is increased significantly. As can be seen in figure 13.1, for the last 10 years, the number has increased. Besides, it is expected that the demand for renewable energy will increase so the there is enough room for more initiatives. The forecast also includes that most AWE systems shall have increased their power to 100-150 kW. This can be made possible by improving their kites with new technologies, operate at higher (jet-stream) altitudes or find new methods. It is also predicted that the average cost of AWE systems will drop. This can be a result of the fact that the kites would have lower operating cost, because the operation is fully automatic. Also, by creating wind farms, the overall cost would also decrease. The lifetime of the kite could have also been improved, which could result in lower investment costs.

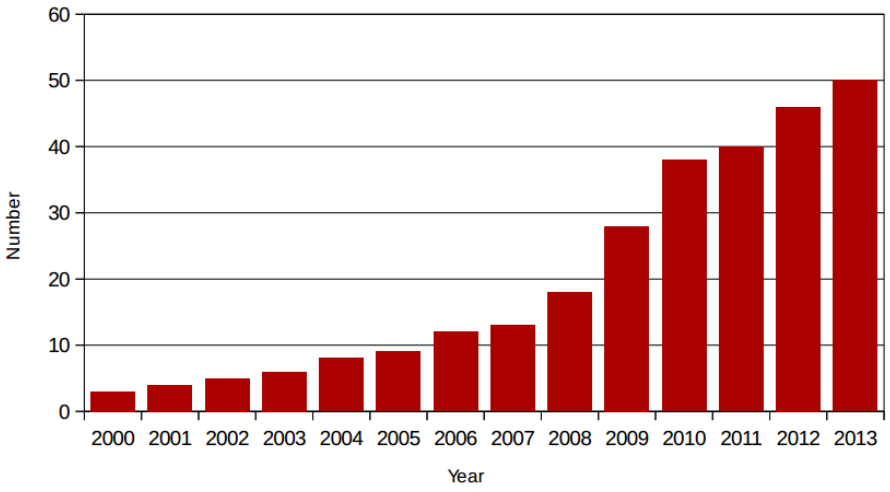

Figure 13.1: Growth in AWE projects

Added value

In the future, the share of wind energy will have been increased but there will still be room for new AWE projects. This project could have a significant part of the airborne wind energy

sector. By expanding the production, the cost can be kept low. Wind farm with hundreds of kites will be more efficient than just a single kite in the private sector. To achieve these commercial objectives, suitable regions have to be sourced; suitable not only with enough wind and space but also not suited for other renewable projects like solar and hydroelectricity. In other words, the airborne wind energy is a unique solution in that region to create green energy. Canada ,for example, has large regions with constant wind, but not enough sunlight for solar generation.

Another opportunity lies in the visual aspect of the kite. If the size of the kite increases, it could be possible to see them from a distance. The surface of the kite can then be used for advertisement of (investment) companies. In exchange for cooperation with the project, there logo can be printed on the wing surface. Also, the possibility to advertise could help to sell the system to multiple companies. However, there is also a weakness. By making the kite visual to the surrounding inhabitants, the public acceptance could suffer. The kite looks more present and therefore more dangerous to the public.

A weakness of the project is that it is not suited for offshore application. There is more wind power on sea, which attracts companies like SkySails. They use the airborne wind energy concept offshore, so they can achieve a higher constant power. To operate at sea, they have to compromise on the lifespan of the kites, which is significantly shorter.

In 10 years, the classification for the AWE system can be changed. This could mean that the kite should always meet the requirements of an aircraft. Then it is possible that the system has to undergo a redesign to meet the future requirements. Another possibility is that there is whole new classification for AWE systems. This would also mean that there can be new requirements to be met and so a redesign is necessary.

After the conceptual design phase, when the type of kite is determined, more can be stated about the share value in the future market. For now, the AWE system has to make sure that it is suited for mass production to reduce cost and has a large enough life span, to make it more attractive for on land operations.

Chapter 14

Risk analysis

Technical risk is a factor that must be taken into account when developing and/or enhancing a relatively new technology. The risk is the product of impact and the probability of occurrence of an event. This technological advancement has the potential to provide and enhance capability to the already existing pumping kite generation capacity. However, there is the potential of extended development time and in turn ballooning costs. In this chapter, the risks involved in the implementation of this project are discussed. The technical risk assessment is made in section 14.1 and the various contingency measures to be implemented are covered in the subsequent section 14.2.

14.1 Technical design risk

In the build-up of this project, several processes are undergone. The first is the development process, from the introduction to determination of the concept to be followed through. The second is the design phase, in which the kite is developed fully to a concept awaiting production. Finally, there is an implementation phase which is not within the scope of this project. A risk map for the development stage is omitted since this has been covered extensively in the mid-term phase [9]. For the design phase, the components of the kite become the focus of a risk analysis geared to mitigate chances of failure during operation in totality. The division of sections is:

- Tether
- Kite control unit
- Sensors
- Actuators
- Power generating turbine
- Ground station

A risk table 14.3 is built for this section to enable the system components be investigated in more depth. The various sub-systems that build them up are investigated for possible risks and how to best mitigate these risks. The resulting risk as a combination of occurrence and consequence is displayed in table 14.1.

Table 14.1: Design risk before mitigation strategies

Consequence \ Probability	Unlikely	Probable	Very likely
High	2.1.1, 2.1.3, 2.1.4, 2.2.1, 2.2.2, 6.1.1, 6.1.3, 6.1.4, 6.4.1, 6.4.2, 6.5.2	1.1.1, 1.2.1, 1.2.2 ,2.3.1, 2.3.2, 3.1.1, 3.1.2, 3.1.3, 3.2.1, 3.2.2, 3.2.3, 3.3.1, 3.3.2, 3.3.3, 4.1, 4.2, 4.3, 6.6.1	
Medium	3.3.1, 3.3.2, 3.3.3, 5.1.2, 5.1.3, 6.2.1, 6.5.1,	5.1.1, 6.1.2, 6.2.1, 6.3.1, 6.6.2	
Low			

14.2 Contingency management

In this section, the mitigation strategies followed to try and solve the potential major problems shown, are discussed. As can be seen in the 'Technical design risk table' figure 14.3, there are several risks that are ranked high enough to become a problem if not stemmed in their earlier stages, despite not being classified as high risk (the combination Probable-High). The design is geared towards reducing the risk of failure of the system as much as possible. Some of these risks are discussed here and their mitigation strategies are highlighted.

Tether failure: The tether can fail due to either wear from use or from some catastrophic break in the line. To mitigate the tether failing from wear, strict maintenance schedules are followed and the inspection of the tether is done to ensure that it is still in proper operational condition. The tether could also break inexplicably. There is no particular method by which this can be stopped from occurring; however, the kite can be equipped with increased range of sensors to allow it still effectively glide back to the ground station, thus preventing its loss.

GPS and attitude sensors: These sensors are used to indicate the position and orientation of the kite at any given moment in time. To reduce the risk of their failure, the software is made such that troubleshooting can be made relatively simple. This allows for the testing of the software, thus checking for faulty algorithms. In addition to this, double redundancy is employed thus allowing for control to be maintained. However, should one system fail and the backup kicks in, the risk of catastrophic failure is also increased as there is no backup system to the backup sensors. Thus, in such a case, the kite is landed for repair.

Tether breaks: The kite is connected to the ground station by a tether. In the event that this tether suffers a break, the kite would be lost or damaged in the fall to ground. To counter this, the range of the transceiver on the ground station is increased as is the one in the kite control unit. This allows the kite to autonomously glide safely back to ground. This system lowers the risk of this event significantly.

On-board battery failure: The working of the kite is powered by a battery pack that is charged by the rotation of the power generating turbine. The battery pack could fail in several ways:

- The failure of the turbine. The turbine constantly charges the battery and so its failure leads to the failure of the battery pack. To reduce the risk of this eventuality, a spare battery pack is installed in the kite. This pack provides enough power in the event of a battery failure to land the kite safely.

Table 14.2: Design risks after mitigation strategies

Consequence \ Probability	Unlikely	Probable	Very likely
High	3.3.2, 6.2.2, 8.1.1,	1.1.1, 3.1.1, 3.1.2,	
Medium	1.1.1, 1.2.1, 1.2.2, 2.3.1, 2.3.2, 2.2.2, 3.3.1, 3.3.2, 3.3.3, 4.1,4.2, 4.3, 5.1.1, 6.1.1, 6.1.3, 6.3.1, 6.4.1,6.4.2, 6.5.2, 6.6.1	3.1.1, 3.1.2, 3.1.3, 3.2.1, 3.2.2, 3.2.3	
Low	2.1.4, 2.2.1, 5.1.2, 5.1.3, 6.1.2, 6.1.4, 6.2.1, 6.5.1, 6.6.2		

- Overcharging of the battery due to constant charging from the turbine. To prevent this from occurring, a voltage regulator is installed; this prevents damage to the batteries and mitigates the potential of this failure mode.
- The battery could also suffer from leakage. This could in turn cause damage to the kite at the point of battery placement. To prevent this, strict maintenance checks are carried out and the lifetime of the battery is managed.

After the mitigation strategies have been implemented, an updated risk map of the design risk is illustrated in table 14.2.

Table 14.3: Design risk

Problem Area or Activity	Risks Identified	Description	Probability Of Occurrence	Impact Intensity	Mitigation Strategy	Description
Tether	1.1 Bridle connection point	1.1.1 Failure of connection point	Probable	High	Control	Strict enforcement of maintenance schedules and practices
						Design connection points for greater loads than expected
	1.2 Tether	1.2.1 Tether line fails due to wear	Probable	High	Control	Strict enforcement of maintenance shedules and practices
		1.2.2 Tether line breaks	Probable	High	Control	Increase signal range of antennae to effect automated glide procedure to the ground station
Kite Control Unit	2.1 Battery	2.1.1 Fails to charge	Unlikely	High	Control	Spare battery on board to provide enough power to return to ground safely for maintenance
		2.1.2 Cell leakage	Probable	Medium	Control	Strict enforcement of maintenance schedules and practices
		2.1.3 Overcharging	Unlikely	High	Control	Use of a voltage regulator
		2.1.4 Freezing	Unlikely	High	Control	Thermal insulation
	2.2 Antenna	2.2.1 Breakage/failure	Unlikely	High	Control	Double redundancy - Extra antenna in the system to compensate for loss
		2.2.2 Loss of communication with ground station	Probable	High	Control	Increase signal range to effect automated glide to parking altitude or ground
	2.3 Power electronics	2.3.1 Malfunction (change in impedance)	Probable	High	Control	Wide operational testing before implementation
		2.3.2 Circuit break	Probable	High	Retain	Frequent operational testing to ensure the circuits function effectively
Sensors	3.1 Attitude sensors	3.1.1 Incorrect measurement values	Probable	High	Control	These sensors are used to indicate the position and orientation of the kite.
		3.1.2 Failure to respond to commands	Probable	High	Control	The software running the sensors is made such that it is relatively easy to test for faulty algorithms.
		3.1.3 Failure to transmit data	Probable	High	Control	Should either of the two fail, there is a backup sensor to ensure that the kite safely returns to ground for repair
	3.2 GPS	3.2.1 Incorrect measurement values	Probable	High	Control	
		3.2.2 Failure to respond to commands	Probable	High	Control	
		3.2.3 Failure to transmit data	Probable	High	Control	
	3.3 Pitot tube	3.3.1 Incorrect measurement values	Unlikely	Medium	Control	Double redundancy - A second pitot tube is installed on the kite to ensure continued measurement of speed data
		3.3.2 Failure to respond to commands	Unlikely	Medium	Control	
		3.3.3 Failure to transmit data	Unlikely	Medium	Control	
Actuators	4.1 Ailerons	4.1.1 Failure to respond to commands	Probable	High	Control	Strict enforcement of maintenance schedules and practices
	4.2 Rudder	4.1.2 Structural failure	Probable	High	Control	Application of a Built in Self Testing system to check for the need for repair or maintenance and
	4.3 Elevator		Probable	High	Control	predict potential operational failure
Power generating turbine	5.1 Turbine	5.1.1 Blade damage	Probable	Medium	Retain	An emergency battery pack is carried on board the kite. This battery is fully charged at all times
		5.1.2 Uncoupling	Unlikely	Medium	Retain	and is used to power the kite operations and to ensure safe landing
		5.1.3 Jammed	Unlikely	Medium	Retain	
Ground station	6.1 Battery pack	6.1.1 Fails to charge	Unlikely	High	Control	Spare battery to provide power for the system without causing interruptions
		6.1.2 Cell leakage	Probable	Medium	Control	Strict enforcement of maintenance schedules and practices
		6.1.3 Overcharging	Unlikely	High	Control	Use of a voltage regulator
		6.1.4 Freezing	Unlikely	High	Control	Thermal insulation
	6.2 Winch	6.2.1 Jams	Unlikely	Medium	Control	Strict enforcement of maintenance schedules and practices
	6.3 Processors	6.3.1 Do not react to input or give output	Probable	Medium	Control	Double redundancy - Have a second processor board with similar capabilities
	6.4 Antenna	6.4.1 Breakage/failure	Unlikely	High	Control	Double redundancy - Extra antenna in the system to compensate for loss
		6.4.2 Loss of communication with kite	Unlikely	High	Control	Double redundancy - Extra antenna to allow for uninterrupted operation
	6.5 Mast	6.5.1 Unable to rotate	Unlikely	Medium	Retain	Adapt the kite to land in that position. If this fails then abort the landing
		6.5.2 Lack of current transimission	Unlikely	High	Control	Enforcement of maintenance schedules on the mast
	6.6 Generator and power electronics	6.6.1 Malfunction (change in impedance)	Probable	High	Control	Wide operational testing before implementation
		6.6.2 Circuit break	Probable	Medium	Control	Frequent operational testing to ensure the circuits function effectively

Legend of mitigation strategies:
Control: The group solves the problem in house
Deflect: The problem is directed to the tutors and teaching assistants for help
Retain: The risk is accepted by the group
Avoid: This branch is possibly eliminated if it becomes troublesome

Chapter 15

RAMS

After discussing the risks for the system, the Reliability, Availability, Maintainability and Safety (RAMS) characteristics of the system can be elaborated upon. In this chapter the reliability (section 15.1), availability (section 15.2), maintainability (15.3 and safety (section 15.4) will be discussed.

15.1 Reliability

The system described in part I has not yet been tested and therefore an analysis is done to estimate the reliability of the system. As mentioned in section 14.2, the tether is the most critical component of the system and therefore the reliability of the tether will give a good approximation of the system reliability.

The approach used in chapter 33 of [4] for the determination of the lifetime of the tether, will be applied here. In table 15.1 the input parameters are given.

Table 15.1: System parameters

Parameter	Value
Fiber type	SK75 + coating
Reel-out force ($F_{\text{reel-out}}$) [kN]	20
Tether length (r) [m]	200 to 700
Reel-out duration ($t_{r_{\text{out}}}$) [s]	160
Cycle Time (t_{cycle}) [s]	170
Drum and pulley diameters (D_{dp}) [mm]	1200
Design factor (f_{d}) [-]	3
Day/night temperature factor (f_{t}) [-]	1.5
Season temperature factor (f_{s}) [-]	1.5

The Minimum Breaking Load (MBL), F_{MB}, of the tether can be calculated by applying a design factor (f_{d}) to the reel-out force ($F_{\text{reel-out}}$), which gives:

$$F_{\text{MB}} = f_{\text{d}} F_{\text{reel-out}} = 60\text{kN} \tag{15.1}$$

According to [4] this corresponds to a worked-in tether diameter of 6mm. The worked-in diameter is a weaving procedure that reduces the tether diameter by about 15%. The additional weight due to tether coating (t_{coat}) is assumed to be 10%. The density of High-Modulus Polyethylene (HMPE), ρ_{HMPE}, is 970 $^{\text{kg}}/_{\text{m}^3}$.

15.1.1 Creep lifetime

For the calculation of the creep lifetime the tension in the tether (F_{t}) is needed. This is calculated as follows; note that the fiber weight (W_{fiber}) is excluding the tether coating:

$$F_{\text{t}} = \frac{F_{\text{MB}}}{W_{\text{fiber}}}\rho_{\text{HMPE}} = \frac{F_{\text{MB}}}{(1 - t_{\text{coat}})W_{\text{tether}}}\rho_{\text{HMPE}} \tag{15.2}$$

with W_{tether} as the weight of the tether.

Using figure 15.1 the Safe Working Life (SWL), L_{sw}, for SK75 can be obtained. A load of 0.522 GPa corresponds an SWL of 0.6 years. On the other hand, this value for SWL needs to be corrected for two factors.

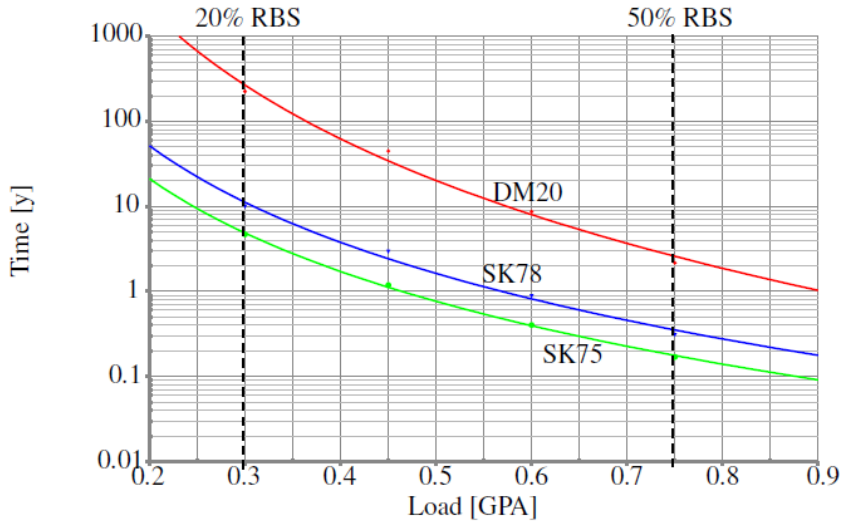

Figure 15.1: Safe Working Life ($T = 20°\text{C}$) graphs for DSM Dyneema fibers based on creep rupture [3]

The first correction has to do with the fact that the tether is not subjected by the reel-out mean load 100% of the time. Therefore, the load factor f_{l} can be computed as follows:

$$f_{\text{l}} = \frac{t_{\text{cycle}}}{t_{\text{r}_{\text{out}}}} = \frac{170}{160} = 1.06 \tag{15.3}$$

The second correction is for temperature changes, not only due to day/night cycle, but also seasonal changes. The day/night temperature factor and the season temperature factor are given in table 15.1 and are derived according to the book "Airborne Wind Energy" [4].

Thus, the service life (SL), L_s, based on creep check, can be computed as follows:

$$L_s = L_{sw} f_l f_t f_s = 0.6 \cdot 1.06 \cdot 1.5 \cdot 1.5 = 1.43 \text{years} \tag{15.4}$$

15.1.2 Bending lifetime

Apart from the creep criterion, also the bending fatigue has to be looked into. For the determination of the bending lifetime, the ratio D_{dp}/d_t is needed, where D_{dp} is the diameter of both the sheave and the drum, and d_t is the tether worked in diameter. The value for D_{dp} is 1200 mm and d_t is 6 mm. The D_{dp}/d_t ratio then becomes 200.

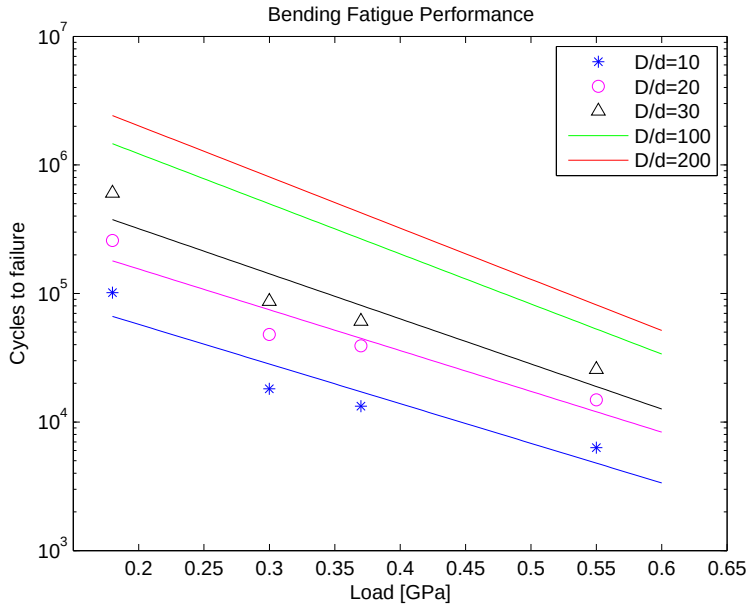

Figure 15.2: Bending fatigue performance of ropes made of SK75 with DSM property coating (data obtained from [3])

From figure 15.2 can be seen that the corresponding number of Cycles To Failure (CTF), N_{CTF}, for a load of 0.522GPa, is equal to 10500 single bends. This value is obtained by extrapolating the original data for D_{dp}/d_t to the new ratios of 100 and 200. The SWL for bending fatigue is calculated with equation 15.5.

$$L_{sw} = \frac{N_{CTF}}{N_{bends}} t_{cycle} \tag{15.5}$$

In this case, the number of bends is equal to two and the cycle time is equal to 170 s, as determined in table 15.1. With all these values, the SWL becomes 104 days. An improved construction of the tether (see patent on braided rope construction [19]), results in doubling the lifetime to 208 days. Thus, the overall lifetime of the tether is 208days.

15.1.3 Quantification of reliability

The system has not yet been operational and therefore no experimental data is available. Therefore, what follows, is an overview of the possible reliabilities for the tether. Here, the method

used in the book "Systems Engineering And Analysis" [20] is applied.

A range from 1 to 5 for the numbers of tether failures is chosen. The total operational lifetime is set to 20 years. The failure rate, λ_f, can be computed as follows:

$$\lambda_f = \frac{N_f}{t_{tot_{op}}} \tag{15.6}$$

The reliability of the tether is then equal to:

$$R_{op} = e^{-\lambda_f t_{op}} \tag{15.7}$$

with t_{op} as the moment in time at which the reliability is determined.

The results are given in figure 15.3

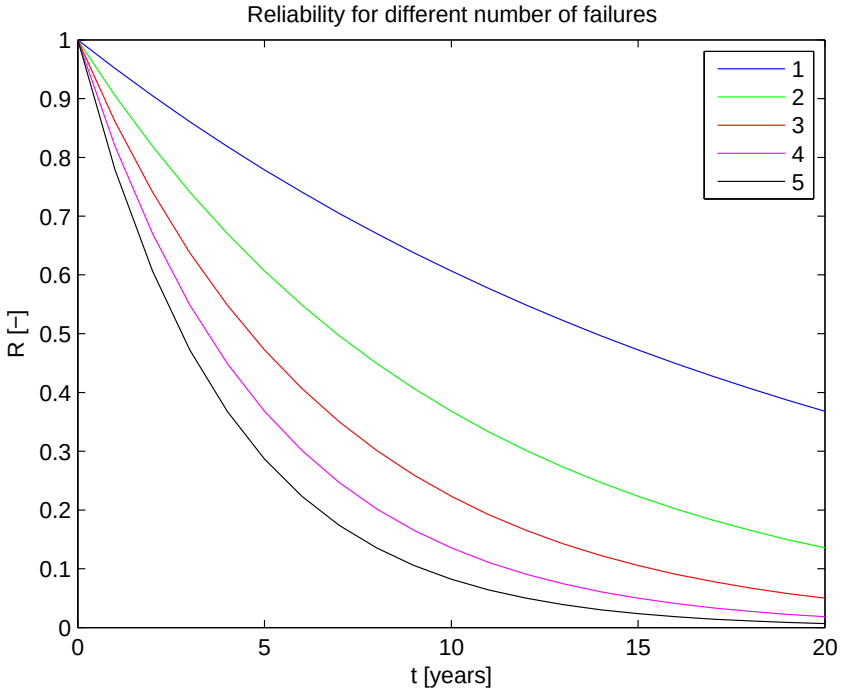

Figure 15.3: Reliability of the tether as a function of time for different number of failures

15.2 Availability

The availability of the system is correlated with the logistics of the system. The higher the availability, the quicker a costumer can receive the system from the manufacturer. The logistics flow block diagram can be seen in figure 15.4. In this figure the flow of assets from suppliers up to decommissioning (recycling and disposal) is shown.

Reducing the amount of involved suppliers (the top row in the figure) would reduce the risk of supply delays and therefore increasing the availability. This risk can also be mitigated by having a stock available, but this would require a bigger initial investment.

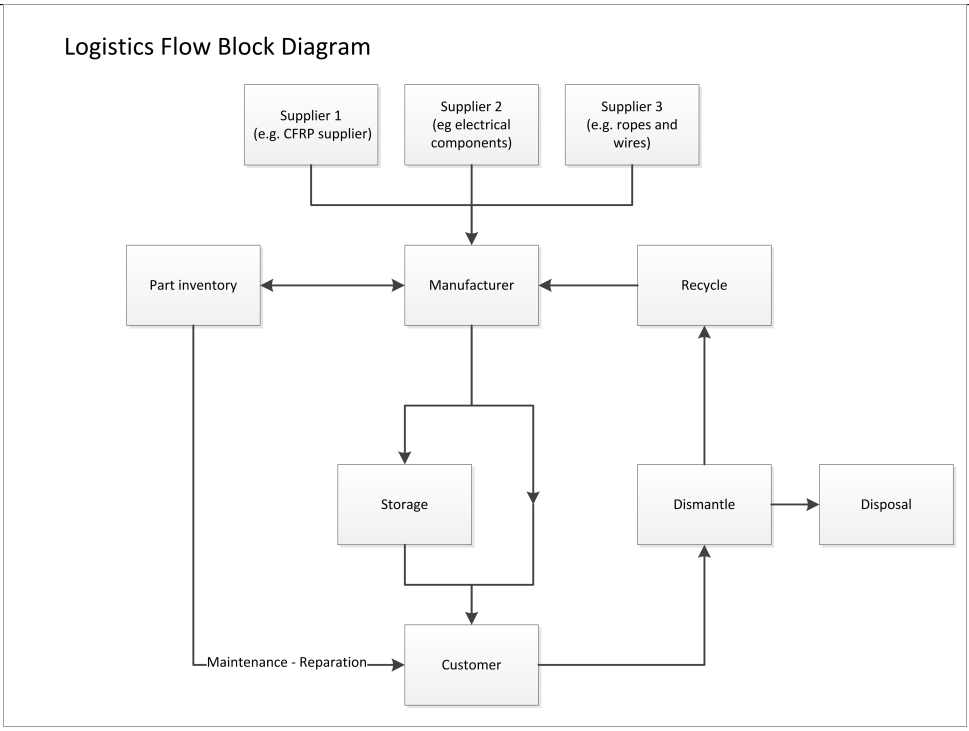

Figure 15.4: Logistics flow block diagram

Manufacturing is done on a single location; this means that no logistics is required between different manufacturers. After manufacturing, the product can first be stored before it is sold to a customer. This is undesirable because it would require additional storage space for finished products. On the other hand, it does mean that the time between order and delivery can be greatly reduced, and therefore the availability of the system is increased.

Storing an extra kite is an option suitable when the power generation unit has to be used in disaster areas, where immediate power is required. If stock is insufficient, the power generation unit will be delivered to the customer directly from the manufacturer.

15.3 Maintainability

During the lifetime of the system, some time has to be reserved for maintenance. This will help to keep the performance of the system optimal. The maintenance of the system can be divided into scheduled maintenance and unscheduled maintenance. An overview of the overall procedure can be seen in figure 15.5.

15.3.1 Scheduled maintenance

An outline of scheduled maintenance is given in table 15.2. As can be noticed in the table, some components will only be replaced In Case Of Failure (ICOF). These components are included in the design in such a way that they need to be replaced only ICOF. As shown in section 14.2, most of the problems that can arise in these components can be mitigated by redundancy.

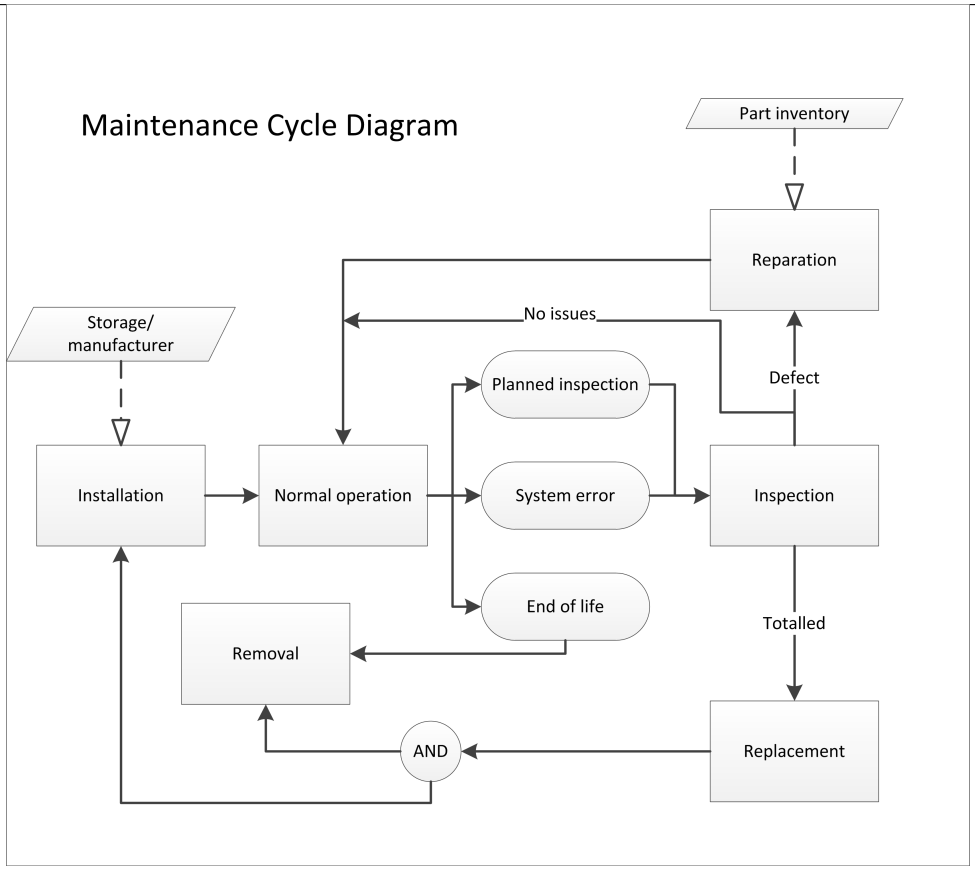

Figure 15.5: Maintenance cycle diagram

Components such as the winch and the mast are unlikely to reach failure and are therefore also replaced or repaired ICOF.

Another aspect of scheduled maintenance is the cleaning of the kite and external components thereof. This is done in order to remove excessive accumulation of dirt.

15.3.2 Unscheduled maintenance

Figure 15.5 shows an outline of the procedures that should be done regarding system errors. The components for which these activities are needed are either capable of being replaced or repaired.

Cleaning of the different system components is also included in the unscheduled maintenance. This is done in case for example a swarm of insects hits the kite, as mentioned in 4.4. When an incident like this occurs, the performance of the kite will decrease. At this point the computer at the ground station will give a signal to maintenance personnel and he will then notice the dirt on the kite. Subsequently, the kite is brought down for cleaning.

Table 15.2: Scheduled maintenance

Component	Sub-Component	Replacement [y]
Tether	1 Tether	0.5
Kite Control Unit	2.1 Battery	2.5
	2.2 Antenna	ICOF
	2.3 Power electronics	ICOF
Sensors	3.1 Attitude sensors	ICOF
	3.2 GPS	ICOF
	3.3 Pitot tube	ICOF
Actuators	4.1 Ailerons	2.5
	4.2 Rudder	2.5
	4.3 Elevator	2.5
Power Generating Turbine	5 Turbine	ICOF
Ground Station	6.1 Battery pack	2.5
	6.2 Winch	ICOF
	6.3 Processors	ICOF
	6.4 Antenna	ICOF
	6.5 Mast	ICOF
	6.6 Generator and power electronics	ICOF
Kite Materials	7 Materials	5

* In Case Of Failure (ICOF)

15.4 Safety

A factor that has a great impact on public acceptance, is safety. In this section the different safety features of the system will be presented.

First, the system has some safe modes during operation. In case of high wind speeds, the kite is statically parked at a higher altitude. On the other hand, in case of low wind speeds during a short period of time, the kite is kept in the air by reverse pumping (investing energy in the system to keep the kite airborne). When low wind conditions are present for a longer period, the kite is landed.

In chapter 14, the different risks for the system were discussed and there the different mitigation procedures can be seen. All these procedures are, not only for the safety of the complete system, but they also help to keep the system free from hazards to humans.

Mitigation is chosen such, that if a major component fails, the kite can still be able to perform a safe landing. Even if the tether breaks, which is the most critical situation as shown in table 14.1, the kite can still land safely. Also, the operational safety of the system is relatively high. This is because the system is fully automated.

The system is also safe to the environment. This means that the system does not expel harmful gasses during operation. Therefore, it can be concluded that the system is safe, both operationally and environmentally.

Chapter 16

Development process

In this chapter the future development of the DSE kite design is proposed. The process will have five different steps, leading to a commercially viable system. In each step the design, manufacturing and testing is taken into account. The DSE design in this development process is considered as a prototype design, which in time can be scaled to larger systems. Off course this process will be a highly sustainable and effective development, which is also explained in this chapter.

16.1 Project design & development logic

During the DSE project, a durable and lightweight wing has been designed. It will provide 40 kW power during the traction phase, resulting in an average power output of 22 kW, with the key geometry parameters presented in chapter 3. The future project plan of this system; to physically build and test the prototype with scaling possibilities up to and beyond 100 kW. This would make the system not only technically feasible, but also highly commercially viable when compared to renewable as well as non-renewable energy producing systems.

This will take the following steps: first, two models will be designed, followed by the DSE prototype of 22 kW, hereafter a demo system of 50 kW and finally the commercial system of 100 kW. The project design and development (PD&D) gives a logical order of activities that have to be executed from detailed design until product delivery of a commercial system to the customer. The PD&D is visualized in figure 16.2. The first phase is shown in red, the second phase in green, the third phase in orange, the fourth phase in blue and the fifth and final phase in yellow. The development time line with its corresponding milestones can be seen in figure 16.1. All five systems have a Designing, Manufacturing and Testing phase.

1. Model 1: testing in OJF

   In the nearby future, first the smallest model of 0.75 kW will be built, that will only be tested on its aerodynamic performance using the Open Jet Facility (OJF) at TU Delft. This model is therefore sized to fit in the OJF test section with a span of 2m. A detailed FEM- en CFD-analysis of the design has to be done, as well as the design of the software and control interface subsystems. Using the facilities of the Aerospace Engineering faculty, it is possible to fabricate all main components (wing, tail boom, tail and control surfaces). The materials used for this model are inexpensive plastics, with comparable surface roughness to carbon. Other more specific parts, such as control surface actuators,

will have to be ordered. Manufacturing of this model will take approximately 3 months. Required wind speed during testing is $\approx 30\,\mathrm{m/s}$, to match the flight Reynolds number. After intensive testing of this smaller model at the OJF, the aerodynamic properties of the design are derived to validate the assumed values. Testing will lead to revisions in the design as well as to fixes in the production of the system.

2. Model 2: testing on current ground station

   A larger model will be built, that will be connected to the existing ground station of KitePower 2.0. At the Aerospace Engineering faculty, it is possible to fabricate the smaller carbon components, such as the tail and control surfaces. The two main components (wing and tail boom) should be fabricated at facilities that can fabricate larger components, e.g. the nearby Airborne Aerospace company at Ypenburg. For this model system, the material used will be the readily available T300 baseline carbon fiber. Aerodynamic testing of smaller parts can still be done at the OJF. Controllability and performance testing of the complete system attached to the ground station will occur at Valkenburg Airbase.

3. Prototype

   Now the prototype system with the design dimensions proposed in the DSE can be built. Design flaws that followed from the testing of the model, can be coped with during the redesign phase (redesign of the model). Similar manufacturing procedures will be followed as for model 2. Testing of this system will require a ground station that can deal with the higher traction forces, though it may be possible with improvements on the current ground station. Tether forces for the systems are also shown in table 16.1. More advanced structural optimization methods will be used to optimize the system, as been proposed in the DSE. Important to start on during the third phase, is the marketing and sales of the product. Also, the training of operators, who will perform maintenance on the systems and monitor their performance, is planned to start in this phase.

4. Demo & commercial

   Finally a 50 kW demo system and later a 100 kW commercial system can be built. Detailed project development is difficult to elaborate on, as this is highly dependent on the outcomes of the model testing, the prototype and many yet unknown and undefinable factors. It must be noted that when the commercial system has been successfully tested, certification tests must also be performed to ensure the system meets all regulatory requirements. This testing will highly depend on what the future will bring regarding the governmental certification of Airborne Wind Energy systems. For marketing and sales purposes a public demonstration will be given. The demonstration will also be beneficial to the public perception of this rigid kite AWE system.

In table 16.1 the key numbers of the five systems are shown. All systems are scaled with respect to the DSE prototype system and based on the power equations from chapter 4, the same aspect ratio of 7.88 for each system as well as an approximated relation between the power generated during reel-out and and the average power output.

16.2 Sustainable development

For the final design of the kite, the sustainable aspects of the airborne wind power generation have been reconsidered, based on the sustainability part of the Mid-Term Review [9]. The kite

Table 16.1: Key numbers development systems

System	P_{average} [kW]	P_{rout} [kW]	F_{tether} [kN]	S_{proj} [m2]	b_{w} [m]	d_{t} [mm]
Model 1	0.75	1.35	0.6	0.5	2	-
Model 2	10	18	8	5.5	6.6	4
Prototype	22	40	20	12.5	10	5.8
Demo	50	90	35	22	13	8
Commercial	100	180	70	40	18	10.5

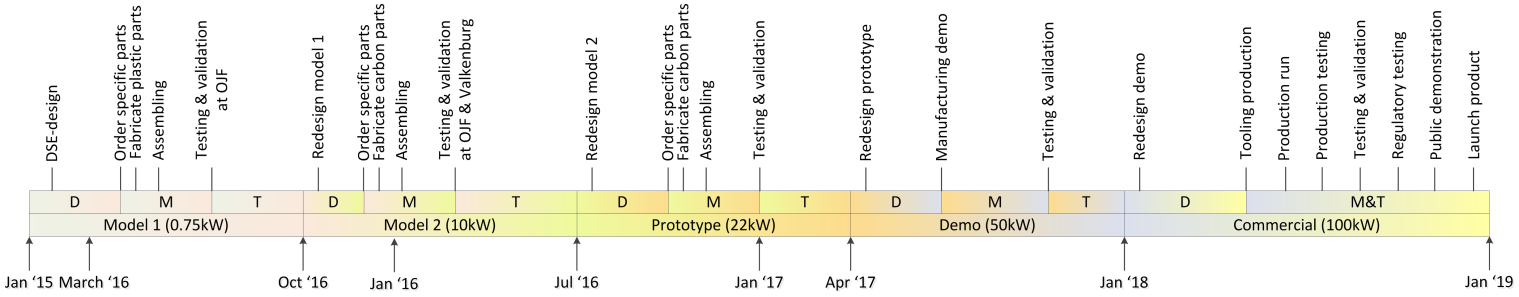

Figure 16.1: Development timeline

has been structurally optimized to reduce the weight to a minimum, reducing the amount of material used and the impact on the environment. The rigid carbon kite will have low vibrations resulting in low-noise production. Also the reduced vibrations cause an increase in the durability by reducing fatigue stresses. To further reduce manufacturing energy during the development of the system, the first model will only be made out of environmentally more friendly plastics as this system will only be aerodynamically tested in the OJF. The second model is sized to be connected to the existing ground station of KitePower 2.0, ensuring that until this stage in the development process all initial investments can be used for investigation of the kite itself. Later, on the commercial carbon kite systems will have high durability and low maintenance, reducing the environmental impact.

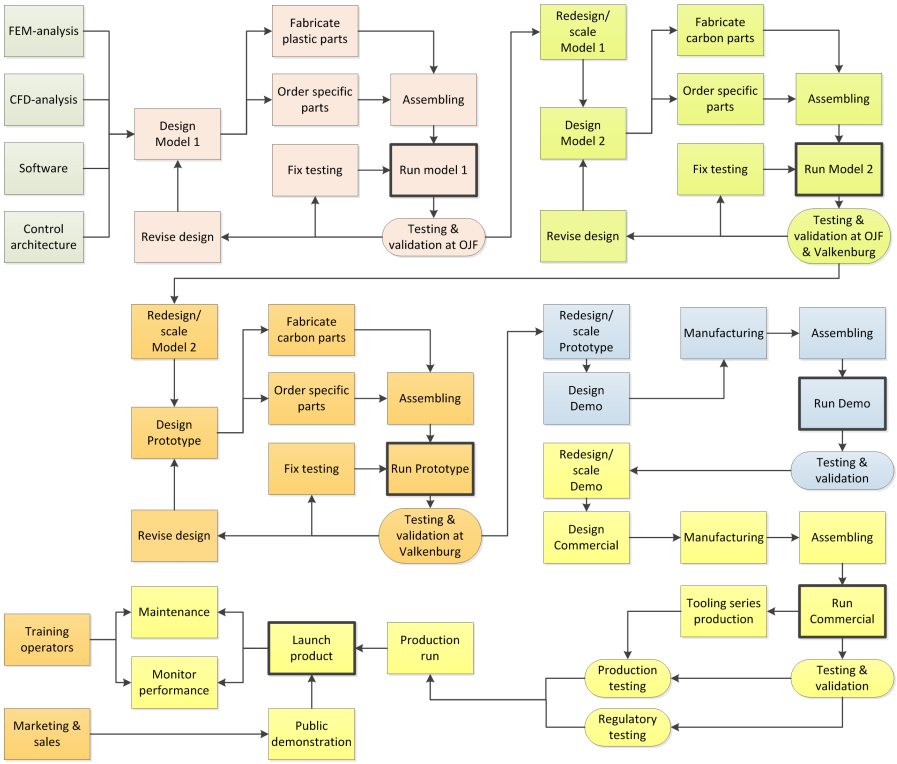

Figure 16.2: Project design & development logic

Part IV

Conclusions

Chapter 17

Compliance matrix

In this chapter the compliance matrix which follows from the requirements presented in chapter 2, is presented. The matrix can be seen in table 17.1.

As can be seen most requirements are met, just requirement 2.4.2, 'usage of toxic material shall be avoided', and requirement 1.3.3, 'A maximum operational wind speed of 25 $^{m}/_{s}$ shall be reached', are not compliant.

The reason requirement 2.4.2 is not met is due to the choice of CFRP as principal building material. This material was chosen to be able to comply with requirement 1.3.2, the stall speed. The material has very high strength over weight properties and was needed to comply with 1.3.2. Because this requirement is more important for possible commercial success, it was given priority over toxicity of the material. At a later stage, when the design has been optimized further, CFRP could be replaced by a natural fiber composite when this is a hard requirement set by the customer. In most cases however, the power yield benefits of the kite with CFRP weigh up against the negative effects.

Requirement 1.3.3 was not met because of how the system responds to higher wind velocities. The reel-out speed has been set to one-third of the wind speed by requirement 1.1.1, which results at higher wind speeds in a very short duration of the traction phase, reducing the total cycle power output to 0 at a wind speed of 23 $^{m}/_{s}$. Section 9.1 goes into more detail on this subject, and explains how this can be solved.

There are also a couple of requirements in the compliance matrix that have been graded as 'Yes∗', these requirements are partly met. In what way these can be improved is listed below.

- Req. 1.2.2 - Weight shall be minimized: Although weight optimization has been performed, there is still a lot of room for improvement. For example by examining different ply layups of the carbon fiber, and by using a FEA package to analyze the connection details so the weight contingency can be reduced.
- Req. 2.1.4 - Fully automated over entire flight envelope: In general the kite is controllable during all flight modes because three types of control surfaces are used; ailerons, rudder and elevator. This means that the kite is very suitable for auto-pilot application. However, the auto-pilot itself still needs to be developed.
- Req. 2.3.3 - Major components shall be accessible and maintainable: Although it is mentioned in the text that they are used, the access panels and hatches are not yet

designed. The design of these details should be done during future developments of the kite.

- Req. 2.5.1 - Cost over Mechanical power (LCOE of less than 10 ¢/kW): According to the return of investment calculations an LCOE of 10 ¢/kW can be reached, however at this point the return on investment will be equal to zero. Therefore the same calculation has also been done with an LCOE of 11.3 ¢/kW, which is 75% of the LCOE of a PV solar panel. This calculations lead to an return on investment of over 15%, which is sufficient for this kite. When the kite is scaled up to 100 kW the LCOE is expected to drop as the amount of material used and the complexity of the system scales at a smaller rate than the power output.
- Req. 2.6.1 - Sensor space shall be integrated: Although space is available, it was not mentioned in the design where the sensors are placed.

Table 17.1: Project requirement compliance matrix

Number	Requirement	Value	Compliant
1	Perform mission technically		
1.1	*Operational*		
1.1.1	Reel out speed	$\frac{1}{3}V_w$	Yes
1.1.2	Reel-in speed and force	> 10 m/s, < 10 kN	Yes
1.1.3	Position end of reel-in phase is starting point next phase	-	Yes
1.2	*Structural*		
1.2.1	Wing span	< 10 m	Yes
1.2.2	Weight shall be optimized	-	Yes*
1.3	*Flight Condition*		
1.3.1	Tether length	200 m − 700 m	Yes
1.3.2	Stall speed	< 5 m/s	Yes
1.3.3	Maximum operational wind speed	25 m/s	No
1.4	*Mission output*		
1.4.1	Power output during reel-out	40 kW at 6 m/s $< V_w <$ 12 m/s	Yes
2	*Perform mission within constraints*		
2.1	*Performance*		
2.1.1	The wing shall perform a pumping cycle operation	-	Yes
2.1.2	The wing shall be able to fly in figures-of-eight	-	Yes
2.1.3	Aerodynamically stable over entire flight envelope	-	Yes
2.1.4	Fully automated over entire flight envelope	-	Yes*
2.2	*Safety*		
2.2.1	Commercial and military airspace shall be avoided	-	Yes
2.2.2	Flight over inhabited areas shall be avoided	-	Yes
2.2.3	The wing shall be controllable and predictable over entire flight envelope	-	Yes
2.2.4	The system shall have a safe mode	-	Yes
2.3	*Durability*		
2.3.1	Minimum wing lifetime	> 1000 h	Yes
2.3.2	AWE system lifetime	> 20 years	Yes
2.3.3	Major components shall be accessible and maintainable	-	Yes*
2.4	*Sustainability*		
2.4.1	Emission of harmful gasses shall not be allowed	-	Yes
2.4.2	Usage of toxic materials shall be avoided	-	No
2.5	*Cost and efficiency*		
2.5.1	Cost over *mechanical* power ratio	< 10 ¢/kW	Yes*
2.6	*Other*		
2.6.1	Sensor space shall be integrated	-	Yes*
2.6.2	The system shall be able to have an airborne power supply	-	Yes
2.6.3	The wing shall be scalable	-	Yes

Chapter 18

Conclusions

In this report, the detailed design of the *"durable and light-weight kite for pumping kite power generation"* is presented. After 10 weeks of project work, the group was able to extend their knowledge on the concept (Rigid Conventional Kite), which was chosen during the Mid-term review. The report covered several important aspects, which were examined carefully and in great detail.

A number of valuable insights was gained during the project. In the aerodynamics part could be seen that not ${C_L}^3/C_D^2$ is the driving term for kite design but rather $C_{L_{max}}$ is. This is due to the tether drag driving the C_D up with increasing line length. In the structural department, due to the high loads involved, a structure of prismatic tubes with ribs and cloth skin was not viable.

The functional analysis includes a Functional Flow Block Diagram (FFBD) and Functional Breakdown Structure (FBS), which gave an insight to the power generation process. The system characteristics requirements for the project were met. These are shown through the analysis done on aerodynamics, structural, control and stability.

The Wortmann FX73-CL3-152 airfoil is chosen for the wing of the kite due to its very high $C_{L_{max}}$ and large thickness. In order to achieve an as large as possible aspect ratio, it is concluded that the maximum total span(10 m) available for the kite is used. The wing has a surface area of 12.7 m^2, a taper ratio of 0.4 and an aspect ratio of 7.88.

Structural analysis was carried out on the concept and the group decided that the wing will be constructed out of four panels and three ribs per side. The top skin and front and back spar are made from CFRP sandwich panels. The other surfaces are constructed of only CFRP. The total weight of the kite without control components turned out to be 33.78 kg. The boom used to connect the tail to the main wing was chosen to have an elliptical shape due to its better aerodynamics performance, though it was heavier than the square tube that was also considered. At the trailing edge of the main wing the tailboom has an upsweep of 9 deg, to keep the body more tangent to the airflow and increase drag performance.

The stability analyses showed that the kite has roll stability, positive yaw stability and positive longitudinal stability. Only the symmetrical eigenmotions of the dynamic stability were looked upon. Both phugoid and the short-period motion of the kite were analyzed and found to be stable.

In the control part, the aileron and the elevator were designed to make the roll and pitch at

the end and beginning of the traction phase. The rudder is designed to make coordinated turns with a small turn radius to make the kite more effective.

From the market analysis it can be concluded that opportunities lie in regions where no other renewable sources are available (e.g. solar energy). These niche markets could be used to mature the design before it can be applied on a larger scale. The threat for technology, is that the cost of the systems can only be significantly reduced by large scale production of the kite power systems, due to its high development costs.

The chapter on sustainability indicated that the focus on sustainability should be maintained in all phases of the design life cycle.

Chapter 19

Recommendations

In this chapter the recommendations for future developments of this project are summarized. The group has tried to be as complete as possible in covering all engineering aspects of the system, but some parts were either not available, beyond the scope of the project or required more time to elaborate on. The main elements that need further analysis are aerodynamics, structures, TOL, Kite-Ground station interface and Cycle optimization. They will be discussed here in that order.

19.1 Aerodynamics

The aerodynamic analysis was mainly restricted by the tools at hand. XFLR5 is a well known tool, but should only be used for preliminary analysis. The velocity flight regime (Mach numbers of $\approx$ 0.1) justifies the use of a linear tool like XFLR5, but the angles of attack at which the kite operates, require further analysis with CFD models. Also, this type of tool could verify and validate the use of XFLR5 for future use in this field. Because the lack of data on similar projects, the validation with respect to aerodynamics is still incomplete. The high L/W ratio renders comparison with aircraft comparable in size, was impossible. Also the lack of a normal fuselage, with its inherent interference and drag, makes this project hard to validate. Therefore, as stated in chapter 16, first CFD analysis and small scale wind tunnel testing should be performed.

19.2 Structures

Although the method used for the sizing of the wingbox is already quite advanced, there might still be possibilities for weight reduction. Possibilities can be found, for instance, in only using sandwich panels locally in highly loaded areas. Or using strength compatibility for the stiffener calculation, where stiffeners only take bending loads and the skin takes only shear loads. Not taken into account at this point are: aeroelasticity, fatigue, bridle split location, compressive forces due to the bridle angle, shear buckling and buckling under own weight. All these points need to be considered as well. With all these effects that still need to be taken into account it would be wise to use a Finite Element Analysis tool.

19.3 Take-off and landing

A Take-Off and Landing (TOL) concept was developed for the system. This was sized on a relatively low level, because the assignment was focused mostly on the kite itself. For future development and the step towards a commercial system, a more detailed analysis should be executed. That would mean that a lot of the assumptions made in this design of the TOL can not be made for the future detailed analysis.

19.4 Kite-ground station interaction

The interaction design between the ground station, where the trajectory calculations are executed and the auto-pilot is positioned, and the kite is still low in detail.

19.5 Low wind optimization

At this point not the full power production potential of the system is used. There are two areas where significant increases in power production can be achieved: low wind conditions and high wind conditions. If the kite is resized for lower wind speeds, a significant increase in availability of rated power can be achieved. Because according to the wind-data [2], it is very likely that wind velocities are below $5\,{}^{\mathrm{m}}/_{\mathrm{s}}$.

Also lower stall speeds, and therefore lower landing speeds, could be achieved by using high-lift devices. This option was already investigated in chapter 4, but the team ran into the limitations of XFLR5.

19.6 High wind optimization

The current kite can also, with some modification, still be able to achieve its rated power at much higher wind speeds than at this moment. High winds currently result in a kite that flies at extreme velocities, close to Mach numbers of 0.3. By incorporating some sort of spoiler, the drag at these wing velocities could be increased at will, slowing the kite down. If then the kite is re-trimmed, a new equilibrium could be achieved. This, in combination with a decrease in reel out velocity to below one third of the wind velocity leads to a fully trimmable kite that can be used at rated power in a much wider range of wind speeds, with a much higher electricity yield per annum. Also, the increased yield may justify the weight increase by incorporating such a system, but this would have to be examined.

Bibliography

[1] J.A.Mulder/ W.H.J.J van Staveren/J.C. van der Vaart/ E.de Weerdt/ C.C. de Visser/ A.C. in't Veld/ E.mooij. *"Flight Dynamics reader"*, Faculty of Aerospac Engineering, TU Delft, March 24, 2013.

[2] G. Wolken-Mohlmann. "OnKites - Studie zur Verwendung von Flugenergieanlagen". Technical report, Fraunhofer-Institut fur Windenergie und Energiesystemtechnik, 2012.

[3] Uwe Ahrens/ Moritz Diehl / Roland Schmehl. *Airborne Wind Energy.* Springer-Verlag, 2013, pg.563-585.

[4] Uwe Ahrens/ Moritz Diehl / Roland Schmehl. *Airborne Wind Energy.* Springer-Verlag, 2013.

[5] Sheets M /Burghardt F / Karalar T / Ammer J / Chee YH / Rabaey J. "A Power-Managed Protocol Processor for Wireless Sensor Networks". Technical report, University of California, Berkeley, 2006.

[6] Hermans D / Decuypere R. "A challenge for Micro and Mini UAV: The Sensor Problem". Technical report, Royal Military Academy of Belgium, 2005.

[7] The Royal Engineering Academy. *Wind Turbine Power Calculations RWE npower renewables Mechanical and Electrical Engineering Power Industry.*

[8] M.S. Gney / K. Kaygusuz. Hydrokinetic energy conversion systems: A technology status review. *"Renewable and Sustainable Energy Reviews"*, 'Department of Chemistry, Karadeniz Technical University, Turkey', 2010.

[9] DSE fall 2014 Group-3. "mid-term report". Technical report, Delft University of Technology, 2014.

[10] Gerrit Wolken-Mhlmann. *"Onkites - Studie Zur Verwendung Von Flugenergieanlagen, Untersuchung der Windpotentiale"*, Fraunhofer-Institut fr Windenergie und Energiesystemtechnik (IWES), 2012.

[11] International Civil Aviation Organization. *Manual of the ICAO standard atmosphere : extended to 80 kilometres (262 500 feet) / International Civil Aviation Organization.* Montreal, Quebec : International Civil Aviation Organization, 1993.

[12] F. Rasi Marzabadi/M.R. Soltani. *Effect of leading-edge roughness on boundary layer transition of an oscillating airfoil*, Sharif University of Technology, 23 December 2012.

[13] Nianxin Ren / Jinping Ou. *Dust Effect on the Performance of Wind Turbine Airfoils*, School of Civil Engineering, Harbin Institute of Technolgy, China, 23 December 2012.

[14] T.H.G Megson. *"Aircraft structures for engineering student"*. Butterworth-Heinemann, 2005, 2nd Edition.

[15] R.L. Penning. "ESDU file 94007: Elastic Buckling of Cylindrically Curved Laminated Fibre Reinforced Composite Panels With All Edges Simply-Supported Under Biaxial Loading". Technical report, ESDU, 1994.

[16] Dr. Jan Roskam. *Airplane design, PartV:component weight estimation.* Design,Analysis and Research Corporation, 2003, chapter 3.

[17] Mohammad H. Sadraey. *Aircraft Design.* Wiley, 2012.

[18] Althaus / Dieter. *Stuttgarter Profilkatalog II.* Institut fr Aerodynamik und Gasdynamik (IAG), Universitt Stuttgart. View and Sohn Braunschweig, 1981.

[19] R. L. M. Bosman. *Braided rope construction. US Patent US 7,789,007*, 7 Sept 2010.

[20] Benjamin S. Blanchard/ Walter J. Fabrycky. *Systems Engineering And Analysis, third edition.* Prentice Hall, 1997, pg.345-396.